

Dedicated to my parents for their unending support in all capacities, and for not rubbing it in too hard when I finally proved that our family really is made up entirely of engineers. You've been on my side since the beginning and I can't thank you enough for it.

J. D. Tobin  
*New Mexico Institute of Mining and Technology*  
*August, 2014*

**QUANTITATIVE SCHLIEREN MEASUREMENT OF  
EXPLOSIVELY-DRIVEN SHOCK WAVE DENSITY,  
TEMPERATURE, AND PRESSURE PROFILES.**

by

J. D. Tobin

Submitted in Partial Fulfillment  
of the Requirements for the Degree of  
Master of Science in Mechanical Engineering  
with Specialization in Explosives Engineering

New Mexico Institute of Mining and Technology  
Socorro, New Mexico  
August, 2014

## ABSTRACT

Shock waves produced from the detonation of small explosives are characterized using the high-speed schlieren imaging technique. Results are used to determine quantitative and qualitative information about the shocks characteristics. The refractive index gradient field is extracted from successive images and converted to a density field using the Abel deconvolution method. The density field was used to determine shock overpressure and overpressure duration behind the shock wave. This analysis used a weak lens, which provided a known calibration to convert the images pixel intensities into refractive index gradient values. The tests performed used three types of explosive compounds: shotgun shell primers, NONEL shock tube, and Detasheet. The analysis only considered time periods where the shock was clearly separated from the detonation gases and free of any explosively-propelled fragments. Several different temperature profiles were used to determine the pressure field using the ideal gas law. The hydrocode CTH, developed by Sandia National Laboratories, was used to determine a temperature profile, which was also used to calculate the pressure field. Results showed the ability to accurately measure the pressure profile of a shock wave optically using a quantitative schlieren technique. The use of a temperature decay profile as predicted from CTH was observed to yield the most accurate optical pressure data compared to piezoelectric pressure gage data.

**Keywords:** EXPLOSIVES; SHOCK WAVES; SCHLIEREN IMAGING; PRESSURE PROFILE; TEMPERATURE PROFILE; DENSITY PROFILE; ABEL INVERSION METHOD

# CONTENTS

|   |           |
|---|-----------|
| <b>LIST OF FIGURES</b>  | <b>iv</b> |
| <b>1. INTRODUCTION</b>  | <b>1</b>  |
| 1.1 Motivation . . . . .  | 1         |
| 1.2 Literature Review . . . . .                                   | 1         |
| 1.2.1 Shock Waves . . . . .                                       | 1         |
| 1.2.2 Traditional Pressure Measurement Techniques . . . . .       | 2         |
| 1.2.3 Optical Techniques . . . . .                                | 4         |
| 1.2.4 Objectives . . . . .  | 5         |
| <b>2. EXPERIMENTAL METHODS</b>                                    | <b>6</b>  |
| 2.1 High-Speed Imaging . . . . .                                  | 6         |
| 2.2 Schlieren Imaging Technique . . . . .                         | 7         |
| 2.2.1 Dual-Field-Lens Schlieren Setup . . . . .                   | 7         |
| 2.3 Quantitative Schlieren Imaging . . . . .                      | 9         |
| 2.3.1 General Principles of Light Refraction . . . . .            | 9         |
| 2.3.2 General Process for Determining the Density Field . . . . . | 12        |
| 2.4 Explosive Material . . . . .                                  | 14        |
| 2.5 Pressure Gage Measurements . . . . .                          | 14        |
| 2.6 Shock Wave Imaging . . . . .                                  | 17        |
| 2.6.1 Digital Image Processing for Pressure Measurement . . . . . | 18        |
| 2.6.2 Abel Deconvolution Process . . . . .                        | 20        |
| <b>3. FLAT PLATE ANALYSIS</b>                                     | <b>24</b> |
| <b>4. CTH MODELING</b>  | <b>27</b> |

|  |           |
|--|-----------|
| <b>5. EXPERIMENTAL RESULTS</b>                                   | <b>38</b> |
| 5.1 Temperature Calculations from Optical Measurements . . . . . | 38        |
| 5.1.1 Shot Shell Primers . . . . .                               | 38        |
| 5.1.2 NONEL Shock Tube . . . . .                                 | 48        |
| 5.1.3 Detasheet . . . . .  | 57        |
| 5.2 Pressure Calculations from Optical Measurements . . . . .    | 66        |
| 5.2.1 Shot Shell Primers . . . . .                               | 66        |
| 5.2.2 NONEL Shock Tube . . . . .                                 | 69        |
| 5.2.3 Detasheet . . . . .  | 72        |
| 5.2.4 Intensity Corrections . . . . .                            | 74        |
| <b>6. CONCLUSIONS AND RECOMMENDATIONS FOR FUTURE RESEARCH</b>    | <b>78</b> |
| 6.1 Future Work . . . . .  | 79        |
| <b>BIBLIOGRAPHY</b>  | <b>80</b> |

## LIST OF FIGURES

|     |   |    |
|-----|---|----|
| 1.1 | Idealized pressure profile denoting peak overpressure and pressure duration, including negative pulse. . . . .  | 2  |
| 1.2 | Schematic of dual-field-lens arrangement. . . . .   | 4  |
| 2.1 | Schematic of dual-field-lens arrangement with area highlighted denoting placement of explosives (shotshell primers, NONEL shock tube, or Detasheet). . . . .  | 8  |
| 2.2 | Diagram of light refraction through some schlieren object centered in the dual-field-lens schlieren setup. . . . .  | 9  |
| 2.3 | A) shows a diagram of light refraction through positive lens in the dual-field-lens schlieren setup; b) shows gradients across two lenses of 10 <i>m</i> (on the left) and 4 <i>m</i> focal lengths; c) shows an average of three horizontal rows of pixels taken from the center of the two lens. . . . .  | 11 |
| 2.4 | Calibration lens intensity and specific physical location with 5th-order polynomial fit. . . . .  | 13 |
| 2.5 | Piezoelectric gage location within dual-field-lens schlieren setup. The gage is secured within an aluminum plate. The edge of the plate is diagonally cut to allow shock to travel over top surface without reflecting off plate surface. In this orientation, the shock will be coming from the right. . . . .   | 16 |
| 2.6 | Standard pressure trace from the detonation of Detasheet using 50 psi piezoelectric gage for data collection. . . . .   | 17 |
| 2.7 | Example of shock track routine using a non-sequential series of images from the detonation of NONEL. Time step between sequential images is 8.3 $\mu$ s. The white line is generated by the tracking program; the black line is the shock imaged by the dual-field-lens schlieren setup, though it is mostly obscured by the tracking program. The program tracks backwards in time towards the detonation center. Note the subsequent misalignment of the shock tracking line and the shock profile; this is caused by purposefully incorrect placement of the charge center. Images are not sequential. . . . | 19 |
| 2.8 | Row of pixel intensities across a shock from the detonation of NONEL.   | 21 |
| 3.1 | Setup of heated flat plate. . . . .   | 25 |

|      |   |    |
|------|---|----|
| 3.2  | Comparison of flat plate temperature profiles of theoretical and experimental measurements. Uncertainty of experimental temperature is $\pm 2K$ , denoted by the size of the data points (blue).  | 26 |
| 4.1  | Schematic of CTH model. PETN is in gray, tracers in yellow. Total region modeled extends to $2m$ .  | 27 |
| 4.2  | CTH pressure output of 1g PETN detonation, $10cm$ , $44cm$ , and $90cm$ from charge center.   | 29 |
| 4.3  | Logarithmic scale of CTH pressure output of 1g PETN detonation, $10cm$ , $44cm$ , and $90cm$ from charge center.  | 30 |
| 4.4  | CTH temperature output of 1g PETN detonation, $10cm$ , $44cm$ , and $90cm$ from charge center.  | 31 |
| 4.5  | Logarithmic scale of CTH temperature output of 1g PETN detonation, $10cm$ , $44cm$ , and $90cm$ from charge center.   | 32 |
| 4.6  | Normalized CTH output of 1g PETN detonation, $10cm$ from charge center.   | 33 |
| 4.7  | Normalized CTH output of 1g PETN detonation, $44cm$ from charge center.   | 34 |
| 4.8  | Normalized CTH output of 1g PETN detonation, $90cm$ from charge center.   | 35 |
| 4.9  | Scaled CTH output of 1g PETN detonation, $44cm$ from charge center.   | 36 |
| 5.1  | Detonation of shotshell primer. Distance across field-of-view (light gray circle) in lens is $0.1524m$ .  | 39 |
| 5.2  | Oblique shocks forming from fragmentation before shock.   | 39 |
| 5.3  | Shock Mach number from the detonation of shot shell primer.   | 40 |
| 5.4  | Streak image and single image of shot shell primer fired at a 45 degree angle. Vertical time step in streak image is $8.33\mu s$ , distance across field of view (gray background) is $0.0254m$ . | 41 |
| 5.5  | Pixel intensity across shock front.   | 41 |
| 5.6  | Gage pressure profile. Highlighted portion (red) used to determine temperature. Distance from primer face to gage is $0.165m$ .   | 43 |
| 5.7  | Optical density profile created using Abel deconvolution. Highlighted portion (red) used to determine temperature.  | 44 |
| 5.8  | Compilation of temperature profiles from detonation of shot shell primers.  | 45 |
| 5.9  | Linear approximation (red) of CTH temperature profile.  | 46 |
| 5.10 | Peak and atmospheric points used to create linear temperature fit from density profile.   | 47 |
| 5.11 | Comparison of linear approximations of temperature profile.   | 48 |

|      |  |    |
|------|--|----|
| 5.12 | Detonation of NONEL shock tube. Distance across field-of-view is 0.1524m. First image at t=104.86 $\mu$ s from shock exiting NONEL tube, time between sequential images 104.8 $\mu$ s. . . . . | 49 |
| 5.13 | Mach number of shock generated by detonation of NONEL shock tube. Mach number past 0.3m remains constant at 1.03. . . . .  | 50 |
| 5.14 | Example of pixel intensities across shock from NONEL shock tube. Distance from NONEL to gage is 0.127m. . . . .  | 51 |
| 5.15 | Gage pressure profile. Highlighted portion red used to determine temperature. Distance from NONEL to gage is 0.127m. . . . .   | 52 |
| 5.16 | Optical density profile. Entire signal used to determine temperature. Distance from NONEL to gage is 0.127m. . . . .   | 53 |
| 5.17 | Temperature profile directly calculated from optical density and gage pressure. Mach 1.03. . . . .   | 54 |
| 5.18 | Time of peak and low points highlighted. . . . .   | 55 |
| 5.19 | Linear fit of experimental temperature profile. . . . .  | 56 |
| 5.20 | Temperature profile and linear fit directly calculated from optical density and gage pressure. Distance from NONEL to gage is 0.102m. Mach 1.06. . . . .                                       | 57 |
| 5.21 | Typical shock from the detonation of Detasheet. . . . .  | 59 |
| 5.22 | Shock Mach numbers from detonation of Detasheet. . . . .   | 60 |
| 5.23 | Example of pixel intensity across shock from detonation of Detasheet, distance from charge to gage 0.9017m. Mach 1.08. . . . .   | 61 |
| 5.24 | Gage pressure profile. Highlighted portion red used to determine temperature. Distance from Detasheet to gage is 0.902m. . . . .   | 62 |
| 5.25 | Optical density profile. Location of leading edge of shock highlighted. Linear fit of entire selection used to determine temperature. . . . .  | 63 |
| 5.26 | Compilation of temperature profiles from detonation of Detasheet. . . . .  | 64 |
| 5.27 | Linear fit to CTH profile and calculated temperature profile. . . . .  | 65 |
| 5.28 | Linear fit to temperature profile. Distance from gage to charge is 0.456m. . . . .   | 66 |
| 5.29 | Compilation of pressure profiles used with shot shell primers. Mach 1.12, theoretical pressure 185kPa $\pm$ 7kPa. . . . .  | 67 |
| 5.30 | Zoomed in example of raw background intensity. . . . .   | 68 |
| 5.31 | Comparison of theoretical, gage, and optical peak pressures at three distances using NONEL shock tube. . . . .   | 69 |
| 5.32 | Pressure fields derived from linear temperature trends compared to gage pressure. Distance to gage 0.127m. . . . .   | 70 |
| 5.33 | Pressure fields derived from linear temperature trends compared to gage pressure. Distance to gage 0.102m. . . . .   | 71 |

|      |  |    |
|------|--|----|
| 5.34 | Comparison of theoretical, gage, and optical peak pressures at three distances using rolled 1g balls of Detasheet. . . . .     | 72 |
| 5.35 | Comparison of calculated pressure field to gage and CTH pressure profiles. Distance charge to gage 0.9017m. Mach 1.08. . . . . | 73 |
| 5.36 | Comparison of calculated pressure field to gage and CTH pressure profiles. Distance charge to gage 0.457m. Mach 1.09. . . . .  | 74 |
| 5.37 | Background and shock intensities for detonation of Detasheet. . . . .  | 75 |
| 5.38 | Deviated background and shock intensities for detonation of Detasheet. Correction also shown. . . . .                          | 76 |

This thesis is accepted on behalf of the faculty of the Institute by the following committee:

---

Michael Hargather, Advisor

---

---

I release this document to the New Mexico Institute of Mining and Technology.

---

J. D. Tobin

Date

# CHAPTER 1

## INTRODUCTION

### 1.1 Motivation

Optical methods for determining the peak pressure and pressure duration behind the shock have several advantages over more traditional measurement techniques. Some of the major advantages of quantitative optical methods are the non-intrusive nature of data collection, as well as the ability to obtain data about the full field-of-view of the explosive event. This allows for an entire plane of data about the shock's characteristics without potential reflections from other measurement tools such as pressure gages. Pressure gages also can be destroyed during an explosive event, whereas optical techniques requiring high-speed cameras can be safely placed far from the event while still collecting accurate data. Additionally, the ability to image the entire field-of-view allows for qualitative analysis of the shock's behavior in more complex scenarios, such as reflections off of multiple surfaces like cars or buildings. These advantages over more traditional techniques allow optical imaging techniques to be applied to a wider field of analytical applications. Theoretically, any explosive detonation in air could be analyzed using optical techniques, perhaps replacing the necessity for gages entirely or at least eliminating the need to rely solely on single-point measurements taken from gages or other measurement tools.

### 1.2 Literature Review

#### 1.2.1 Shock Waves

One of the most important characteristics from the detonation of explosives is the formation of shock waves. A shock wave is an instantaneous change in a medium characterized by a change in density, temperature and pressure. Shock waves form when a fluid flows faster than the speed of sound, causing a buildup of material at the front of the wave disturbance, which eventually transitions into a shock wave, which exists in a very narrow region [1]. This overpressure and pressure duration determine the explosive impulse delivered to the surrounding area, where impulse is primarily responsible for causing damage to solid structures [2, 3, 4]. This damage is due to dynamic loading on the structure,

imparting kinetic energy leading to structural deformation [5]. The shock wave is oftentimes the first thing to interact with a structure (exempting shrapnel). It is important to understand the characteristics of the shock wave and its propagation through air, particularly in scenarios where can reflect off multiple surfaces, such as in urban environments. In these scenarios, it can be difficult to predict the impulse delivered by a shock wave, or extrapolate a full-field understanding from singular data collection points as is the case with the use of more traditional diagnostic methods, such as piezoelectric gages [4]. Developing a diagnostic tool that can be applied to scenarios where these interactions occur will improve the range of choices available for shock analysis.

### 1.2.2 Traditional Pressure Measurement Techniques

There are various ways to determine the speed and pressure of a shock wave. The speed and pressure can be determined experimentally and theoretically, though the properties from detonations in air are extremely complicated to predict [6]. There are also multiple methods of numerical simulations that can predict the pressures resulting from shock waves [3, 7, 8]. However, it is still necessary to verify such results experimentally. Any methods used are ideally capable of resolving the complete pressure profile in Figure 1.1.

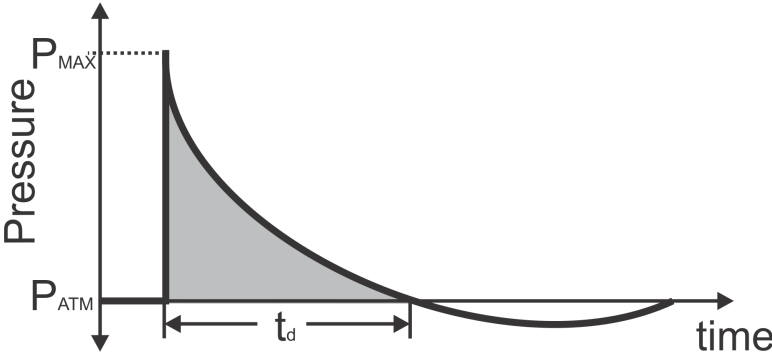


Figure 1.1: Idealized pressure profile denoting peak overpressure and pressure duration, including negative pulse.

In order to determine the pressure from a given shock wave, one of the most commonly employed tools are pressure gages. These gages come in various types and are designed for specific applications; several common ones include piezoelectric probes, carbon probes, pressure plates and fiber optic sensors [9, 10]. These devices record the pressure-time history as an electric signal, which is recorded and used to analyze shock pressure. The gages are designed for specific loading situations, so care must be taken that the gages are not destroyed by excessive loading during an explosive event [11]. This can be a major limiting factor in the high-speed, high-impulse environment of explosive research.

Both Sayapin [9] and MacPherson [10] noted the challenges associated with pressure sensors, particularly in the gages response time when compared to the fast loading and unloading of shock wave pressure. The gages record a plane wave when the shock wave hits the sensor and ideally have a response time fast enough that the noise from the gage would not distort the shocks peak signal [9]. In addition, the gages must be rugged and well designed to withstand the heat and debris from explosions [10].

Alternative methods for determining shock pressure and pressure duration include using a ballistic pendulum or performing plate dent test [12, 13]. The ballistic pendulum method uses two long suspended metal bars placed end to end, with an explosive compound located near the end of the one bar. The explosive is detonated, creating a shock that will travel through the first bar into the second. Ideally, the interface between the two bars is cut and faced such that a wave will be transmitted without reflection. Additionally, the explosive compound is placed far enough away from the metal bars that there will be no deformation from the blast [12]. The wave traveling through the two bars reflects off of the end, creating a tension wave traveling backwards. This tension wave interacts with the remainder of the pressure wave, which can lead to separation of the two bars. The ideal scenario has the second bar sufficiently long enough for the front of the tension wave and the tail of the pressure wave reach the interface at the same moment; the bars will not separate under these conditions. This case demonstrates the length of the pressure wave, as this is true only when the second bar is half the length of the pressure wave [12]. The ballistic pendulum test is fairly complex, requiring multiple tests both to determine the correct length of the second bar, and to account for potential damage done to the first rod by the detonation of high explosives. While this technique can be applied in a laboratory setting, piezoelectric gages are far simpler to operate and produce immediate results after a single test.

The plate dent test, the lead block test, the cylinder expansion test, and the underwater expansion test are used to determine the blast potential of a particular explosive compound [13]. In the first two tests, the known yield strength of the metal is used to determine the output strength, but the initial confinement of the explosive, followed by the fracturing and release of detonation gases prevents exact characterization, as both the shock and the detonation gases act on the material. The third test has the advantage of being completely confined by the water, and the shock can be visualized using high-speed cameras, while the detonation gases oscillate between expansion and implosion. While this technique may yield reasonable information about the shock, the overall technique is more complicated than simply detonating in air. The plate dent test consists of detonating an unconfined charge against a witness plate of known properties. The depth of the dent produced from the detonation can be linearly correlated to the detonation pressure for many explosives. However, a single value for detonation pressure is insufficient data to make any conclusions about the shock overpressure and pressure duration.

### 1.2.3 Optical Techniques

One method for expanding the number of available analytical tools is the use of optical techniques, which are non-intrusive and allow for qualitative and quantitative data. Recent decades have seen a resurgence of interest in the schlieren and shadowgraph optical techniques [14, 15]. These techniques visualize refractive index variations. For use with explosives, they require a high-speed camera, a strong light source, lenses and can be used in the laboratory or in the field with little to no damage.

Traditional schlieren is used for quantitative and qualitative measurements of refractive index variations in transparent media. It visualizes the first derivative of the refractive index in a transparent medium [14, 16]. A typical schlieren setup utilizes two high-quality lens or mirrors in order to visualize a schlieren object. This object can be an air jet, heat convection, shock waves, or any other transparent media through which light may pass. The light is refracted by this object and is partially cut off using a knife-edge (a sharp, narrow edge) prior to entering a camera lens. The knife-edge is a trademark of the schlieren technique [14]. Some percentage of the light entering the camera is cutoff by this knife-edge, produces light and dark patterns with schlieren. These patterns are visual representations of changes in the refractive index within the schlieren object.

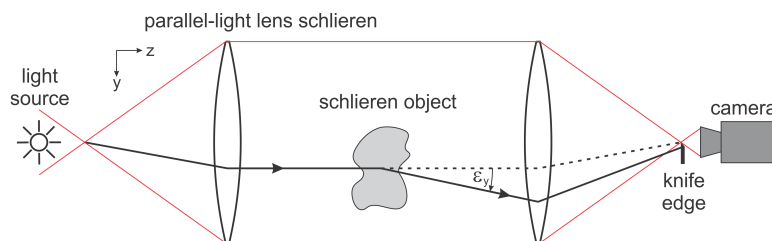


Figure 1.2: Schematic of dual-field-lens arrangement.

The schlieren technique requires exact alignment of its components in order to get quantitative measurements of the observed density gradients. Additionally, the possible field-of-view is limited to the size of the mirrors or lenses, with larger setups quickly becoming very expensive. A similar method is the shadowgraph technique, and is best suited for visualizing strong gradients that dramatically change the observed illumination, particularly shockwaves. However, shadowgraphy visualizes the second derivative of the refractive index, and cannot be used for quantitative density measurement [14, 17, 18].

The schlieren technique has been used for investigating the shock wave properties of explosives [2, 17, 19, 20, 21]. Hargather [2, 22] and Biss [17] have used the retroreflective system and the schlieren system to collect quantitative shock wave data from explosions and gunshots. Shock Mach number and density fields have been determined. Previous work has used various assumptions and theoretical calculations to determine the density field [22, 17]. In order to

determine the pressure field from the density field, the temperature behind the shock was assumed constant [17]. The equations used to determine the theoretical pressure and temperature from Mach number are shown in Equations 1.1 and 1.2.

$$\frac{P}{P_{atm}} = \left(1 + \frac{\gamma - 1}{2} M^2\right)^{\frac{-\gamma}{\gamma - 1}} \quad (1.1)$$

$$\frac{T}{T_{atm}} = \left(1 + \frac{\gamma - 1}{2} M^2\right)^{-1} \quad (1.2)$$

#### 1.2.4 Objectives

The schlieren technique will be evaluated for use in measuring the pressure profile. This work will investigate new approaches to determining the temperature field. Computational and experimental methods of determining the temperature field will be analyzed and the effect on the derived pressure field will be quantified.

## CHAPTER 2

### EXPERIMENTAL METHODS

#### 2.1 High-Speed Imaging

Digital high-speed photography has become commonplace in recent years, with several different manufacturers supplying a wide range of options for scientific analysis. Here, the Photron FASTCAM SA-X2 was used for the majority of experimental testing. This camera allows for a maximum resolution of 1024x1024 images and is capable of recording up to 1 million frames per second (fps) at a reduced resolution of 128x8. It records in grayscale, allowing for increased light sensitivity over color camera options. The camera has a 16 GB internal memory and can record up to 11.18 seconds at the maximum frame rate. The shutter has a standard minimum speed of 1ms with a digital option of 293ns. The camera has a c-mount lens attachment with an optional Nikon F-mount attachment and Nikon lenses were used during all testing. The camera interfaces with "Photron FASTCAM Viewer" software. This allows for digital images to be saved in a variety of formats for later viewing in the software or processing in other programs. Imaging with this camera utilized resolutions ranging from 1024x1024 for general characteristics to 1024x48 for quantitative analysis. Multiple experiments demonstrated the repeatability of the events, allowing for slower frame rates and wider resolutions to be used. In general, frame rates ranging between 64,800 to 100,000 fps is sufficient for accurate analysis. In all cases, the exposure was kept at 0.293 $\mu$ s in order to prevent smearing of the shock. A Nikon 80-200 mm zoom lens set with maximum aperture (f-stop 2.8) and variable zoom was used during testing. The imaging technique requires maximum aperture as closing the aperture truncates the light hitting the camera sensor.

Phantom v711 high-speed camera developed by Vision Research, was used to record data for one day of testing. This camera has a maximum HD resolution of 1280x800 and is capable of recording at frame rates up to 1.4 million fps at a reduced resolution of 128x8. The camera has a 16 GB internal memory and can record gray-scale images up to 2.97 seconds at the maximum frame rate. The shutter has a standard minimum speed 1ms, with a digital option of 300ns. The camera has a standard Nikon F-mount and Nikon lenses were used during all testing. The camera interfaces with a laptop installed with Vision Research PCC software using a GB Ethernet for control and data. Post-processing is done using PCC and multiple file formats may be exported using this software. Imaging with this camera utilized resolutions ranging from 800x600 to 800x32, with frame

rates ranging from 13001 to 230508, respectively. A larger resolution allows for a complete visualization of flow characteristics in the field-of-view allowed by the size of the lenses used in the schlieren system. The smallest resolution used allowed for a faster fps, resolving the shocks motion at more locations as it crossed the field-of-view. At this frame rate, the shock wave observed to jump 15 pixels between frames. During testing, an exposure time of  $0.294\mu s$  was selected to prevent smearing of the shock wave over multiple pixels. Neutral density filters were used to filter light entering the camera to prevent overexposure of the image. The strength of the filter was chosen based on the lens used and the intensity of the light source. The camera lens specifications used with the Photron were also used with the Phantom.

## 2.2 Schlieren Imaging Technique

There are multiple techniques available to image shock waves, the key limiting factor being the size of the explosive event and the available equipment. The schlieren technique is the primary investigative tool, as it permits the direct calculation of the density field from the first-derivative of the refractive index gradient [14]. From the derived density field, it is possible to determine the pressure field behind the shock.

### 2.2.1 Dual-Field-Lens Schlieren Setup

Figure 2.1 shows the setup used throughout testing; the specific orientation of lenses, light and camera is called the dual-field-lens setup. The two large lenses have a focal length of  $70cm$ . The distance between the two field lenses is approximately  $1m$ . The Nikon  $80-200mm$  lens has a minimum focal distance of roughly  $1m$ , so the center of the test section is at least  $1m$ . Additionally, the lenses cannot be too close together in order to prevent the shock from reflecting off the lenses during testing.

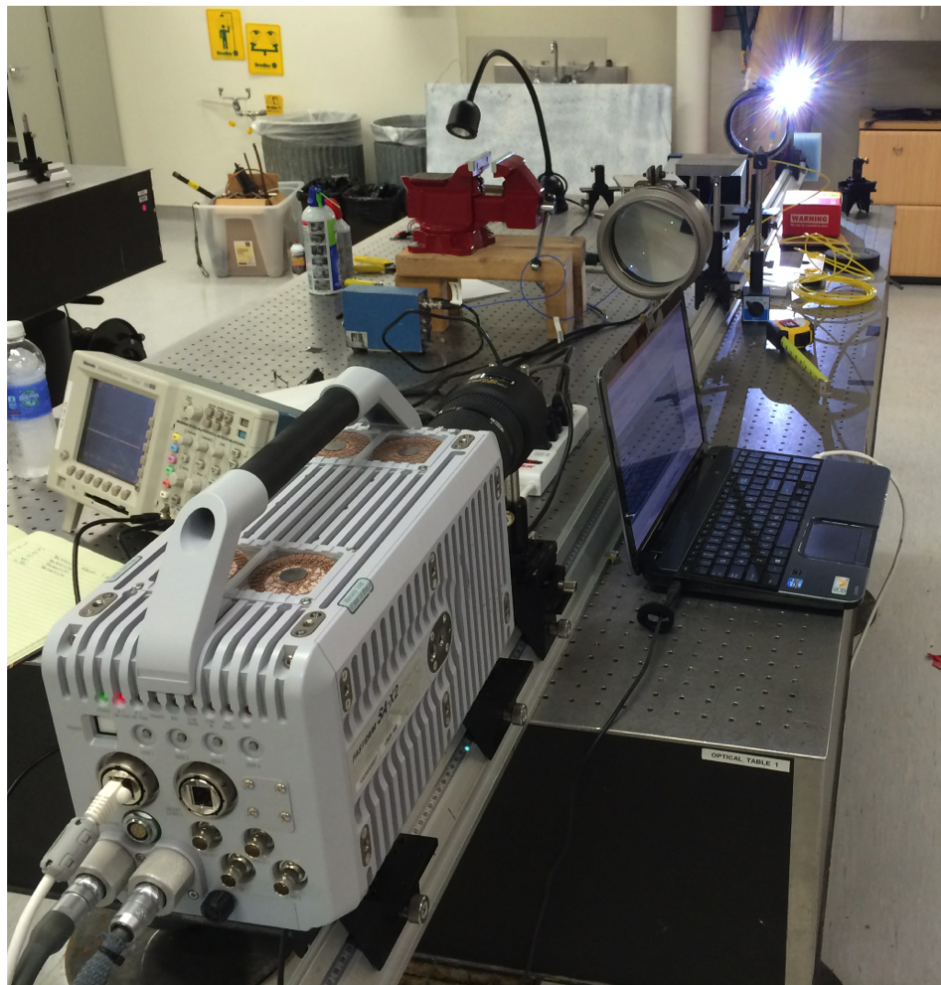
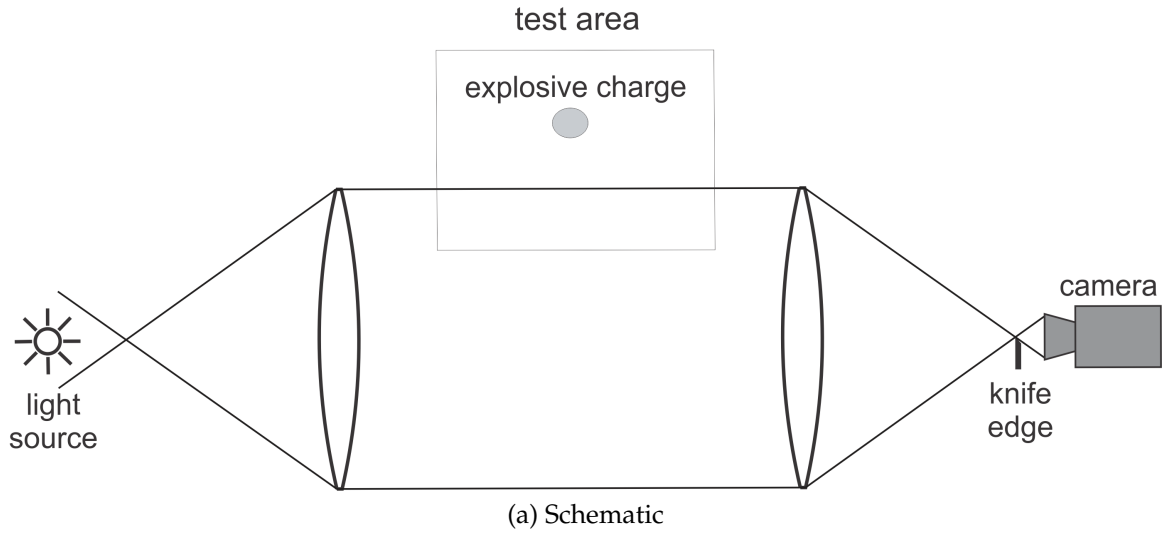


Figure 2.1: Schematic of dual-field-lens arrangement with area highlighted denoting placement of explosives (shotshell primers, NONEL shock tube, or Detasheet).

The light source must be a point light source, requiring either an LED or arc lamp, with extraneous light blocked from illuminating the lenses, test area and camera. The knife edge is placed at the focal point of the second lens, with the camera placed as close as possible to the knife edge in order to prevent additional cutoff from the camera lens itself. When the arc lamp was used, a neutral density filter was placed before the knife-edge in order to prevent overexposure of the image. Typical tests using this system are small in scale, making it ideal for laboratory use. It is possible to use this system in the field, though there is some inherent difficulty in using highly sensitive equipment in an unregulated environment. This system was used in all stages of testing described below, both in the laboratory and in the field.

## 2.3 Quantitative Schlieren Imaging

### 2.3.1 General Principles of Light Refraction

The general principles of the schlieren technique rely on the fact that light rays passing through a transparent medium are bent based on the spatial refractive-index gradients [16]. Light rays traveling towards an observer along the z-axis is bent towards the y-axis through some angle  $\epsilon_y$ , as shown in Figure 2.2.

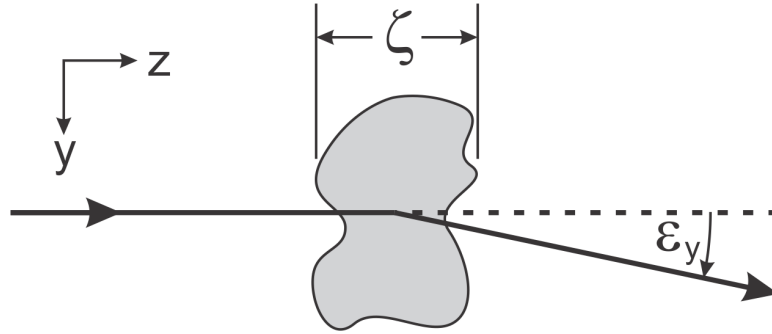


Figure 2.2: Diagram of light refraction through some schlieren object centered in the dual-field-lens schlieren setup.

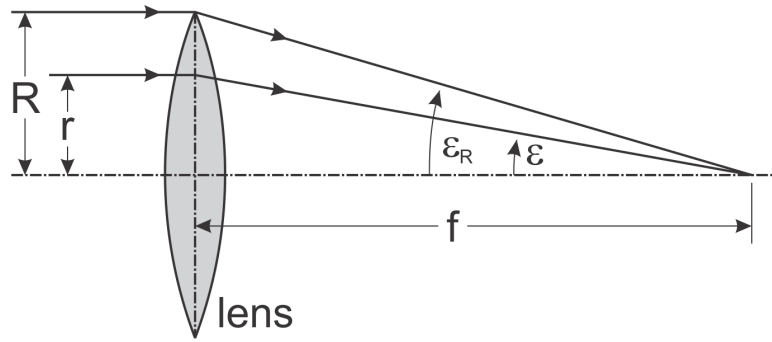
For a two dimensional schliere,  $\epsilon_y$  is directly related to the first spatial derivative of the refractive index,  $n$ , in the  $y$ -direction [16]. The refractive index is related directly to density using the Gladstone-Dale Law.

$$\epsilon_y = \frac{1}{n} \int \frac{\partial n}{\partial y} \partial z = \frac{Z}{n_\infty} \frac{\partial n}{\partial y} \quad (2.1)$$

$$n = k\rho + 1 \quad (2.2)$$

Equation 2.2 shows the direct correlation between refractive index and density, using the Gladstone-Dale constant for air,  $k=0.000226m^3/kg$ . The physics of refractivity lead to some small variability in  $k$ , which increases with increasing light wavelength [14]. However, the variability in  $k$  for most gaseous species are very weakly dispersive at different wavelengths in the visible range [23]. Therefore, variability in  $k$  is insignificant for experiments using visible light. The variable  $Z$  refers to the physical distance that light must travel through the schlieren object. This value can be constant or variable depending on the event being analyzed.

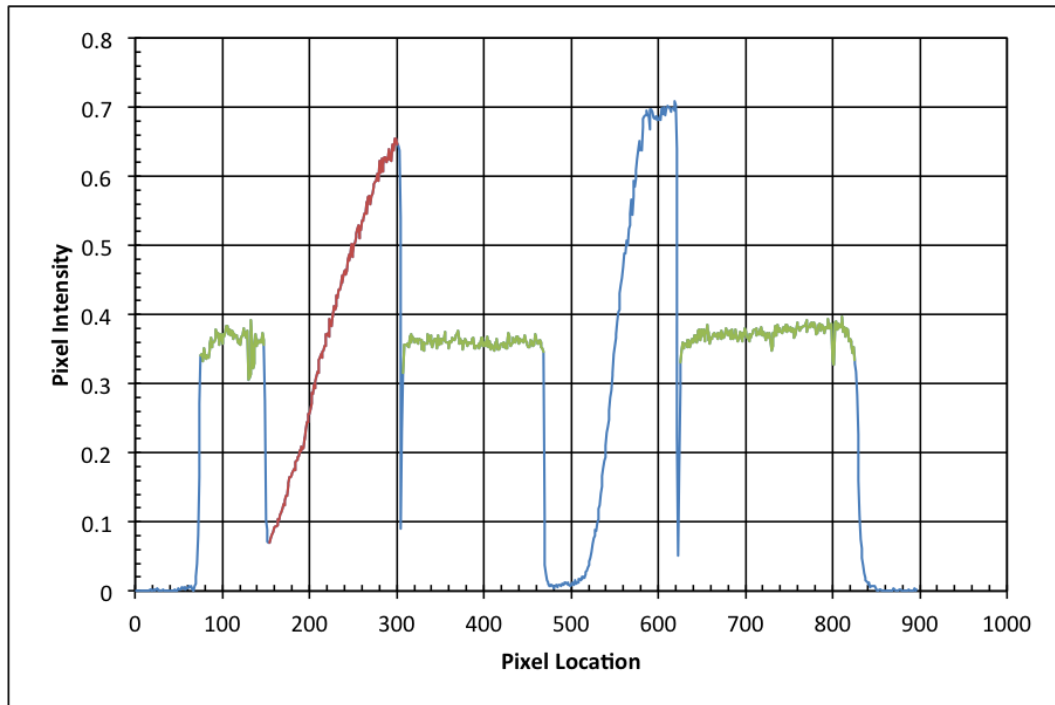
One of the key elements to analyzing the density-gradient field is being able to calibrate it to a known value. Here, a simple, weak, positive lens (long focal length) is used. The diameter of the lens is  $0.0254m$  and the focal length is  $10m$  for all primers and NONEL testing, and  $4m$  for Detasheet testing. Incoming light traveling through the lens will focus all light to a point. Light passing through the lens will be refracted through a maximum angle at the radius of the lens, with the angle decreasing to zero at the center of the lens, as seen in Figure 2.3. Note in Figure 2.3 that the background intensity is delineated in green, the  $10m$  focal length positive lens is in red, and the  $4m$  lens is in blue. As the focal length of the weak lens increases, the overall sensitivity of the weak lens increases. This fact is best described by Equation 2.3, which shows the relation between radius and focal length. As the focal length increases, the refraction angle  $\epsilon$  becomes smaller, meaning that the lens will be capable of resolving smaller refraction angles within the schlieren image. However, there is a trade off between sensitivity and the overall intensity range within the lens. Greater sensitivity will have a smaller range of maximum observed values, so care must be taken that the calibration lens' range will encompass the observed intensity values from the schlieren object.



(a) Lens Schematic



(b) Physical Image



(c) Lens Pixel Intensity

Figure 2.3: A) shows a diagram of light refraction through positive lens in the dual-field-lens schlieren setup; b) shows gradients across two lenses of 10m (on the left) and 4m focal lengths; c) shows an average of three horizontal rows of pixels taken from the center of the two lenses.

The small angle approximation is used with Equation 2.3 to relate the positive lens' radius to the focal length. Provided the focal length is sufficiently long,

this approximation is justified, which simplifies the overall calculations.

$$\frac{r}{f} = \tan \epsilon \approx \epsilon \quad (2.3)$$

A key point in this analysis is that the camera must be sharply focused on the plane on which measurements are made. This translates to the center axis of the explosive being used during testing. Therefore, the lens must be placed on the same focal plane. The overall range of intensity values observed in the lens is determined by the degree of cutoff. Too much cutoff will lower the image's overall grayscale. In some cases, using too much cutoff can lead to the schlieren object's intensity values zeroing out. Therefore, sufficient cutoff should be chosen based on test parameters. Sufficient cutoff implies that the range of intensity values observed within the lens utilizes a significant portion of the camera's useable dynamic range [21].

### 2.3.2 General Process for Determining the Density Field

The process for determining the density field from a schlieren object is relatively simple with the use of the calibration lens described above. First, the schlieren setup was optimized by placing the light source and knife edge at the focal points of the two field lenses. This will create the parallel light in the test section, and will result in uniform background illumination. This uniformity is key to analyzing deviations from the average background intensity. Next, a row of pixels is taken from images showing the calibration lens or the schlieren object. Some analyses have the calibration lens within the field-of-view during testing, though this is not necessary, provided the background intensity does not shift, multiple successive images can be compared to the calibration image.

In order to determine the density field around the schlieren object, the intensity values associated with the calibration lens must be analyzed. The average background intensity in the image is identified, along with the corresponding intensity in the calibration lens. This intensity's distance from the physical lens center is defined as  $r_0$ , which refracts through an angle  $\epsilon_0$  as defined by Equation 2.3. The  $r_0$  is determined by fitting a 5th-order polynomial to a plot of pixel intensity versus pixel location (see Figure 2.4). This polynomial is used with the average background intensity to determine  $r_0$ .

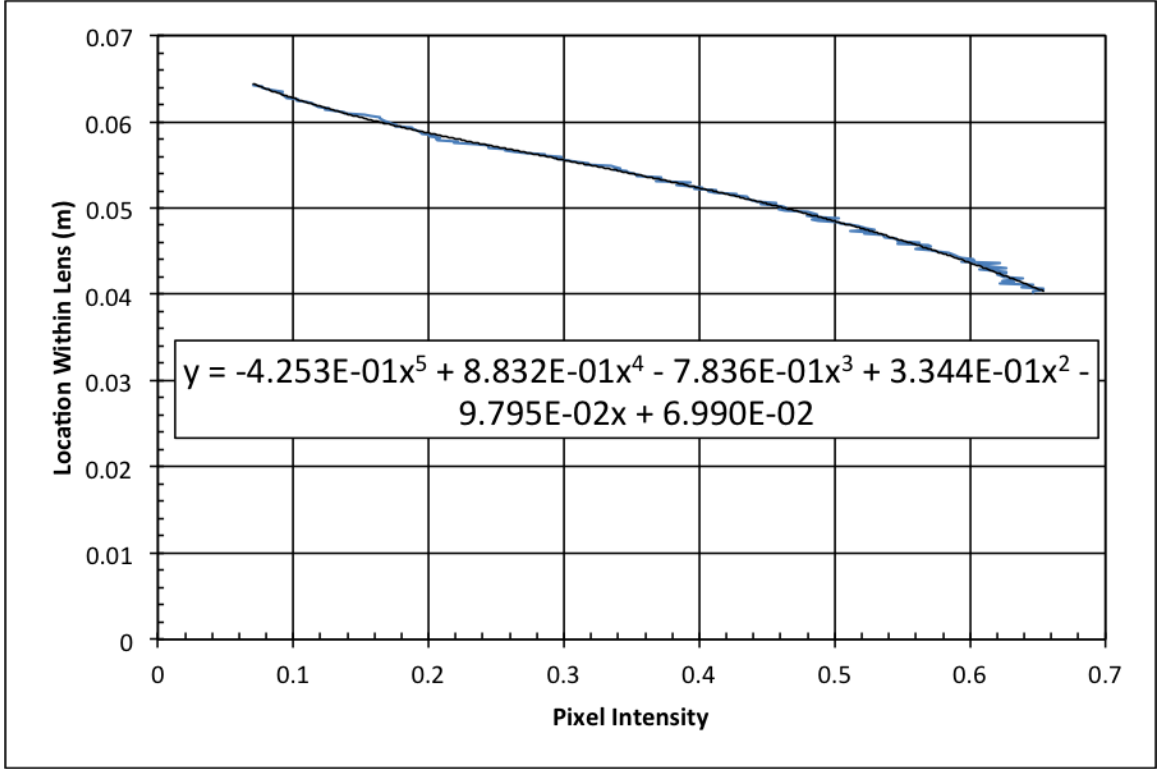


Figure 2.4: Calibration lens intensity and specific physical location with 5th-order polynomial fit.

The refraction angles within the schlieren image are determined using this same 5th-order polynomial to convert intensity into a corresponding physical location within the calibration lens. This location refracts light through some angle  $\epsilon$  using the small-angle approximation. The refraction in the image,  $\epsilon_{image}$ , is determined by relative refraction angle between  $r$  and  $r_0$ .

$$\epsilon_{image} = \epsilon - \epsilon_0 = \frac{1}{f}(r - r_0) \quad (2.4)$$

Here,  $\epsilon_{image}$  is equivalent to  $\epsilon_y$  described in Figure 2.2 and Equation 2.1. From Equation 2.1, the first derivative of the refractive index is determined, using known values for  $Z$  (dependent on the shape of the schlieren event) and  $n_\infty$ , a known constant dependent on the transparent medium being analyzed. The variable  $Z$  is dependent on the size of the schlieren object. For a flow that is constant into the plane of the image,  $Z$  is the physical distance into the image that the schlieren object effects. The refractive index field is then derived by integrating the refractive index gradient from infinity, or atmospheric conditions. Finally, the density field is reconstructed using Equation 2.2.

## 2.4 Explosive Material

Lab testing was done using Remington 209 Premier STS primers and cut lengths of NONEL Lead Line shock tube, and field testing was done using Detasheet. During testing, efforts were made to ensure that the environment was as controlled as possible. In the lab, the air was kept at a constant temperature and all vents were shut off to prevent air currents. In the field, testing was conducted in a large bunker and doors were kept closed during testing; the air temperature was measured for each test. The explosive compound in the Remington primers is primarily lead styphnate along with other metal fuels. The lead styphnate composes 1-26% of the primer's explosive compound, with copper, zinc, antimony, arsenic, iron, barium, and tetrazene as additional compounds. The primers were fired using a pin mechanism which crushed the compound, igniting the material and generating a shock. The NONEL shock tube is composed of a mixture of cyclotetramethylene-tetranitramine (HMX) and aluminum (Al) powder inside a small diameter, three-layer plastic tube. A small amount of the explosive material coats the innermost tube. Shock tube is primarily used as a nonelectric detonator, which initiates an explosive by transmitting a shock down the length of the tube. It is a safe material with a wide variety of initiation applications. HMX, or octagen, is a powerful primary explosive and is used primarily in military applications. Some common applications include use as a detonator, the main compound in shaped charges, and as rocket propellant. Overall, the compound is relatively insensitive. Detasheet, which contains approximately 80% pentaerythritol tetranitrate (PETN), was cut and rolled into balls roughly 1g in weight. Preparation of the charges took place on-site. PETN is a common military explosive frequently used in blasting caps. The compound is well documented, with a known TNT equivalence [24]. PETN is a secondary explosive, requiring a shock impulse in order to detonate. An exploding bridge-wire detonator (EBW) was used to detonate the charges. The charges were secured to the EBW using a small amount of tape. An attempt was made to prevent the tape from facing the schlieren setup, thereby minimizing fragments passing through the field-of-view ahead of the explosive shock wave.

For all testing, the charge was suspended in air in order to prevent reflections from the table surface or the ground from interfering with the initial shock wave reaching the schlieren system (Figure 2.1). In the case of the NONEL, the end of the tube was secured in order to prevent movement during firing. In order to ensure accurate imaging of the shock passed through the schlieren test area, the charge was placed roughly center between the two field lenses. The charge was offset some distance to the side of the schlieren apparatus but was kept along the same center axis.

## 2.5 Pressure Gage Measurements

The gages are a small metal housing holding small crystal discs. These crystals respond to compressive loading and generate an electrical signal that

can be directly converted to pressure [11]. The gages are capable of resolving the pressure duration, recording both positive and negative impulses relative to the atmospheric pressure. However, these gages often fail to resolve the initial peak pressure accurately, particularly as the shock's Mach number increases [11].

An important aspect of this research is the ability to verify the accuracy of the deconvolution technique in reproducing the pressure signal across the shock [6]. A 50 psi PCB Piezotronics model 102 A07 SN 19907 pressure gage and a Textronix Digital Oscilloscope model TDS 3034B were used to measure the pressure signals. A single pressure gage was placed at a set position within the field-of-view to allow close comparison between the gage signal and the pressure signal derived from the deconvolution. Side-on pressures were collected by inserting the gage into an aluminum plate. The plate was cut at an angle on the leading edge to allow the shock to travel over the gage without interference from reflections (see Figure 2.5). A typical pressure trace is shown in Figure 2.6. The pressure trace shows the arrival of the initial shock, followed by a slight negative pressure. The additional noise following the complete shock signal is due to both vibrations within the plate and the detonation gases.

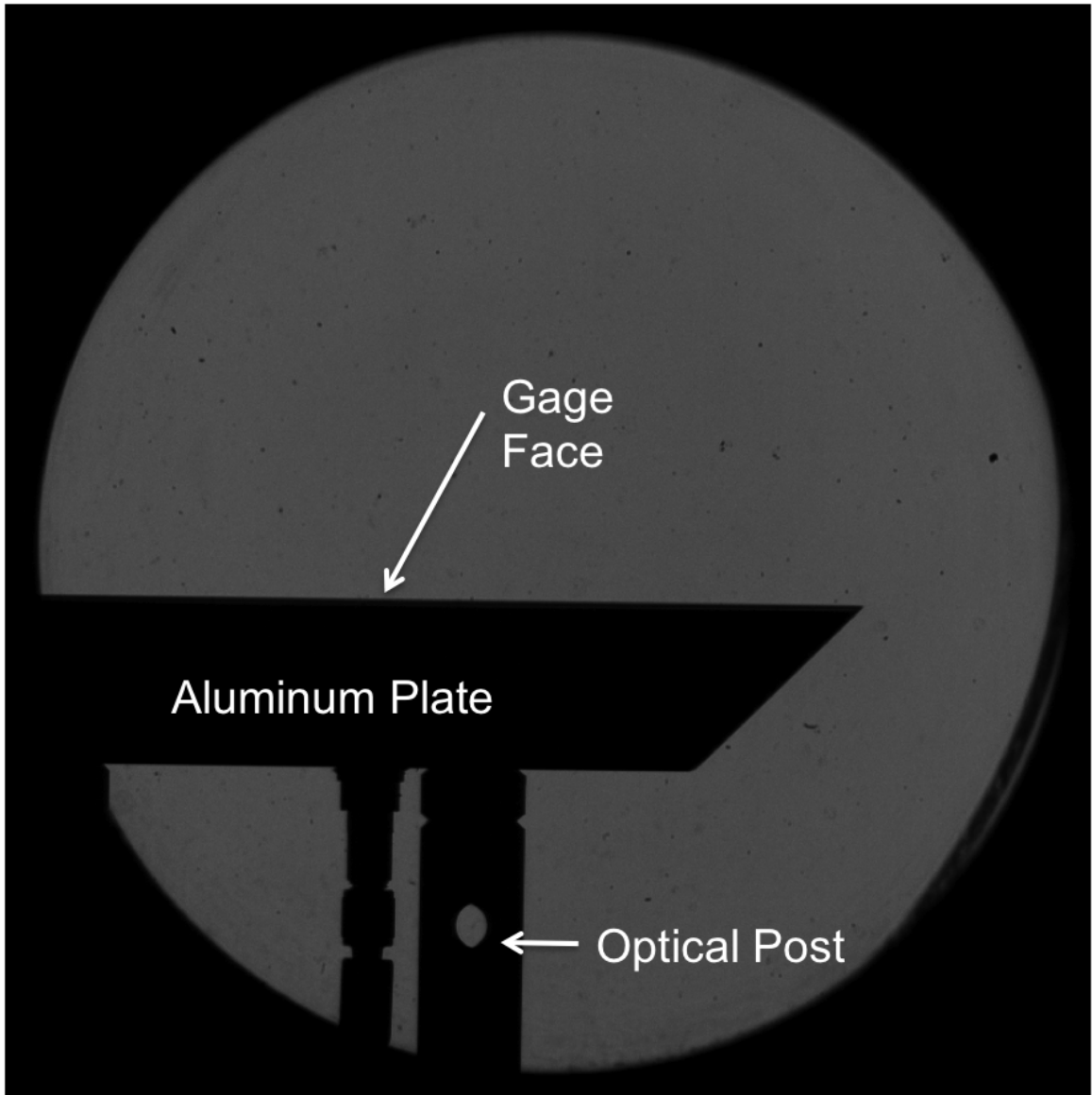


Figure 2.5: Piezoelectric gage location within dual-field-lens schlieren setup. The gage is secured within an aluminum plate. The edge of the plate is diagonally cut to allow shock to travel over top surface without reflecting off plate surface. In this orientation, the shock will be coming from the right.

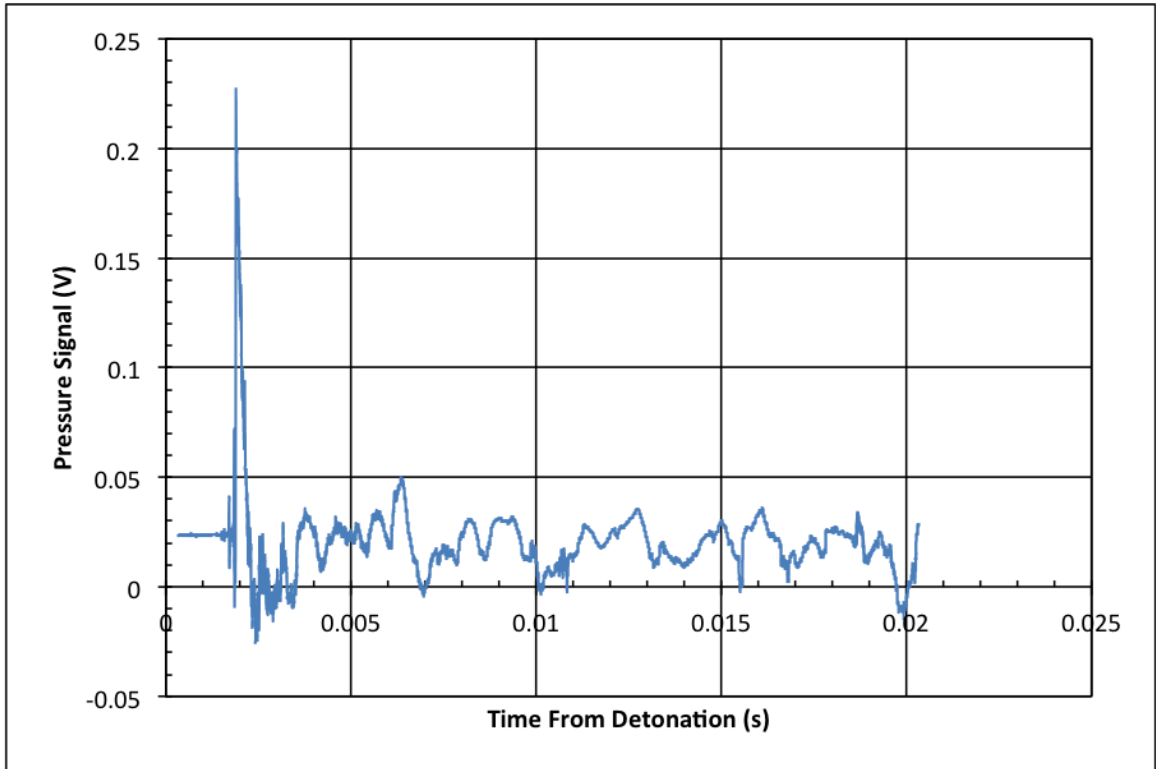


Figure 2.6: Standard pressure trace from the detonation of Detasheet using 50 psi piezoelectric gage for data collection.

While it is necessary to utilize pressure gages in order to provide a benchmark against the optical pressure values, there is some degree of uncertainty associated with the pressure gages. There is noise from various sources, though in general the shape and expected characteristics are clear. However, noise is present immediately prior to the shock wave's arrival, which can lead to difficulty differentiating the beginning of the shock from signal noise. This noise is due to shock impingement on the aluminum plate causing vibrations within the metal. Also, the gage cannot fully resolve the peak pressures predicted by compressible flow relations [6]. Additionally, the gage response time is slower than the shock wave speed, resulting in some delay between the shock arrival and the peak pressure. The final drawback associated with the gages is the limited number of data points available. Depending on the oscilloscope and the settings used for testing, the number of data points can be limited, leading to poor data resolution.

## 2.6 Shock Wave Imaging

The process for imaging shock waves uses the same dual-field-lens setup and determines the refraction angles using the same method described in Sec-

tion 2.3.2. As a shock causes a rapid increase in pressure, temperature and density, the assumption of a constant temperature cannot be used. Previous studies show that both pressure and temperature decay exponentially, but assume that the temperature decays sufficiently slowly so as to be considered constant compared to the pressure decay [21, 25]. Compressible flow relations were used to determine the temperature at the shock wave and this temperature was assumed constant behind the shock for initial analysis, but other temperature profiles were also investigated. Additionally, while the same process of determining the refraction angle,  $\epsilon_y$ , is used, an additional deconvolution of the data is necessary in order to account for the spherical nature of the event.

### 2.6.1 Digital Image Processing for Pressure Measurement

Initial processing of the experimental data requires the determination of the Mach number of the shock. Knowing the Mach number allows for the determination of the theoretical pressure and temperature at the shock wave. This information is necessary for later processing and allows for the experimental pressure field to be compared against some known theoretical value. The Mach number is determined by relating the pixel size to some known physical length using a calibration object. For this, the calibration object used was the calibration lens, either by itself or secured within a frame of known diameter. Inspection of the calibration lens provides the length of the object in pixels, which determines the *length/pixel* ratio.

The physical distance the shock moves between frames is then divided by the time between frames, which is a constant value based on the frames per seconds (fps) setting chosen for the high-speed camera. For the majority of the experiments conducted, the explosive event occurred at distances great enough that the shock travelled fairly constantly through the field-of-view, close to Mach 1.

Initial analysis of an explosive event utilizes a Matlab program to track spherical shocks. The program takes a sequential series of gray-scale schlieren images from the camera and user-variables to track the shocks position and determine the Mach number between images. Below, a typical shock tracking routine is shown. The initial image designates the location of the explosive center, with sequential images highlighting the position of the shock. The analysis focused on a shock wave, so imaging the detonation of the explosive was not necessary. Therefore, the explosive center is chosen as the edge of the field-of-view in the image immediately prior to the shock entering the field-of-view. This does not affect the programs ability to track the shock and will generate accurate velocity data everywhere except between the first and second images. However, distances from the charge center reported by the program will not be accurate with the artificial explosive center. Therefore, the distance from the charge center to some established point in the field-of-view must be known for later processing. Note

that the spherical white line will not align with the edge of the shock, except along the horizontal axis.



Figure 2.7: Example of shock track routine using a non-sequential series of images from the detonation of NONEL. Time step between sequential images is  $8.3\mu s$ . The white line is generated by the tracking program; the black line is the shock imaged by the dual-field-lens schlieren setup, though it is mostly obscured by the tracking program. The program tracks backwards in time towards the detonation center. Note the subsequent misalignment of the shock tracking line and the shock profile; this is caused by purposefully incorrect placement of the charge center. Images are not sequential.

The program begins tracking the shock at the end of the images specified by the user. It then steps backwards in time towards the charge center, looking for the low intensity value denoting the leading edge of the shock. This low intensity value is lower than threshold intensity determined by the average background intensity. The program is capable of tracking the leading edge automatically, though there is a manual option for adjusting the leading edge in individual images. This option is preferable in tests that involved significant fragmentation, which create oblique shocks that can interfere with the automatic tracking option. This process repeats until the first image is reached, generating a streak

image and plots of the Mach number. An output file is also generated, which includes shock position, Mach number, the speed of sound in air, other supplied atmospheric constants, as well as uncertainties for the generated values.

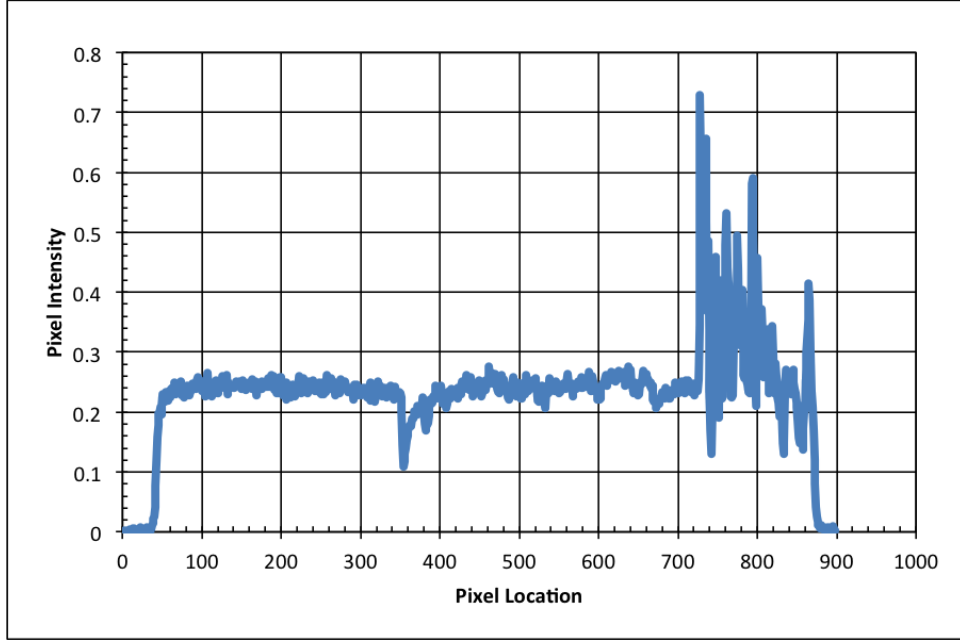
Once the Mach number is known for all images of interest, rows of pixel intensities along the horizontal plane of the shock were extracted and, in some cases averaged, in order to determine the refractive index described in Section 2.3.2.

### 2.6.2 Abel Deconvolution Process

The intensity values across the shock are used to determine the deflection angle,  $\epsilon_y$ , by comparing it to the calibration lens. An example of the pixel intensities across a shock is shown below in Figure 5.14. However, due to the schlieren systems parallel light passing through the spherical shock, the refractive-index gradient field defined in Equation 2.1 are path-integrated quantities. Therefore, a deconvolution of the deflection data,  $\epsilon_y$ , is necessary in order to reproduce the local density field from the integrated quantities seen in the image plane of the camera[21, 26]. For an axisymmetric object such as spherical shock, the Abel inversion method is sufficient to reproduce the field from its 1D representation in the schlieren image.



(a) Shock



(b) Pixel Intensity

Figure 2.8: Row of pixel intensities across a shock from the detonation of NONEL.

Several different Abel inversion methods exist, each with varying degrees of accuracy and uncertainty. These methods are the 1/3rd rule, the 1-point formula, the 2-point formula and the least-squares approximation. Among these, the 2-point formula described in Equation 2.5, 2.6, and 2.7 is preferable, as it has the best inversion accuracy with the least amount of error [26]. The deflection data is calculated as outlined in the flat plate analysis and is input into the Abel inversion method. The Abel inversion method considers a range of data from the center outwards of a spherically symmetric object. Therefore, intensity data points outside of the visible range were artificially filled with background intensity values [21]. This results in zero deflection for non-visible data points. Adding these artificial points is necessary in order for the inversion method to work properly.

The indices  $i$  and  $j$  correspond to data points between 1 and  $N+1$ , where  $N$  represents the total number of data points.  $D_{ij}$  contains the independent data-spacing linear operator coefficients specific to the 2-point method [26]. A simple Matlab code was written to perform the mathematical operation outlined below. The code takes the deflection data in vector form and runs it through the code. The output  $\delta$  will be plotted against the radius, with the distance between data points determined by the pixel calibration constant for an individual test.

$$\delta(r_i) = \sum_{j=i}^{N+1} D_{ij} \cdot \epsilon_j \quad (2.5)$$

$$\begin{aligned} D_{ij} &= \frac{1}{\pi} \cdot (A_{ij} - A_{i,(j-1)} - j \cdot B_{ij} + (j-2) \cdot B_{i,(j-1)}) \\ &\quad \text{if } j > i \text{ and } j \neq 2, \\ &= \frac{1}{\pi} \cdot (A_{ij} - j \cdot B_{ij} - 1) \\ &\quad \text{if } j > i \text{ and } j = 2, \\ &= \frac{1}{\pi} \cdot (A_{ij} - j \cdot B_{ij}) \\ &\quad \text{if } j = i \text{ and } i \neq 1, \\ &= 0 \\ &\quad \text{if } j = i = 1 \text{ or } j < i \end{aligned} \quad (2.6)$$

where  $A_{i,j}$  and  $B_{i,j}$  are

$$\begin{aligned} A_{i,j} &= \sqrt{j^2 - (i-1)^2} - \sqrt{(j-1)^2 - (i-1)^2}, \\ B_{i,j} &= \ln \left( \frac{j + \sqrt{j^2 - (i-1)^2}}{(j-1) + \sqrt{(j-1)^2 - (i-1)^2}} \right) \end{aligned} \quad (2.7)$$

The refractive index  $n$  is reproduced from the 2-point output  $\delta$  using Equation 2.8. Equation 2.2 is used to reproduce the density field. Once the density field has been reconstructed, the ideal gas law can be used to calculate the pressure field from Equation 2.9.

$$\delta = \frac{n}{n_0} - 1 \quad (2.8)$$

$$P = \rho R_{air} T \quad (2.9)$$

For the Abel inversion method to be successful, the shock must be traveling at speeds that allow the ideal gas assumption to hold. At speeds above Mach 5, ionization and molecular dissociation begin to occur in the gas species. The ideal gas law cannot be used when interactions between molecules becomes significant. During testing, Mach numbers were all under Mach 2, making this assumption valid. Additionally, the shock must be clearly separated from the detonation gases in order to allow an accurate deconvolution. A wide separation

will also permit the complete pressure profile to be calculated. In addition, one of the major disadvantages of the Abel technique is the assumption that all deflection is solely caused by a purely spherical schlieren object. Any deflections caused by oblique shocks formed by fragments will remain in the deconvolution results, despite the fact that the fragments may not be traveling in the plane of interest. Therefore, the shock must not only be cleanly separated from the detonation gases, but it also must not have any oblique shocks interfering with the region of interest.

## CHAPTER 3

### FLAT PLATE ANALYSIS

A simple flat plate analysis was used to test the method of deriving the density field. A comparison of experimental and theoretical results was used to verify the accuracy of the technique. A vertical flat plate placed in the field-of-view was heated to achieve steady, laminar flow and imaged using a digital Nikon SLR camera (see Figure 3.1). For this test, the light source in the dual-field-lens setup was an LED. As this is not a high-speed object, only a single image is needed for data analysis. The resolution was chosen to image the entire field-of-view in the schlieren system. The temperature of the plate was measured multiple times during heating to find the steady temperature. The temperature of the plate was deemed steady once the temperature did not vary over a time period of 10 minutes. The temperature was tested at several locations across the plate. Once a steady temperature of  $325 \pm 1K$  was achieved, the flat plate was imaged for processing in Matlab. The density-gradient field around the flat plate was a direct result from the change in air temperature. Therefore, applying the ideal gas law (see Equation 2.9) was a simple matter of determining density from the refractive-index gradient using the method described above to determine density, then using atmospheric pressure to calculate the temperature field. The theoretical profile was derived using the method described by Ostrach [27]. The theoretical temperature profile is compared to the experimental temperature profile (Figure 3.2). The good agreement between the experimental measurement and the theoretical calculations demonstrates that the technique used to reconstruct the density field is accurate.



Figure 3.1: Setup of heated flat plate.

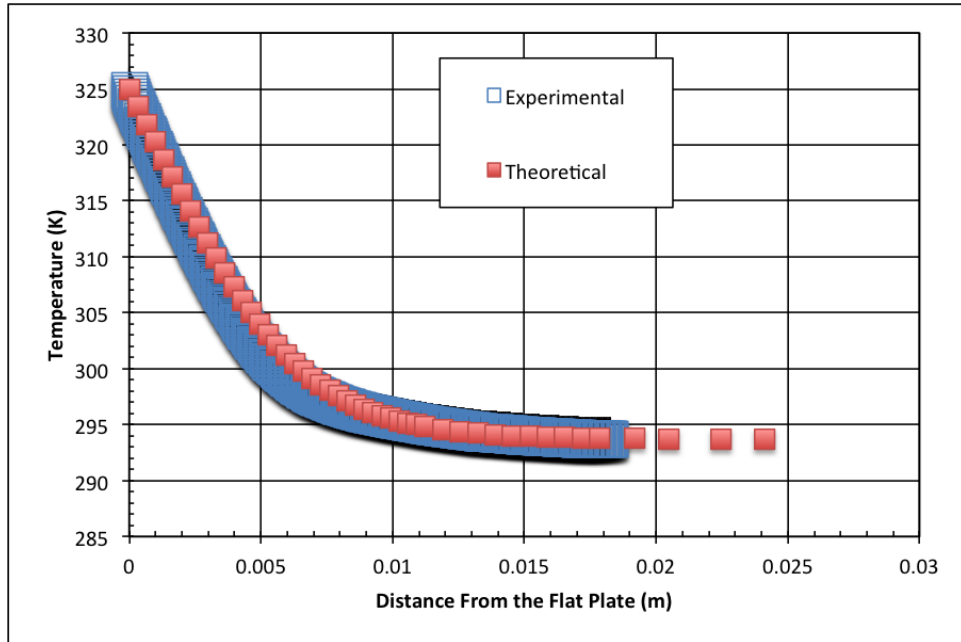


Figure 3.2: Comparison of flat plate temperature profiles of theoretical and experimental measurements. Uncertainty of experimental temperature is  $\pm 2K$ , denoted by the size of the data points (blue).

As the background intensity has some noise, several rows of pixel intensities were averaged to create a smoother signal. While this method does smooth out the inherent noise, this can reduce peak intensities in certain situations where the intensity is non-uniform vertically. In the case of the flat plate, the flow is laminar and the peak temperatures are not extreme, so this averaging is not expected to cause significant peak reduction. For spherical shocks, care must be taken that the area analyzed is uniform vertically. To accomplish this, the charge center must be approximately in line with the center of the field-of-view. The shock will have expanded sufficiently to allow for a uniform surface over several rows of pixels within the field-of-view.

## CHAPTER 4

### CTH MODELING

The CTH software package developed by Sandia National Labs is used here to model the detonation of 1g of PETN. Access to the software was provided through the Energetic Materials Research and Testing Center (EMRTC). PETN is well-understood, making it suitable for use as a standard explosive for comparative purposes. The simulations are used to support the experiments in this work. CTH is a versatile hydrocode specializing in modeling multi-dimensional, multi-material, large deformation, strong shock wave physics [28]. The meshes used range from 1D to 3D rectangles, spheres and cylinders. The user has the option of choosing multiple tabular or analytical equations of state for any material. CTH can model detonation, fragmentation, elastic-plastic behavior and can track fragments smaller than the computational cell [28]. As the present study focuses on spherical, axisymmetric detonations, a 1D representation is sufficient for accurate modeling. The explosive material PETN is placed at one end of the mesh, allowing the shock wave and detonation gases to travel left to right through the mesh. The mesh was set to allow the material to flow freely out of the system without reflecting off the boundaries. The computation was run out to a distance of 2m and consists of 2000 equally spaced cells, providing a mesh resolution of 1mm. Tracers were placed every 10mm out from the center, recording velocity, pressure and temperature data (see Figure 4.1).

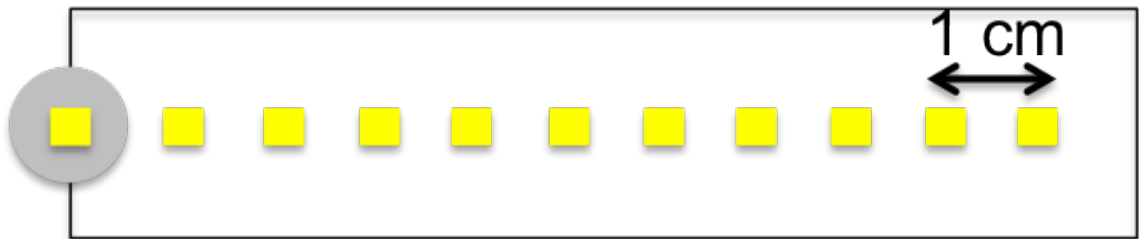


Figure 4.1: Schematic of CTH model. PETN is in gray, tracers in yellow. Total region modeled extends to 2m.

The tracers were used to record the shock time of arrival and the overpressure and pressure duration. The temperature was also recorded and the rate of exponential decay was compared to the pressure decay. This comparison was

used to analyze the applicability of the assumption of constant temperature behind the shock. The air surrounding the PETN was modeled as an ideal gas and the PETN was modeled using Jones-Wilkins-Lee equation of state for high explosives.

One of the primary goals of the CTH analysis was obtaining an accurate temperature profile to use when determining the shock overpressure and pressure duration from the density field. Previous research has made the assumption that the temperature profile's relative rate of decay is slow enough to be considered constant when compared with the rate of decay of the pressure profile [21]. This assumption may hold true close to the center of the explosive, however, CTH modeling indicates that after a certain point, the relative rates of decay of pressure, temperature, and density are roughly equivalent.

While CTH has been known to inaccurately calculate temperature, the relatively slow Mach numbers being analyzed here allow the assumption that the temperature profiles are appropriate. The goal of the CTH analysis is to guide the shape of the temperature profiles and to serve as a benchmark for experimental comparison. The peak temperatures are accurate, as they are calculated using Rankine-Hugoniot jump conditions across the shock wave. The temperature decay profile is expected to be reasonably accurate. This assumption is shown to be accurate by comparison to experimental results.

Tracer data was analyzed at select distances from the PETN charge center (see Figures 4.3 and 4.4). The data was normalized to bring the relative values of temperature, density, and pressure onto a [0,1] scale along the y-axis (Figures 4.6, 4.7, and 4.8). The general equation for temperature is shown in Equation 4.1; pressure and density are normalized using the same equation. Distances were chosen to reflect a shock still coupled to the explosive fireball, as well as a shock that had clearly separated from the slower moving detonation gases. The exact distances chosen for these separated shocks were chosen to correspond to physical data collected from primers and Detasheet. In the figures below, negative normalized values indicate below atmospheric conditions.

$$T^* = \frac{T - T_{atm}}{T_{max} - T_{atm}} \quad (4.1)$$

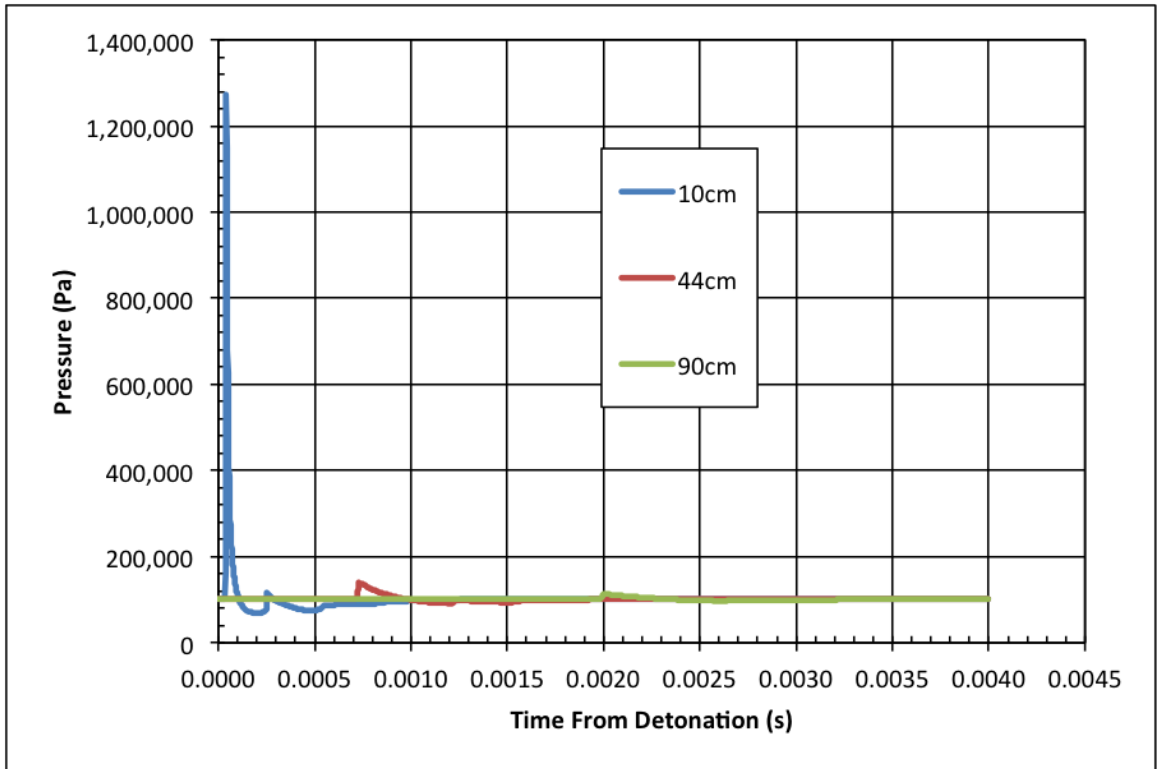


Figure 4.2: CTH pressure output of 1g PETN detonation, 10cm, 44cm, and 90cm from charge center.

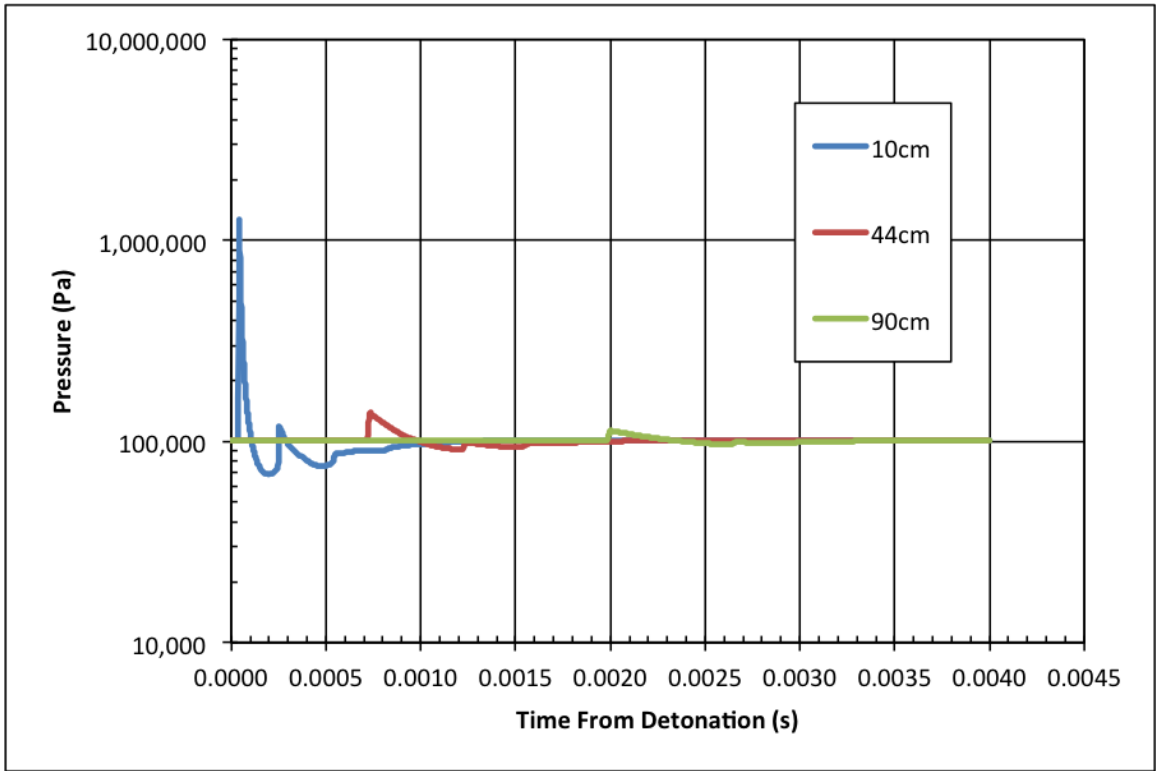


Figure 4.3: Logarithmic scale of CTH pressure output of 1g PETN detonation, 10cm, 44cm, and 90cm from charge center.

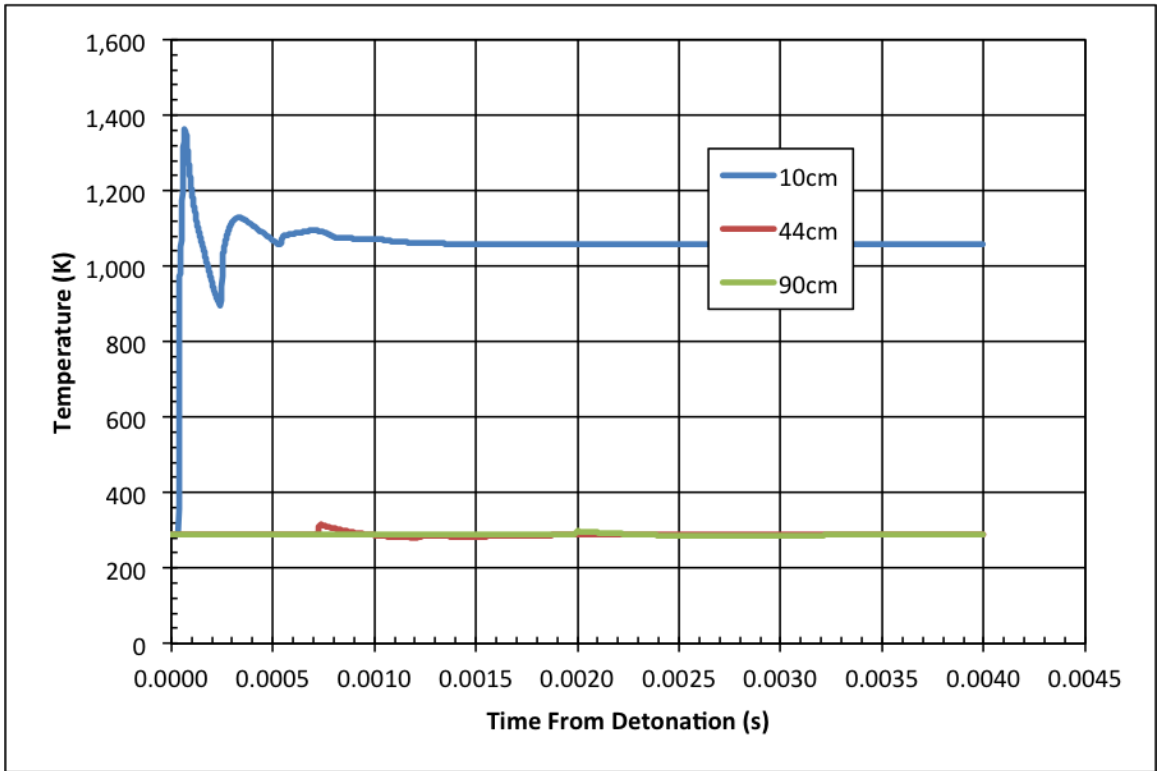


Figure 4.4: CTH temperature output of 1g PETN detonation, 10cm, 44cm, and 90cm from charge center.

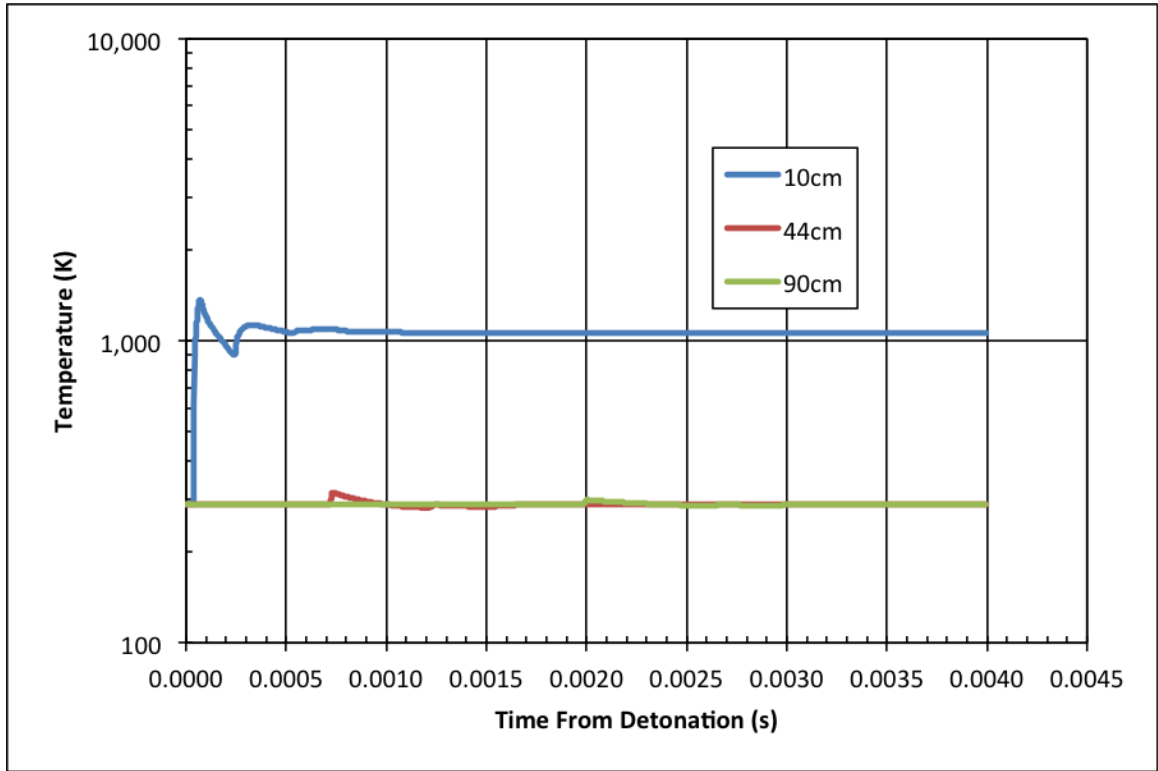


Figure 4.5: Logarithmic scale of CTH temperature output of 1g PETN detonation, 10cm, 44cm, and 90cm from charge center.

Previous work done by Hargather [22] suggests that the shock will be coupled to the fireball and detonation gases within 0.1m of the charge center. This is most clearly seen in Figure 4.4, where the air is shocked to an elevated temperature and fails to decay to atmospheric conditions due to the following detonation gases. To separate the effects of the shock from the effects of the fireball and detonation gases, the temperature profiles were used as the clearest indicator of the position of the fireball. The shock profile is clearly distinguishable at the front due to the sharp rise and fall, as well as the characteristic shape. The leading edge of the fireball can be roughly estimated to exist at some point between 0.0005 and 0.001s post detonation, as seen in the data taken at 10cm from the charge center. Therefore, for all tracer data where the shock temperature failed to decay to atmospheric conditions, the fireball can be assumed to influence the temperature profile. The fireball's position within the temperature profile can also be used to verify the position within the density and pressure profiles, which determines how much of the data at an individual tracer location can be assumed to result solely from the shock's influence.

Normalizing the tracer data at 10cm from the PETN charge center shows a clear trend of the pressure profile rapidly decaying with the temperature profile remaining fairly constant (see Figure 4.6). The odd peak in the temperature profile is an output from the CTH simulation, and may be attributed to the fireball. Therefore, data collected in this region is better served using the constant

temperature assumption.

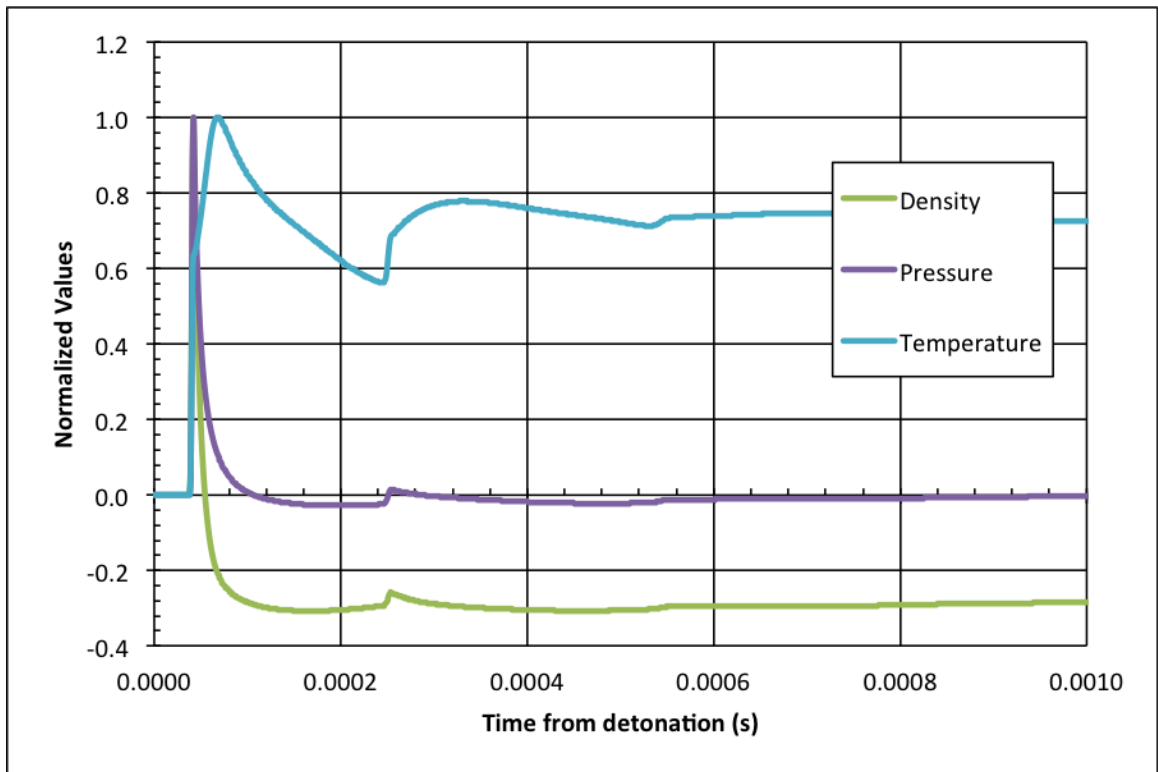


Figure 4.6: Normalized CTH output of 1g PETN detonation, 10cm from charge center.

However, one of the key elements to optically reproducing the complete pressure profile is to have a shock cleanly separated from the detonation gases. The gases have a different chemical makeup, so have a different refractive index. This change in refractive index between gas species cannot be accounted for in the schlieren process, thus the technique is limited to single gas environments. Therefore, analyzing data this close to the charge's center only yields peak pressure data, while neglecting the complete profile. Therefore, analyzing the simulation trends at greater distances is useful, as the shock can be observed to begin separating from the detonation gases after 0.2m [22]. Here, distances at 44cm and 90cm are chosen, as these distances correspond to the range of distances experimentally analyzed using Detasheet. Additionally, data taken at tracer 44 can be scaled and compared to primer data.

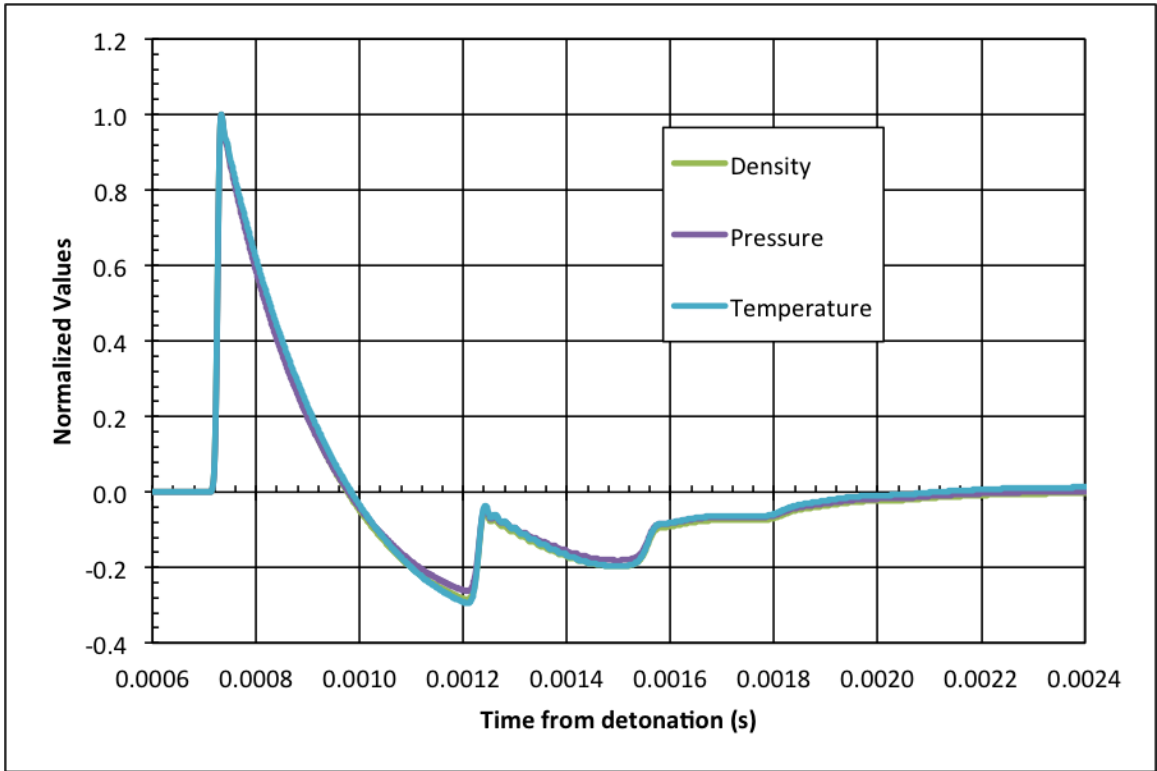


Figure 4.7: Normalized CTH output of 1g PETN detonation, 44cm from charge center.

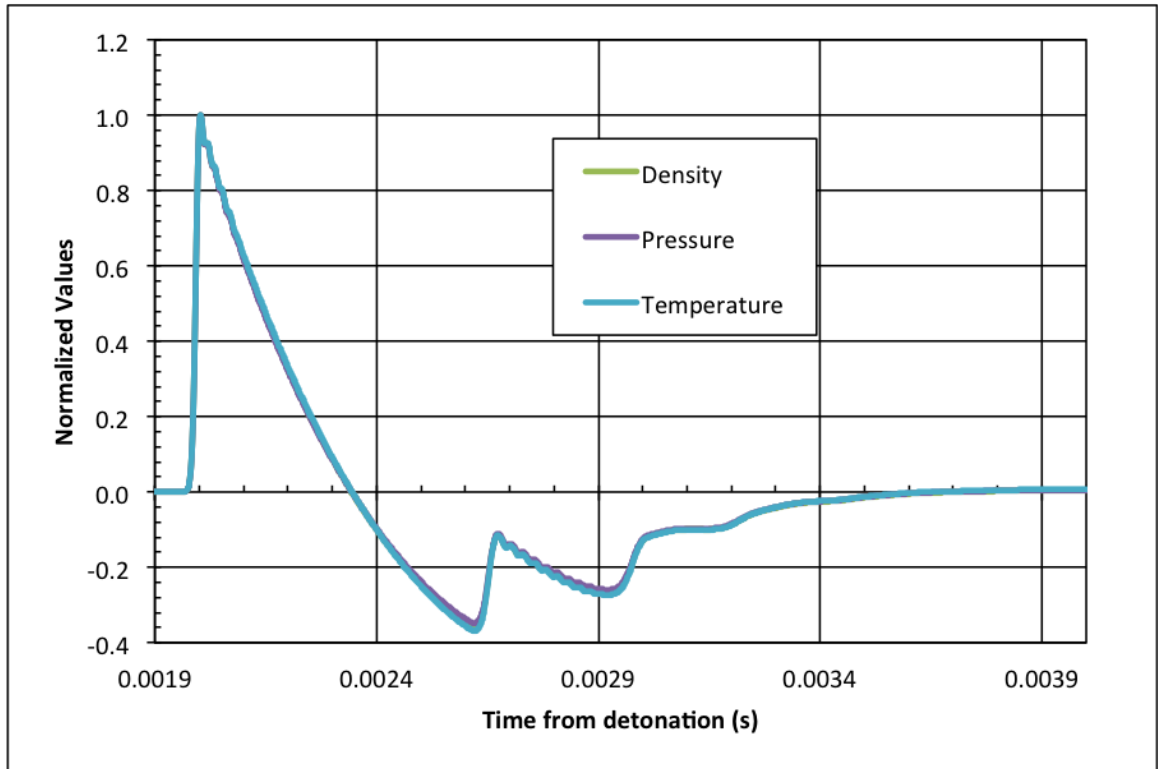


Figure 4.8: Normalized CTH output of 1g PETN detonation, 90cm from charge center.

The normalized results in Figures 4.7 and 4.8 clearly show at distances where the shock is traveling free from the fireball and detonation gases, the relative trends of exponential decay are nearly equivalent. To verify this behavior, the ideal gas law was used to determine the gas constant  $R$  with the pressure, density, and temperature data at each point;  $R$  was calculated and remained constant. The observed decay in density, temperature, and pressure are also of the same general shape to the non-dimensional pressure, temperature, and density profiles calculated from theoretical analysis [29, 30]. Therefore, accurate determination of the pressure field from density requires a new temperature profile.

As mentioned above, the data in Figure 4.7 can be scaled to correspond to data collected from the detonation of primers. The mass of the primers, approximately 0.0551g, was treated as the standard mass. The PETN radius and time data was scaled using Sach's Scaling (see Equations 4.2 and 4.3), which was developed to relate explosions of different masses in different atmospheres. The PETN impulse duration was scaled by relating the temperature, density and pressure data to the scaled time calculated using Sachs scaling methods. The radius from the charge center is  $r$  and  $W_{std}$  is the mass of the standard charge, which is the primer mass. The Sachs scaling method is accurate for charge masses on the order of 1mg, [31]. As scaling is accurate down to masses on the milligram scale, it is unnecessary to run separate CTH simulations for spherical PETN of the same magnitude as the primer explosive compound. Variables with an  $s$  subscript are

scaled. The 1g PETN charge was scaled to the size of the primer, resulting in the data at tracer 44 being compressed to a radius of 16.74cm. The new temperature profile is presented below in Figure 4.9.

$$R_s = \frac{r}{S} \quad (4.2)$$

$$t_s = \frac{ct}{S} \quad (4.3)$$

$$S = \left(\frac{W}{W_{std}}\right)^{1/3} \left(\frac{101325Pa}{P}\right)^{1/3} \quad (4.4)$$

$$c = \left(\frac{T}{288.16K}\right)^{1/2} \quad (4.5)$$

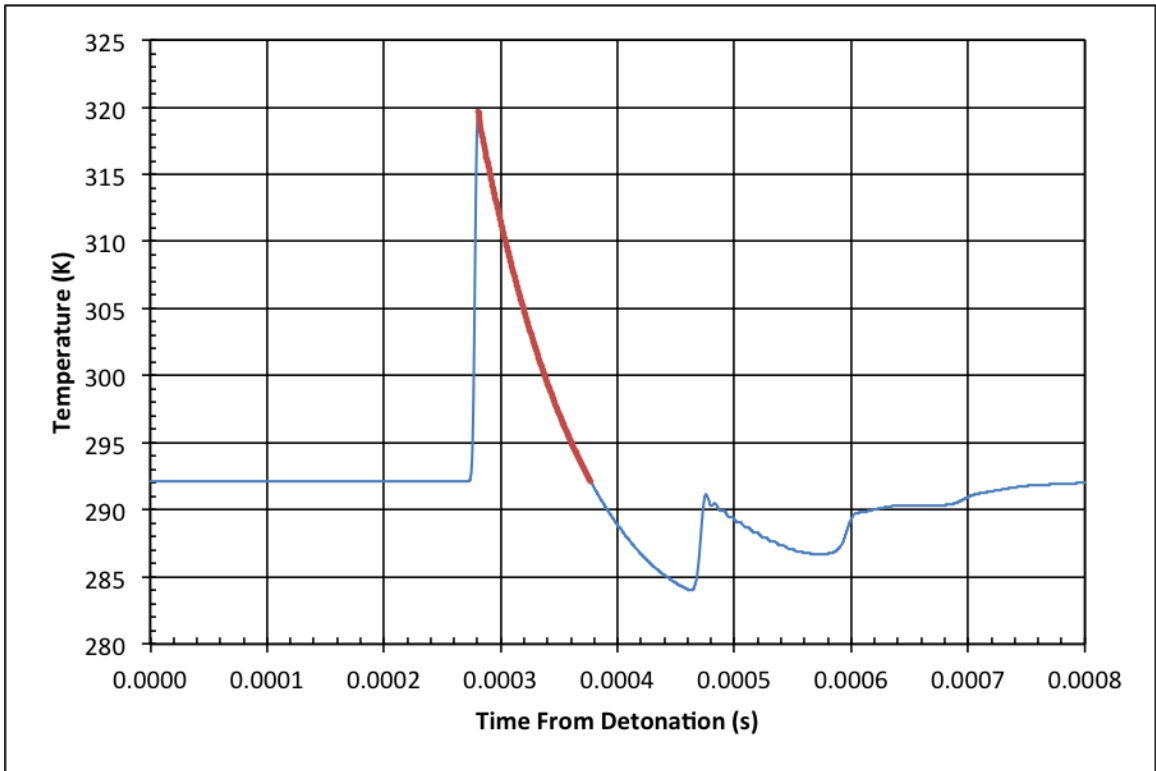


Figure 4.9: Scaled CTH output of 1g PETN detonation, 44cm from charge center.

In order to generate a temperature profile for comparison to optical data, only a subset of the CTH data was analyzed. The subset ranged from the peak value centered at roughly 0.28ms to a low value at 0.45ms and is highlighted in red in Figure 4.9. This portion of the temperature curve was selected for further

pressure calculations using experimental density values because it only takes the primary shock into account, while ignoring the secondary shock. The secondary shock is not observed in the primer tests due to the asymmetric explosion of the shot shells. This temperature curve will be compared to other temperature profiles in the next chapter.

## CHAPTER 5

### EXPERIMENTAL RESULTS

Several different types of explosives were analyzed for the ability to accurately determine temperature and pressure profiles peak pressure and pressure duration behind the shock. The density field was derived using the methods described in Section 2.6.1. Initial analysis of the temperature profiles was done using data from firing shot-shell primers. Results from temperature analysis are applied to testing of shot shell primers, NONEL shock tube, and Detasheet.

#### 5.1 Temperature Calculations from Optical Measurements

##### 5.1.1 Shot Shell Primers

Initial analysis utilized primers in order to establish general shock propagation trends and analysis techniques within a laboratory setting. As seen in Figures 5.1 and 5.2, there is a great deal of light flare and fragmentation following the detonation of shotshell primers. The fragmentation is both unburned explosive composition, as well as pieces of the paper used to hold the pellet within the primer. The light interferes with data collection as it distorts the uniformity of the background. The fragments present can create oblique shocks both before and after the spherical shock, preventing accurate reconstruction using the Abel deconvolution technique, as this technique assumes a uniform spherical shock [26]. Figure 5.3 shows the shock Mach number from the detonation of the primers. The shock decays to a near constant speed after  $0.17m$  from the primer face. While testing the Abel deconvolution technique on a variety of shock Mach numbers is preferable, accurate deconvolution requires that the shock be relatively free of interference from oblique shocks coming off of high-velocity fragments. Additionally, the shock must be clearly separated from detonation gases. An ideal situation has the entire shock completely exit the field of view prior to the detonation gases entering the field-of-view. This will allow the pressure profile to be reconstructed by stitching together data from sequential images. If the detonation gases follow the shock too closely, only a small portion of the shock could be used to reconstruct the pressure profile.

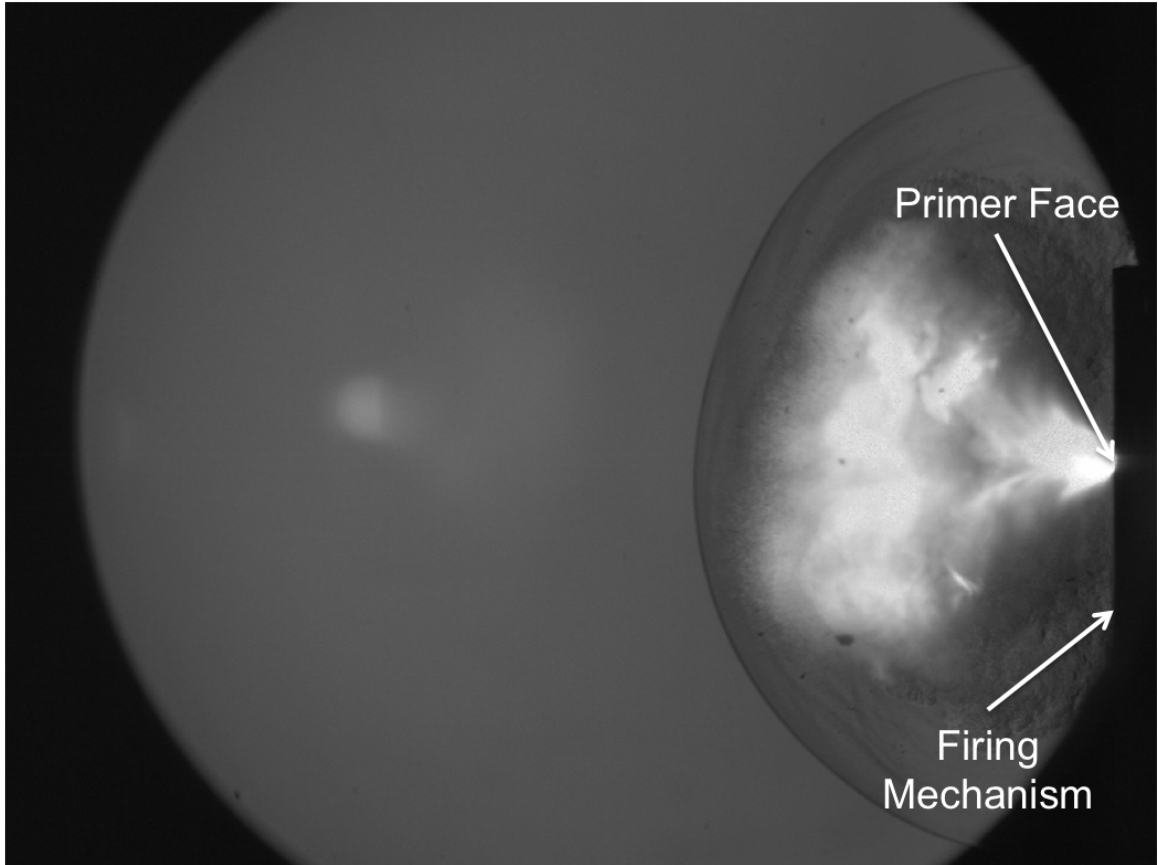


Figure 5.1: Detonation of shotshell primer. Distance across field-of-view (light gray circle) in lens is  $0.1524m$ .

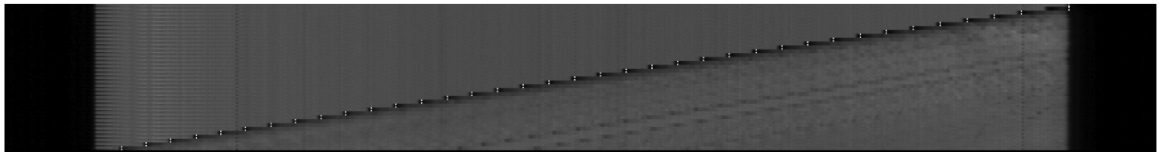


Figure 5.2: Oblique shocks forming from fragmentation before shock.

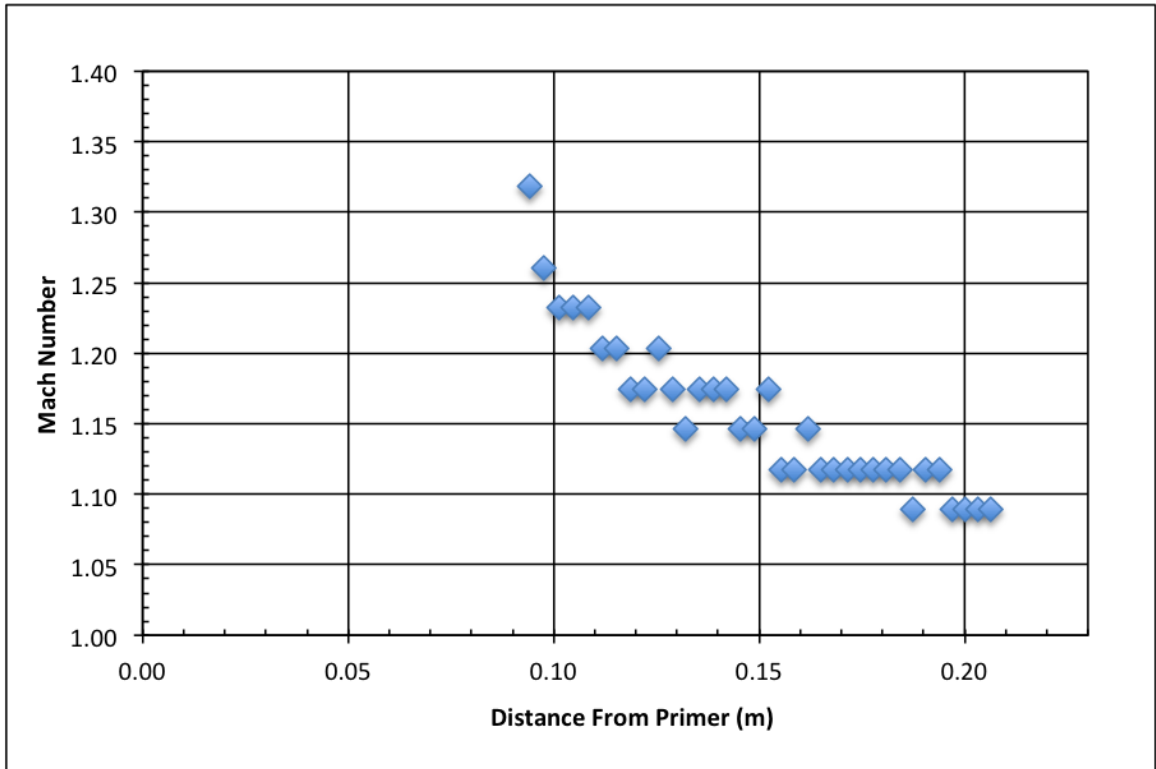
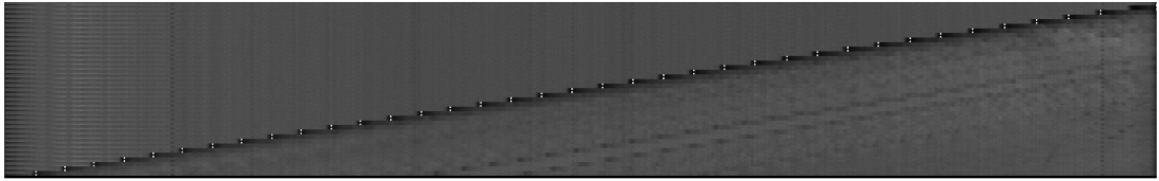


Figure 5.3: Shock Mach number from the detonation of shot shell primer.

Despite these difficulties, it is possible to image the shock coming off of the detonation of shotshell primers. In order to circumvent the interference caused by fragmentation around the spherical shock, the primer was fired at roughly a 45 degree angle outside the field-of-view. This allowed for the majority of the fragments to pass over the pressure plate in such a manner as to not interfere with the spherical shock passing over the gage. As can be seen in Figure 5.1, angles of 45 degrees or higher from the center axis of the primer face will allow a cleaner shock image to be visualized. Figure 5.4 shows a streak image produced from one of these angled shots. The primary shock is clearly delineated, along with several additional shocks, and the detonation gases have not begun to enter the field-of-view. The benefit of separation between the shock and detonation gases can also be seen in Figure 5.5, where there is no evidence of detonation gases. This method was the most successful at obtaining data from the shot shell primers and is used to test the accuracy of the Abel deconvolution technique. During testing, the primers were kept at a set distance of  $0.1651m$ , which was determined to give optimal distance between the shock and the following detonation gases.



(a) Streak Image



(b) Shock at Gage Location

Figure 5.4: Streak image and single image of shot shell primer fired at a 45 degree angle. Vertical time step in streak image is  $8.33\mu s$ , distance across field of view (gray background) is  $0.0254m$ .

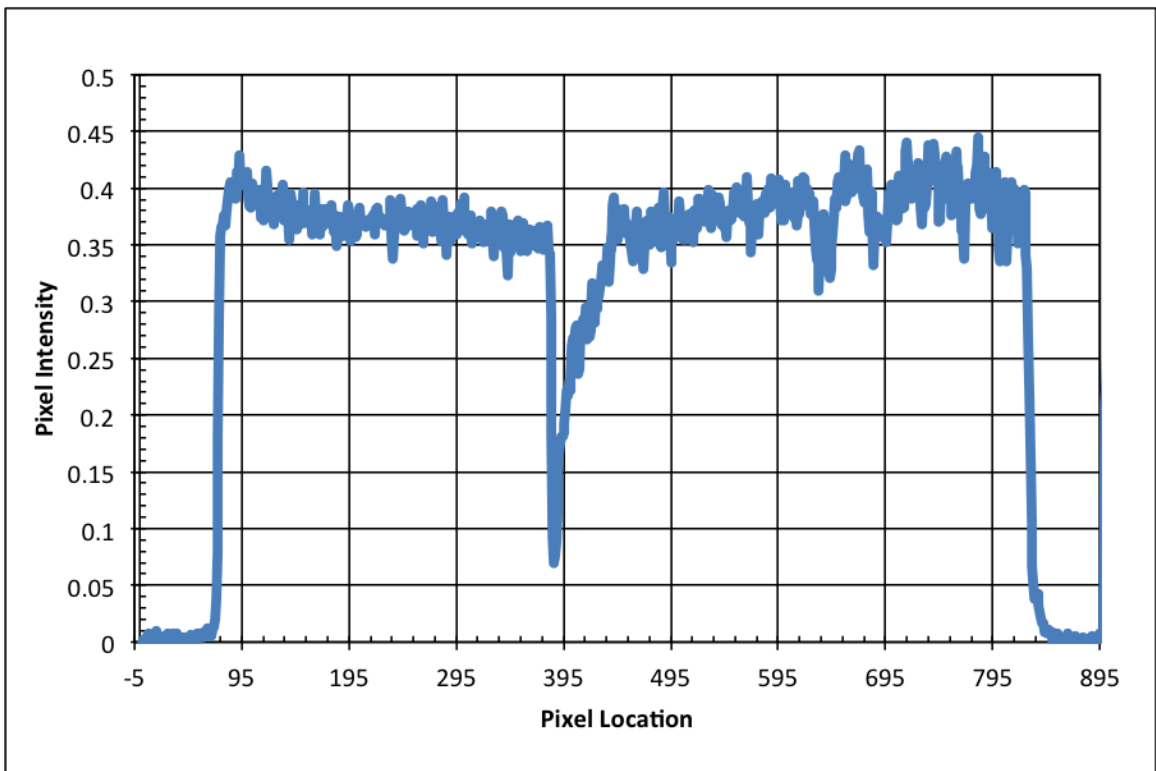


Figure 5.5: Pixel intensity across shock front.

In addition to testing the accuracy of the Abel deconvolution technique, one of the primary goals of this analysis is to test previous assumptions that the

temperature can be assumed constant behind the shock. As seen in Section 4, the relative rate of decay of temperature and pressure becomes roughly equivalent as distance from the charge increases. At distances where the shock is cleanly separated from the detonation gases, it is no longer feasible to assume that the temperature profile is constant. Additionally, while CTH is useful as a comparative tool, it is also beneficial to develop temperature profiles based on experimental data. Comparing different explosives can lead to erroneous conclusions, particularly in situations where a highly idealized scenario of the detonation of PETN is compared to the highly non ideal detonation/deflagration of shot shell primers. Developing a temperature profile based on observed experimental shock behavior will yield more accurate results.

Three different methods for reproducing the temperature, and subsequently pressure, field from the detonation of primers are considered. The first method is the constant temperature assumption and uses a temperature calculated from the Mach number of the shock wave and compressible flow relations (Equations 1.1 and 1.2). The second method is the CTH idealized temperature profile. The last method uses the ideal gas law and calculates temperature directly from the piezoelectric pressure signal and the optical density field. For the gage's pressure data, only the signal corresponding to the peak pressure and pressure duration are considered; the atmospheric signal and the noise after the shock are neglected. Figures 5.6 and 5.7 show the respective portions of the experimental pressure and density fields under consideration. A second-order polynomial fit is applied to the highlighted sections of the pressure and density profiles to account for oscillation and is used in the subsequent analysis.

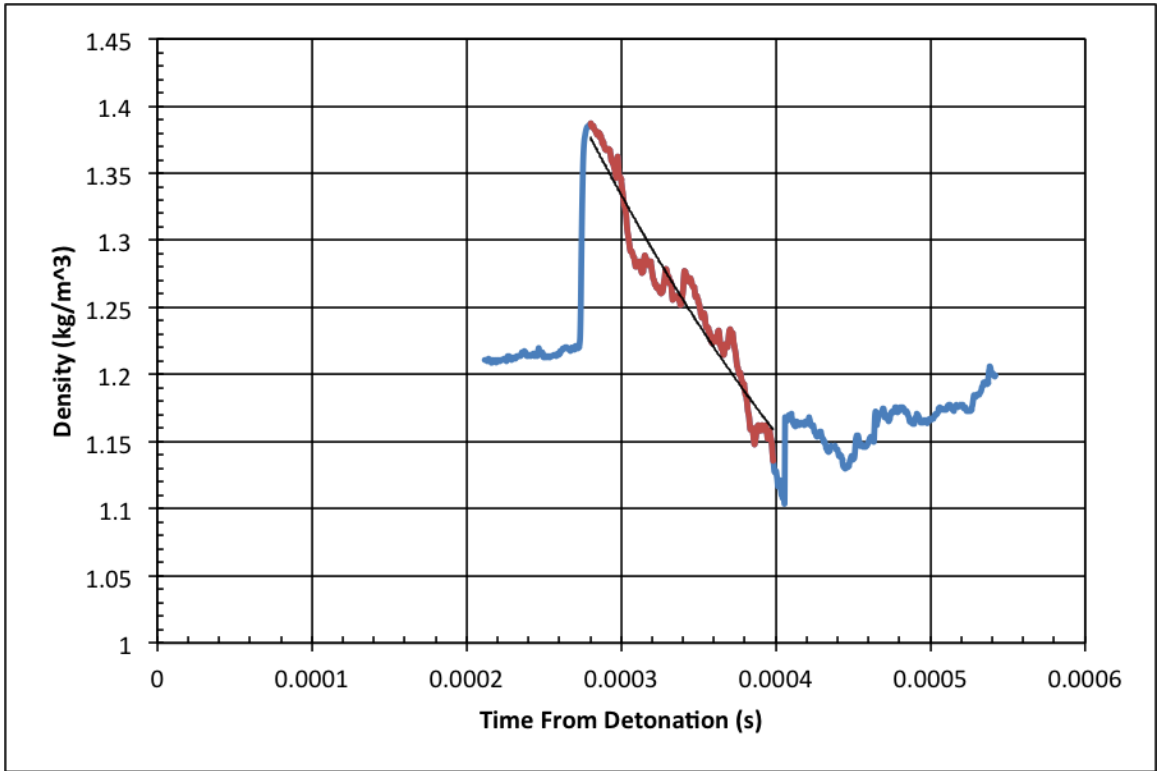


Figure 5.6: Gage pressure profile. Highlighted portion (red) used to determine temperature. Distance from primer face to gage is  $0.165m$ .

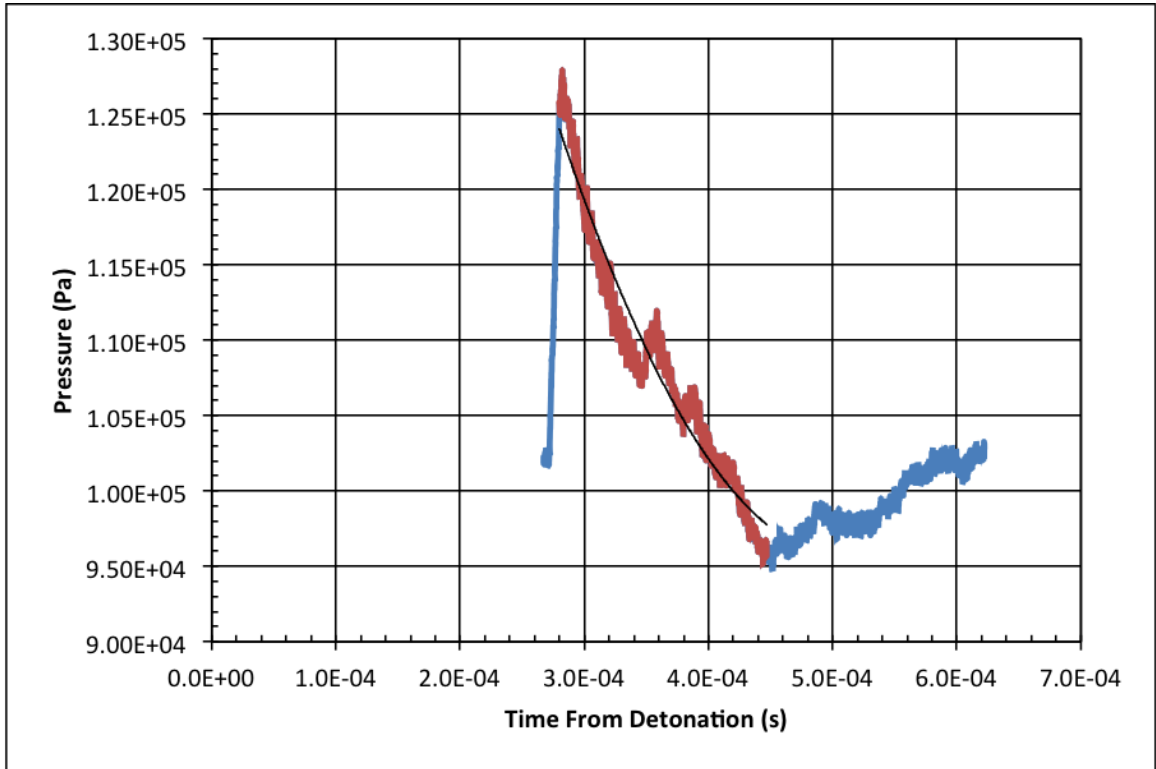


Figure 5.7: Optical density profile created using Abel deconvolution. Highlighted portion (red) used to determine temperature.

The compiled temperature profiles derived from the constant temperature assumption, the CTH analysis, and the direct temperature calculation from experimental data are shown below in Figure 5.8.

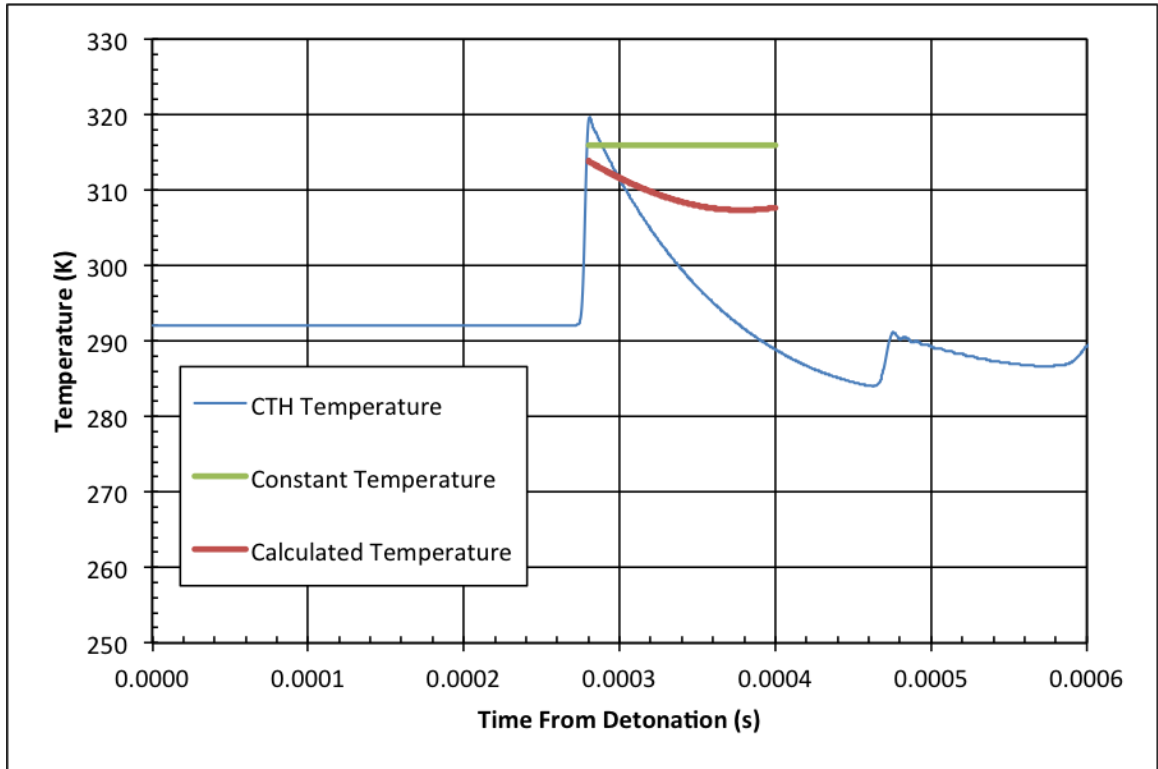


Figure 5.8: Compilation of temperature profiles from detonation of shot shell primers.

Figure 5.8 shows a clear decay in the temperature profile for the calculated temperature scenario. The constant temperature profile is not appropriate for resolving the complete pressure field. Agreement between the calculated and CTH temperature profiles is also good, though the calculated profile shows a decay that does not drop below atmospheric temperature to the extent that the CTH profile shows. The CTH profile is highly idealized and uses PETN, as opposed to the explosive mixture in the primers. Additionally, the primer mixture is confined in a metal cup, whereas the PETN is detonated in air, which may also be a source of the differing behaviors. The confinement is designed to send most of the energy forward from the primer face, whereas the shock was analyzed at an angle away from the primer face. This confinement led to a slightly non-spherical shock, but as all testing with the primers was relatively far away from the face, the analyzed shock can be assumed spherical. These differences in the compound and methods used to calculate the profile could be the cause of the discrepancy between the primer and PETN data. Compared to the calculated temperature profile, CTH would be a poor model for resolving the entire pressure profile. In situations where gage data is not available, a more accurate method of generating a temperature profile would be to use the CTH profile to generate a linear temperature profile as seen in Figure 5.9. As the experimental data does not show a significant negative pulse as is seen in the CTH profile, once the experimental data has decayed to atmospheric levels, constant atmospheric

temperature should be used to determine the rest of the pressure profile. A similar method can be used with the experimental data, creating a linear temperature profile from the density data. The locations of peak and atmospheric density (highlighted in Figure 5.10), are used to create a linear fit. The theoretical peak and atmospheric temperatures are assigned to these locations. For data past the atmospheric point, the air temperature is assumed atmospheric, as the negative pulse is not expected to greatly reduce the temperature below atmospheric behind the shock. The CTH analysis shows that pressure, density, and temperature decay at approximately the same rate, allowing for the density decay profile to be used to generate the linear temperature profile. A comparison of these two linear profiles is shown below in Figure 5.11, indicating fairly good agreement between the linear approximations, although the CTH approximation both predicts a higher peak temperature and shows a slightly faster rate of decay. The effect on the pressure profiles is shown in the Section 5.2.

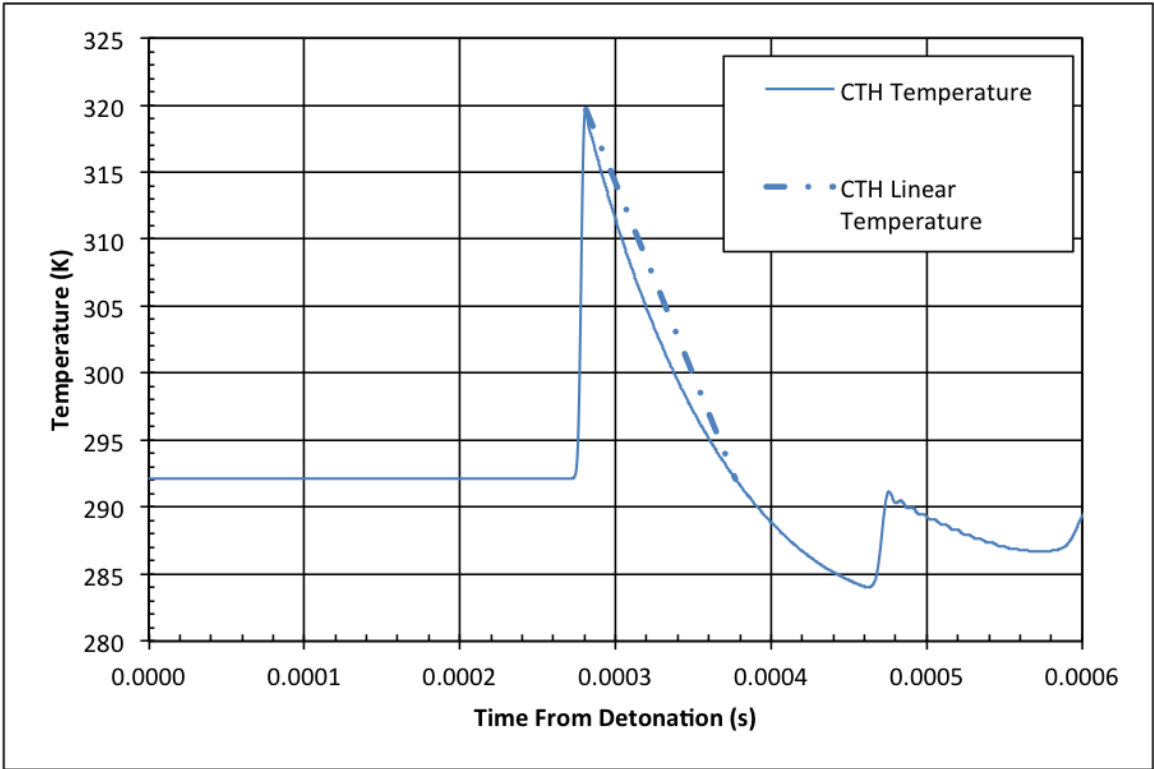


Figure 5.9: Linear approximation (red) of CTH temperature profile.

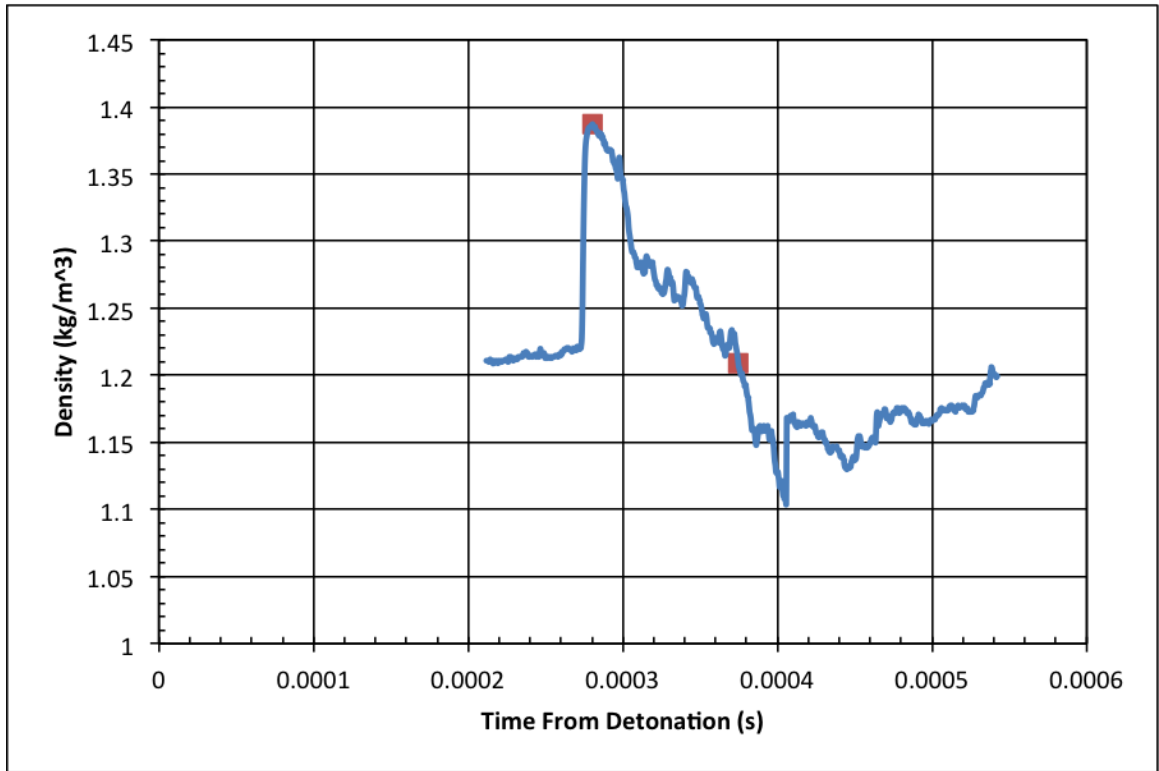


Figure 5.10: Peak and atmospheric points used to create linear temperature fit from density profile.

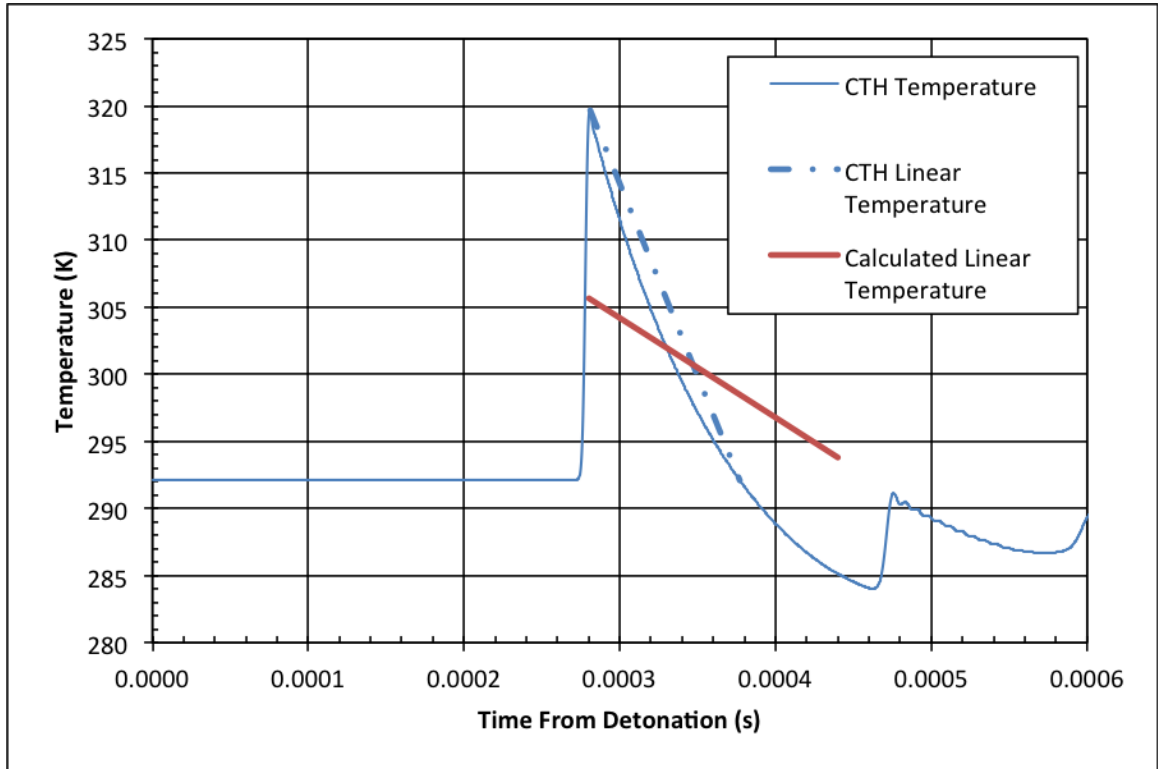


Figure 5.11: Comparison of linear approximations of temperature profile.

### 5.1.2 NONEL Shock Tube

The analysis of the shock waves from the detonation of NONEL shock tube is the same analysis performed for the detonation of primers. The major advantage of using NONEL shock tube is the lack of fragments produced during detonation, resulting in an unimpeded spherical shock traveling through the field-of-view. While there are additional shocks following the primary shock, the overall profile behind the shock is very clean, allowing for testing at several distances. These secondary shocks may be due to the NONEL tubing flexing during detonation, though efforts were made to secure the end of the shock tube. The shock did reflect off of the apparatus used to hold the NONEL during testing, but the reflected shock was weak and was occluded by the detonation gases during firing, so its presence did not interfere with the data taken across the primary and secondary shocks. A slight disadvantage to using NONEL is the relative weakness of the shock. The NONEL shock wave decays faster, resulting in weaker shocks at distances similar to primers. The shock decays to a constant around  $0.08m$  from the end of the tube. Figure 5.12 shows a typical detonation of NONEL shock tube. To achieve comparable Mach numbers, data must be collected closer to the shock tube's opening, which may not provide sufficient time for the shock wave to fully separate from the detonation gases. A plot of the shock Mach number for the detonation of NONEL is shown below in Figure 5.13.

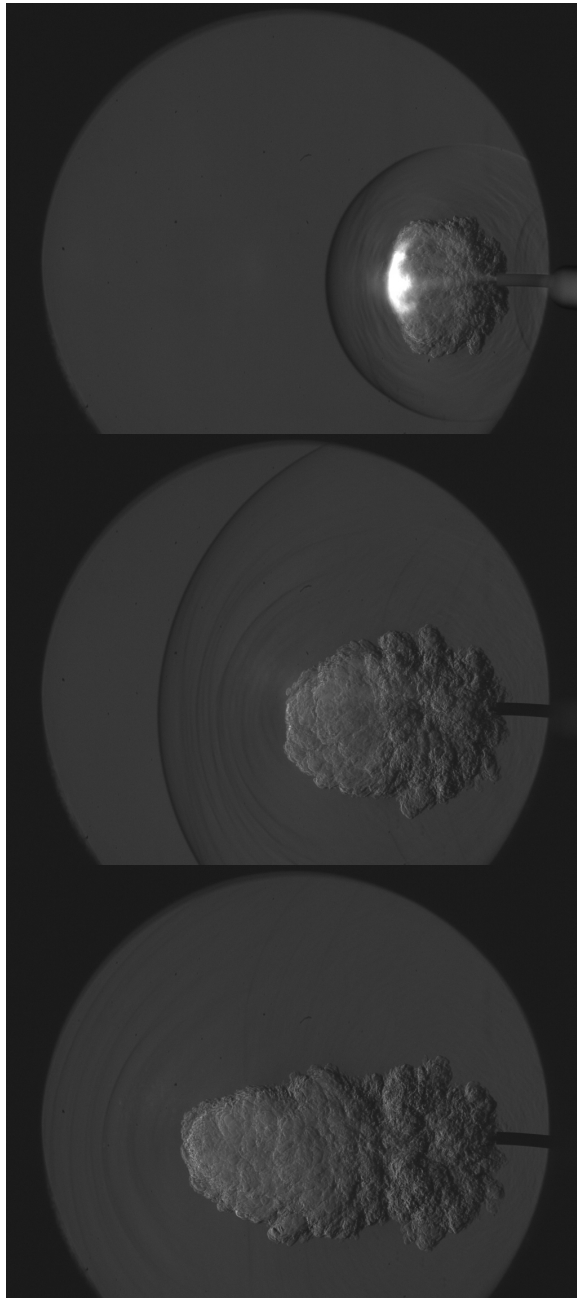


Figure 5.12: Detonation of NONEL shock tube. Distance across field-of-view is  $0.1524m$ . First image at  $t=104.86\mu s$  from shock exiting NONEL tube, time between sequential images  $104.8\mu s$ .

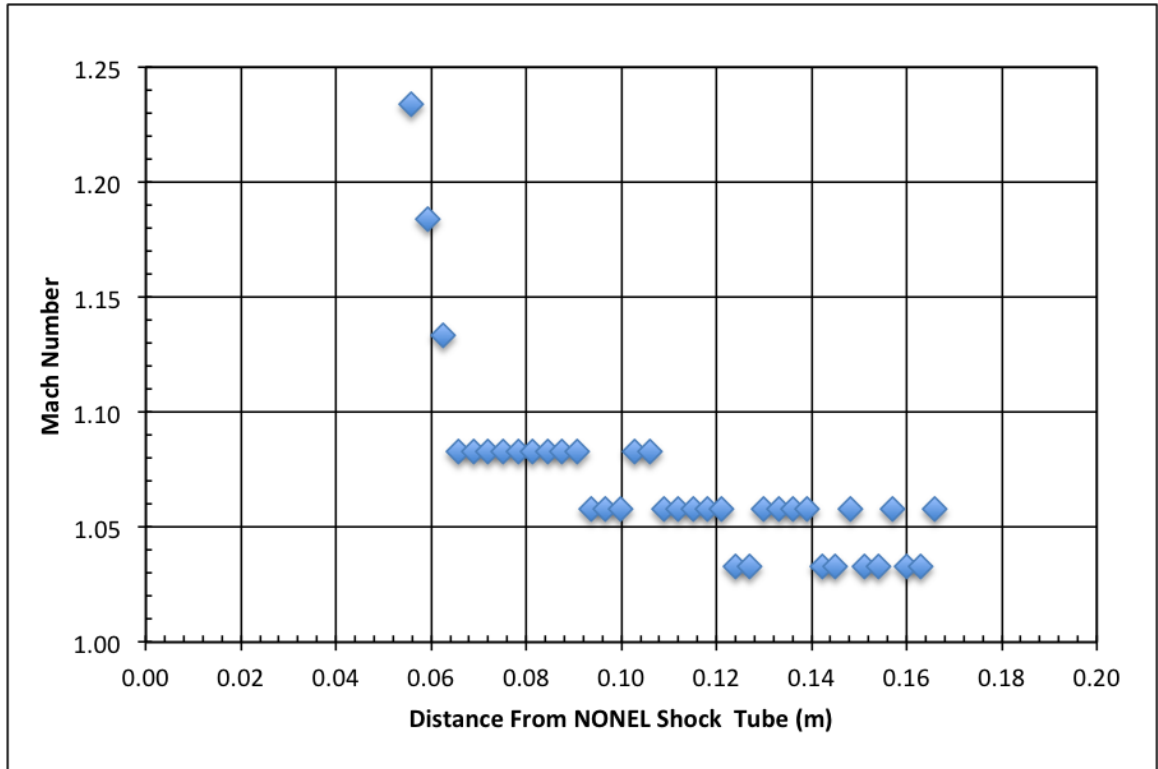
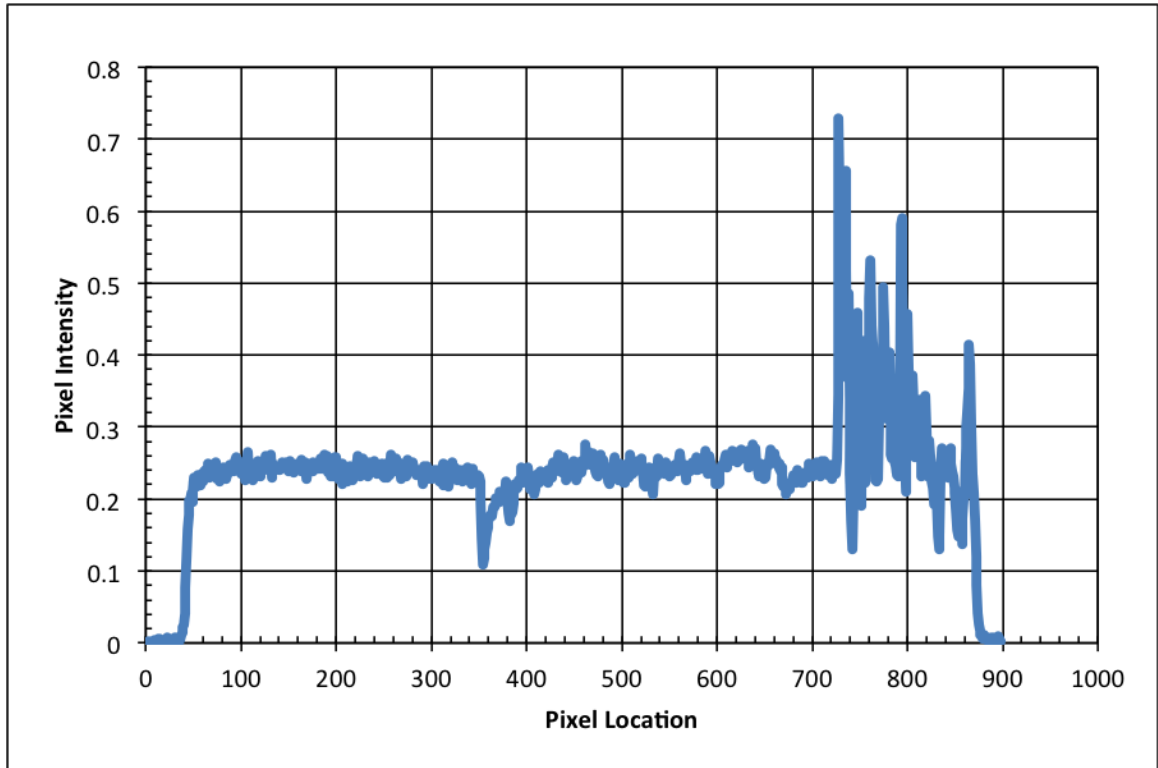


Figure 5.13: Mach number of shock generated by detonation of NONEL shock tube. Mach number past 0.3m remains constant at 1.03.

A row of pixels directly above the aluminum plate holding the gage is selected from the image in Figure 5.14a. In this figure, the leading edge of the shock is located immediately above the face of the gage. The intensity of the row of pixels is shown in Figure 5.14b, which clearly highlights the location of the atmospheric conditions preceding the shock, the shock decay profile, and the following detonation gases. The Abel deconvolution is not performed on points in front of the shock. While the process can reproduce the atmospheric intensity somewhat, the variability in initial pixel intensity leads to an unphysical wide range of atmospheric intensities, so this section is ignored. Therefore, all future shock data calculated using the Abel deconvolution technique will not consider atmospheric conditions preceding the shock.



(a) Shock Image



(b) Pixel Intensity

Figure 5.14: Example of pixel intensities across shock from NONEL shock tube. Distance from NONEL to gage is  $0.127m$ .

Detonation of NONEL shock tube is non ideal because of the shape of the HMX/Al explosive mixture inside the tube that contributes to the formation of the shock, so comparison to CTH is impossible. It is possible to directly calculate the temperature as was done with the primers. The pressure and optical signals used are shown in Figures 5.15 and 5.16. The results are shown in Figure 5.17. An important feature is the peak at the front of the shock. This peak is highly unphysical and is attributed to noise in both the gage and optical data. The immediate rise and fall is unusual, and the theoretical peak temperature is  $299K$  based on the shock Mach number. This theoretical peak falls in line with the calculated temperature profile at  $t=0.0089s$ . After this point, the temperature profile remains centered slightly below atmospheric temperature, with the observed increase in temperature at  $t=0.00402s$  attributed to a following secondary shock.

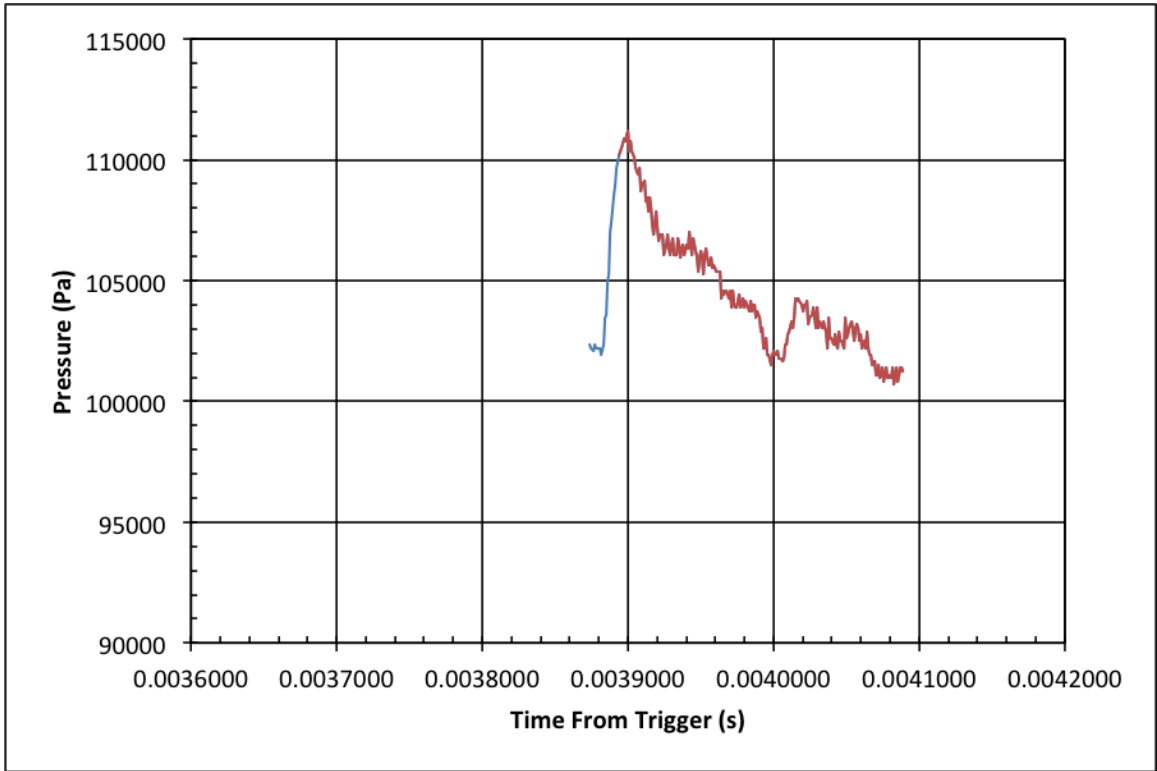


Figure 5.15: Gage pressure profile. Highlighted portion red used to determine temperature. Distance from NONEL to gage is  $0.127m$ .

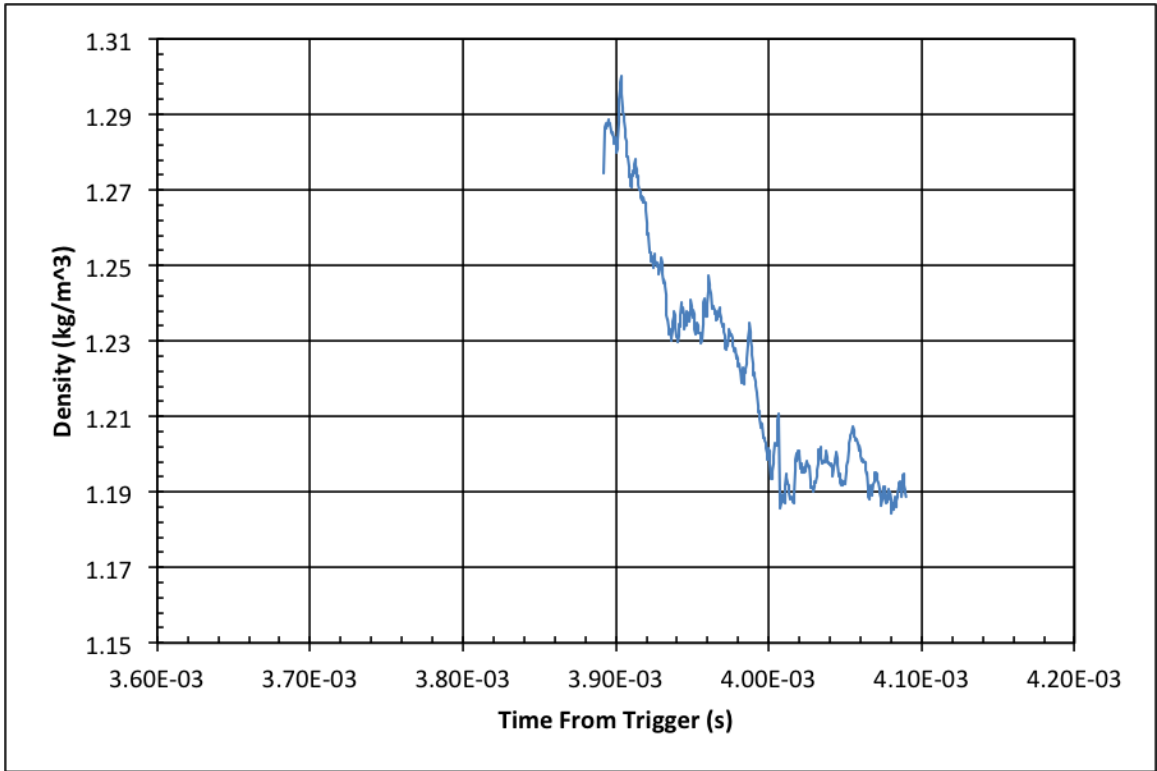


Figure 5.16: Optical density profile. Entire signal used to determine temperature. Distance from NONEL to gage is 0.127m.

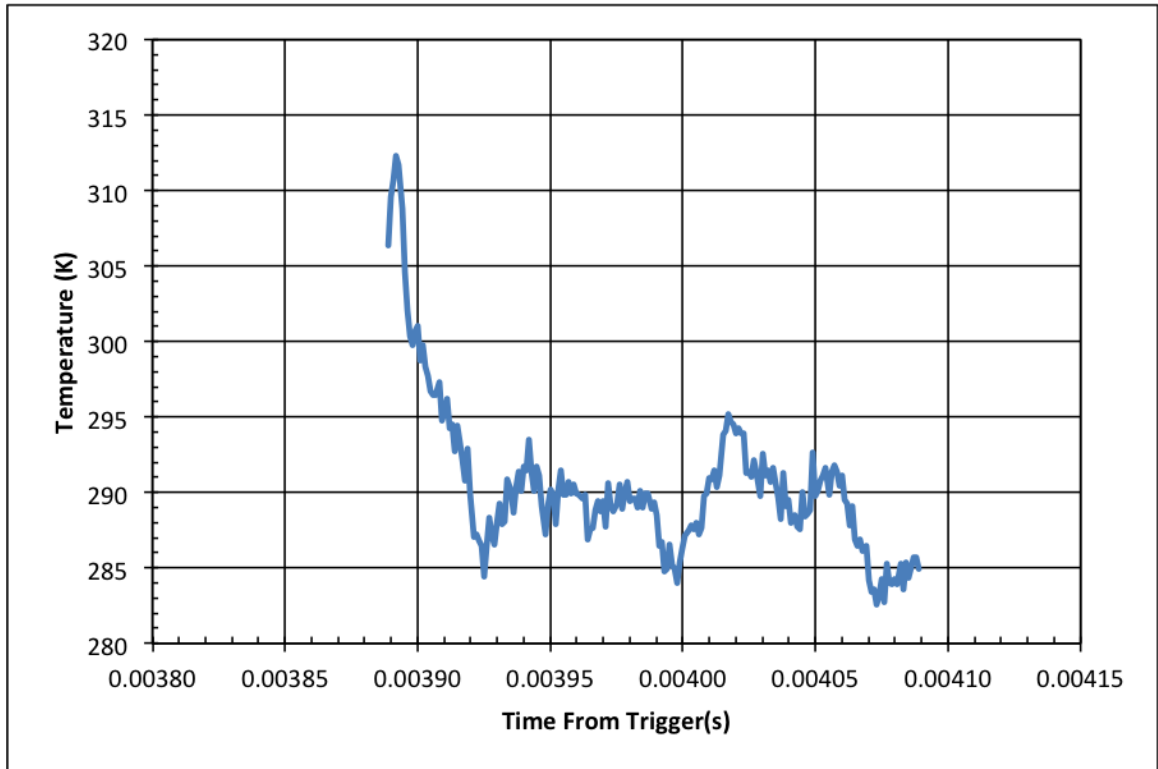


Figure 5.17: Temperature profile directly calculated from optical density and gage pressure. Mach 1.03.

The existence of this secondary shock is seen in all tests using the NONEL shock tube, and its existence makes it difficult to attribute a single linear temperature profile to the data. Additionally, there is no CTH profile to compare to the calculated temperature profile. To calculate a linear temperature profile, the fact that the relative rates of temperature, density, and pressure decay are equivalent is used to generate a linear profile. Using the density profile, the time locations of the peak and atmospheric density after the secondary shock are chosen (see Figure 5.18). A linear fit is created from these two points using the theoretical peak temperature and the atmospheric temperature and compared to the calculated temperature profile in Figure 5.19.

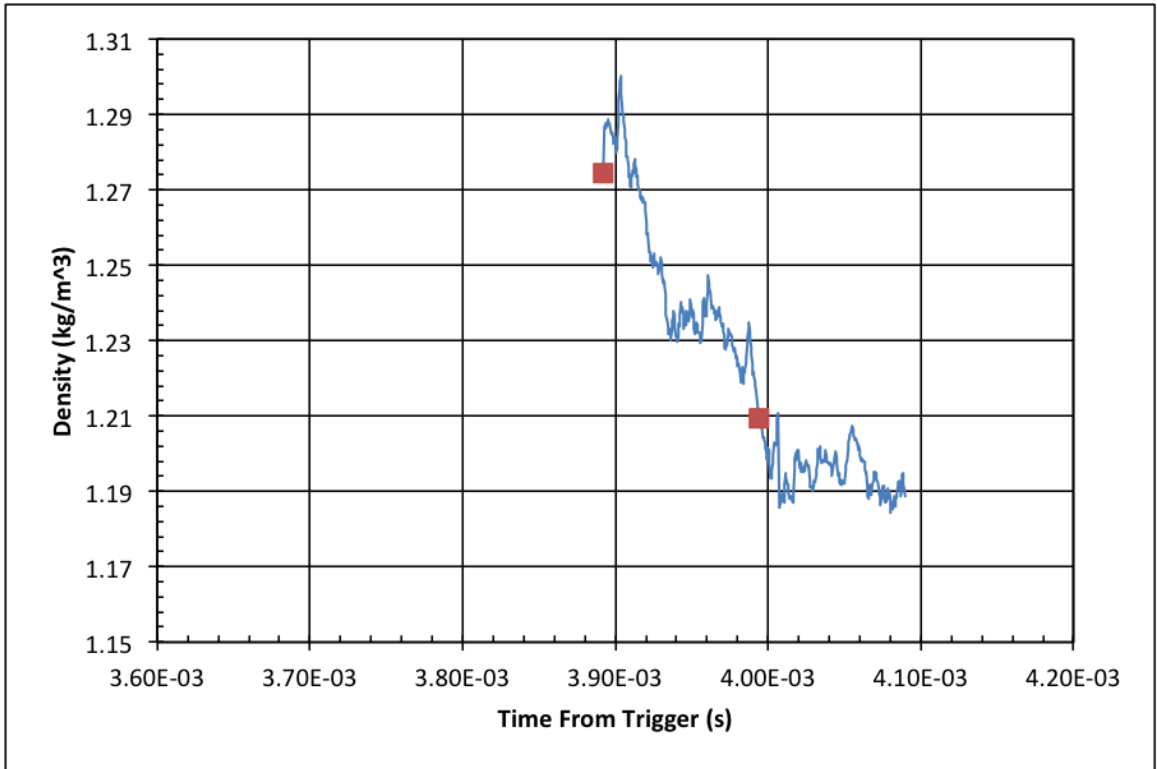


Figure 5.18: Time of peak and low points highlighted.

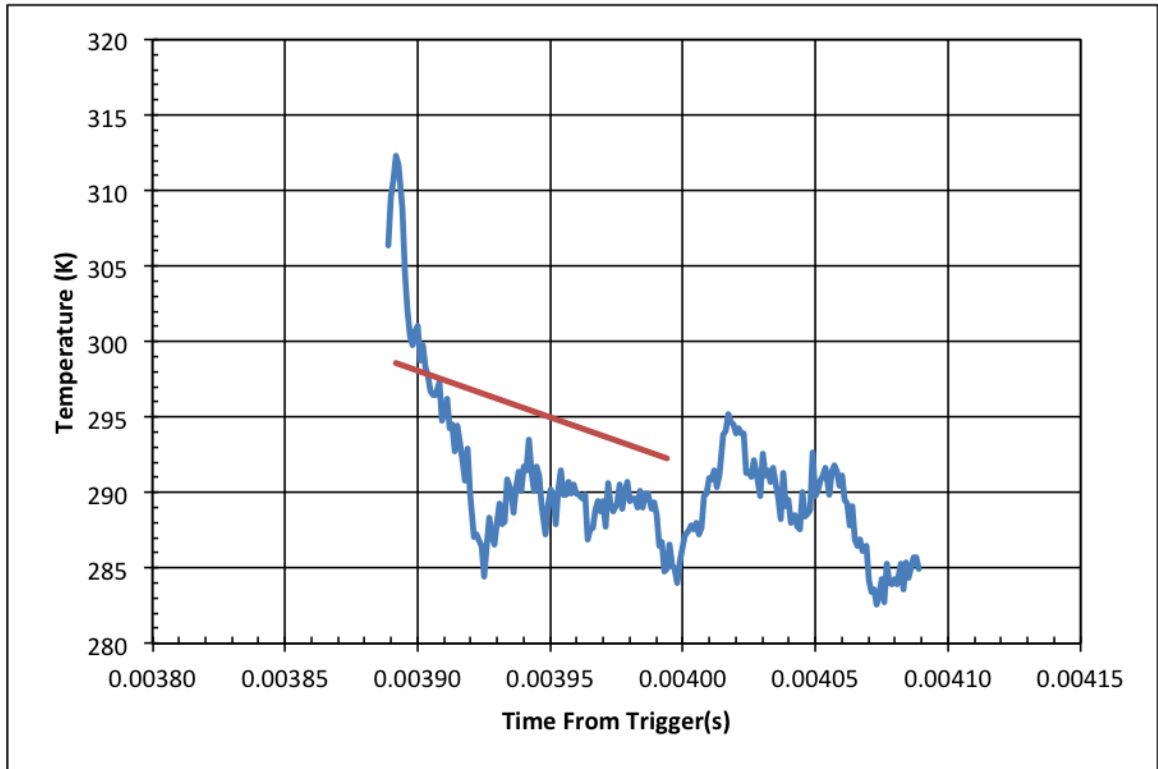
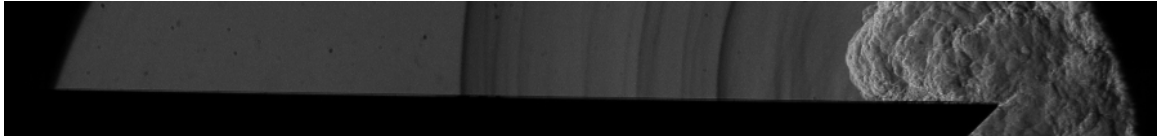
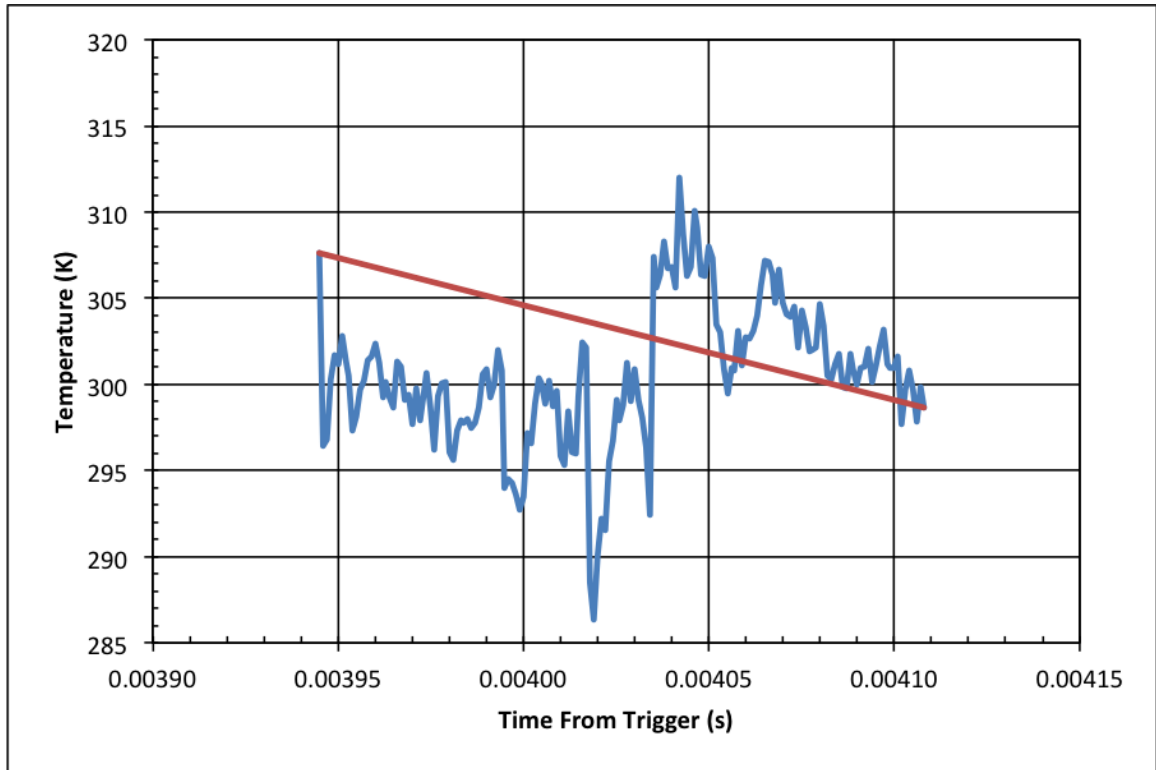


Figure 5.19: Linear fit of experimental temperature profile.

The temperature field for one additional NONEL test is shown below (Figure 5.20). The temperature field and linear decay profile are calculated using the same method described above. In this test, the shock following the primary shock is stronger than in the previous test, resulting in a greater influence on the temperature field.



(a) Shock Image



(b) Calculated Temperature

Figure 5.20: Temperature profile and linear fit directly calculated from optical density and gage pressure. Distance from NONEL to gage is  $0.102m$ . Mach 1.06.

### 5.1.3 Detasheet

The last set of explosive compounds testing were 1g rolled balls of Detasheet, consisting of 80% PETN. Again, the same analysis done to the primers and NONEL shock tube is done here. In this series, all testing was done in the field, so the setup used with the schlieren system is slightly different. Additionally, during testing the background intensity shutting, requiring a correction to the intensity be applied. This is described in further detail in Section 5.2.4. The major differences are the use of an arc lamp in place of a single-die LED, and the presence of the calibration lens within the field-of-view during all detonations. The presence of the calibration lens is unfortunate as the shock impinged on its surface causing a backwards reflection into the oncoming shock. This occurrence

prevented the analysis of the complete pressure profile as done with primers and NONEL. The Detasheet was fired at least  $0.45m$  outside the field-of-view, preventing collection of the entire Mach profile; the shocks were observed to be traveling at a fairly constant rate through the field-of-view. Figure 5.22 shows the shock Mach numbers from the firing of the Detasheet at two locations. A complete Mach profile could not be collected due to the limited field-of-view and the location of the charge. The limited field-of-view and the camera's frame rate also resulted in the small number of data points available. One last major difference is the focal length of the calibration lens; here it is  $4m$ , which was later discovered to give less accurate results than using the  $10m$  focal length calibration lens. However, the comparison between the gage and optical data still shows good agreement for the portion of the shock being analyzed. Figure 5.21 shows the full view of the shock impinging on the calibration lens during propagation. Also note that for this analysis, the row of pixels analyzed goes through the center of the calibration lens, not directly over the gage as has been done in the previous sections. For these tests, the gage was not in the field-of-view. This may also account for some of the discrepancy between the gage and optical measurements. The shock and corresponding pixel intensities from the detonation of Detasheet are shown in Figure 5.23. The charge is  $0.902m$  from the face of the gage.

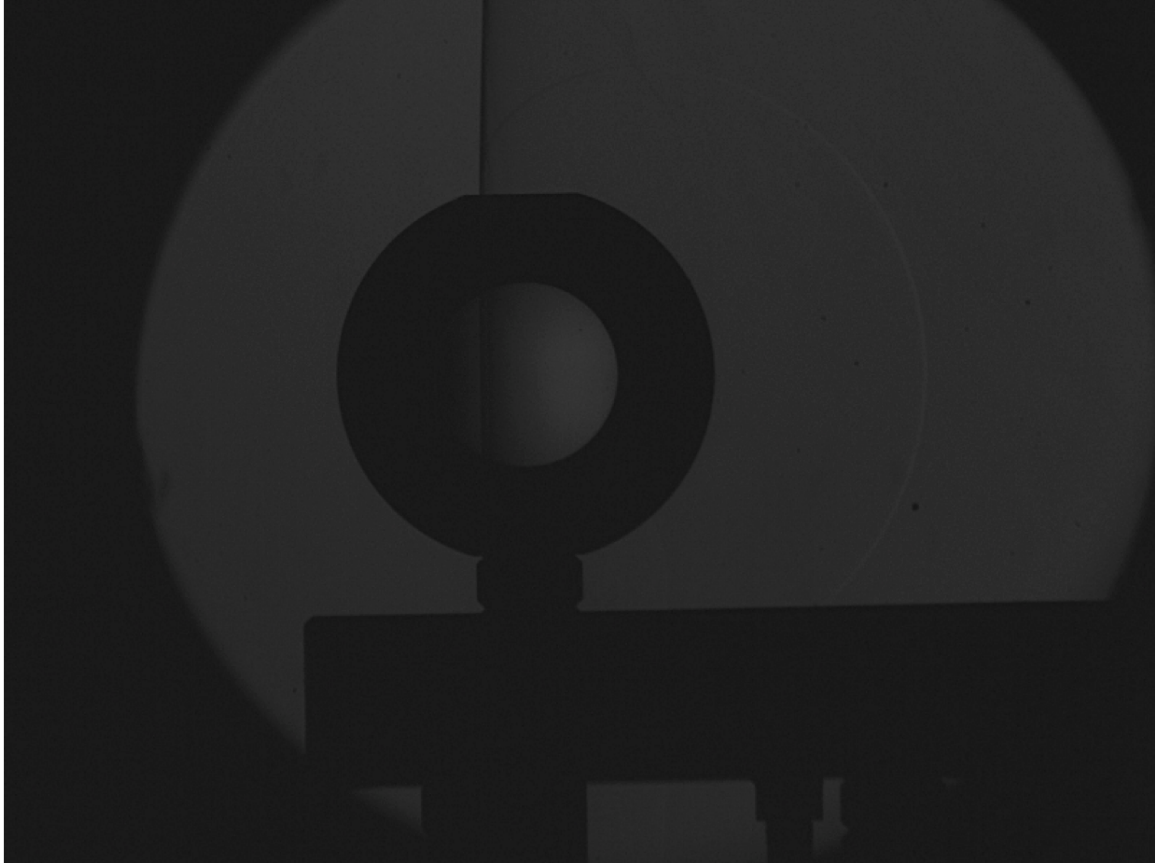


Figure 5.21: Typical shock from the detonation of Detasheet.

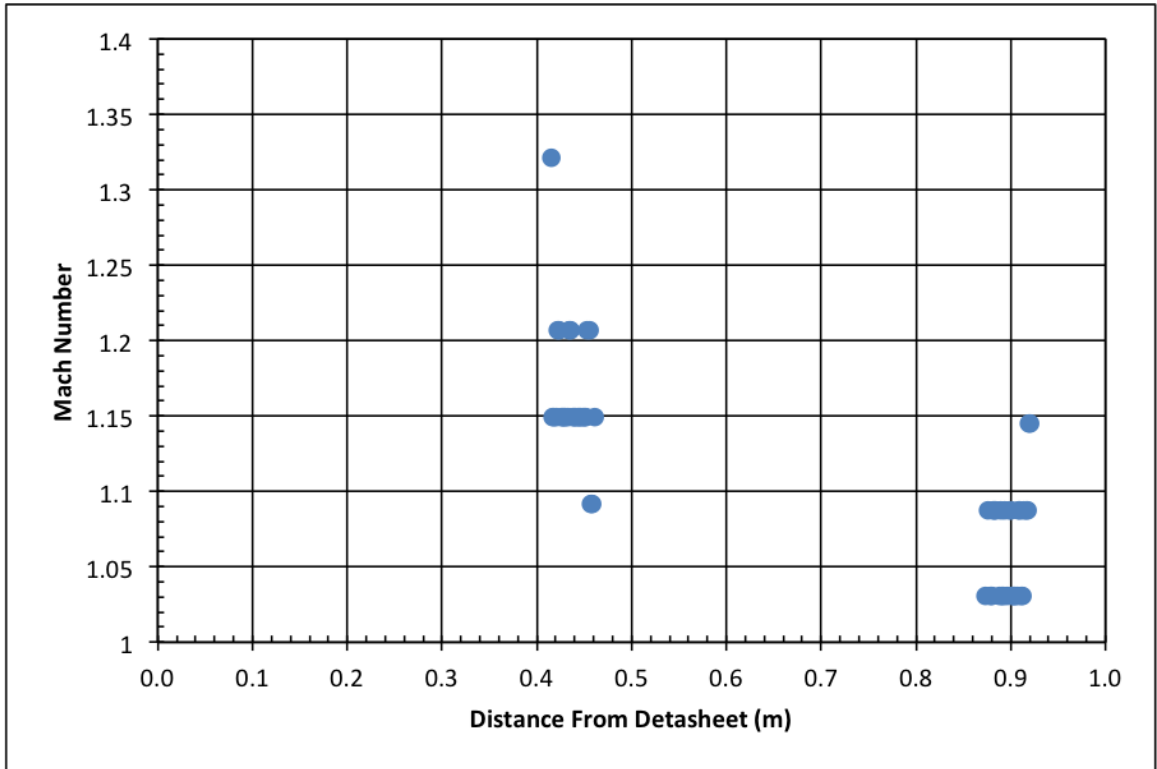
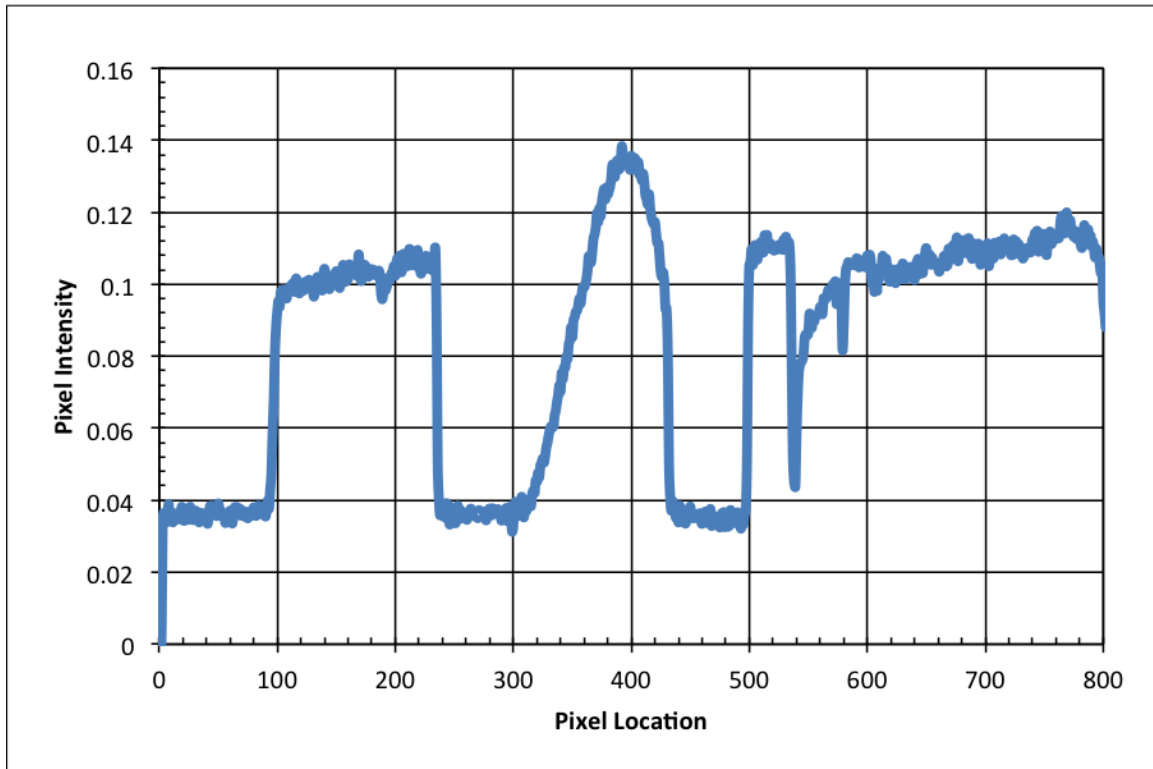


Figure 5.22: Shock Mach numbers from detonation of Detasheet.



(a) Shock Image



(b) Pixel Intensity

Figure 5.23: Example of pixel intensity across shock from detonation of Detasheet, distance from charge to gage  $0.9017m$ . Mach 1.08.

The temperature profile is recreated using sections of the gage pressure and optical density profiles (Figures 5.24 and 5.25). The optical density had a linear fit applied to the data for this calculation. The gage pressure and the density calculated by the linear fit were used to determine the temperature field. This allowed the temperature field to be expanded past the data available in the optical signal. The additional small peaks behind the leading edge of the shock are caused by additional shocks visible in Figure 5.23a. The calculated temperature profile is compared to the constant temperature profile and the CTH temperature profile in Figure 5.26. As with the primers, the temperature at the leading edge of the shock is higher than expected, most likely due to noise in either the gage or optical signals. This temperature signal also decays faster than the CTH profile would predict, indicating that the CTH profile may predict higher temperatures

with increasing distance behind the leading edge of the shock. This discrepancy can be due to noise within the system, but it may also be due to the 4m focal length used for calibration purposes. The presence of the detonator used to detonate the Detasheet may also contribute to some of the discrepancy.

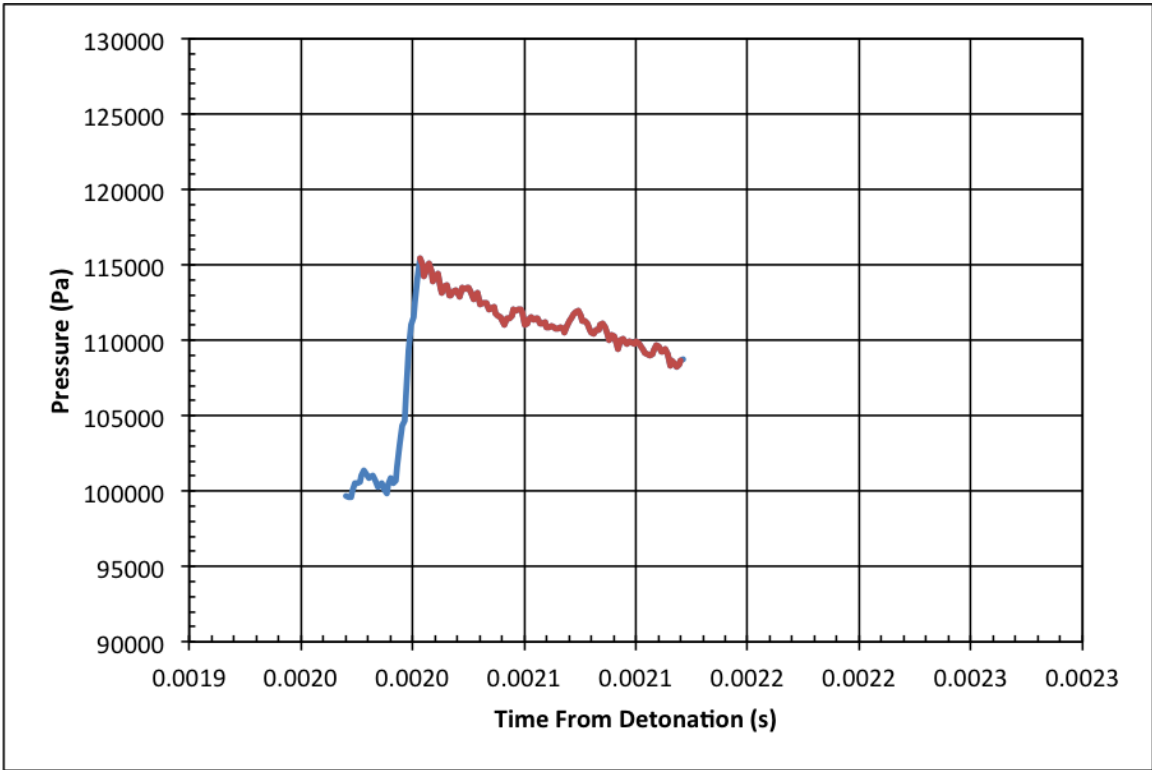


Figure 5.24: Gage pressure profile. Highlighted portion red used to determine temperature. Distance from Detasheet to gage is 0.902m.

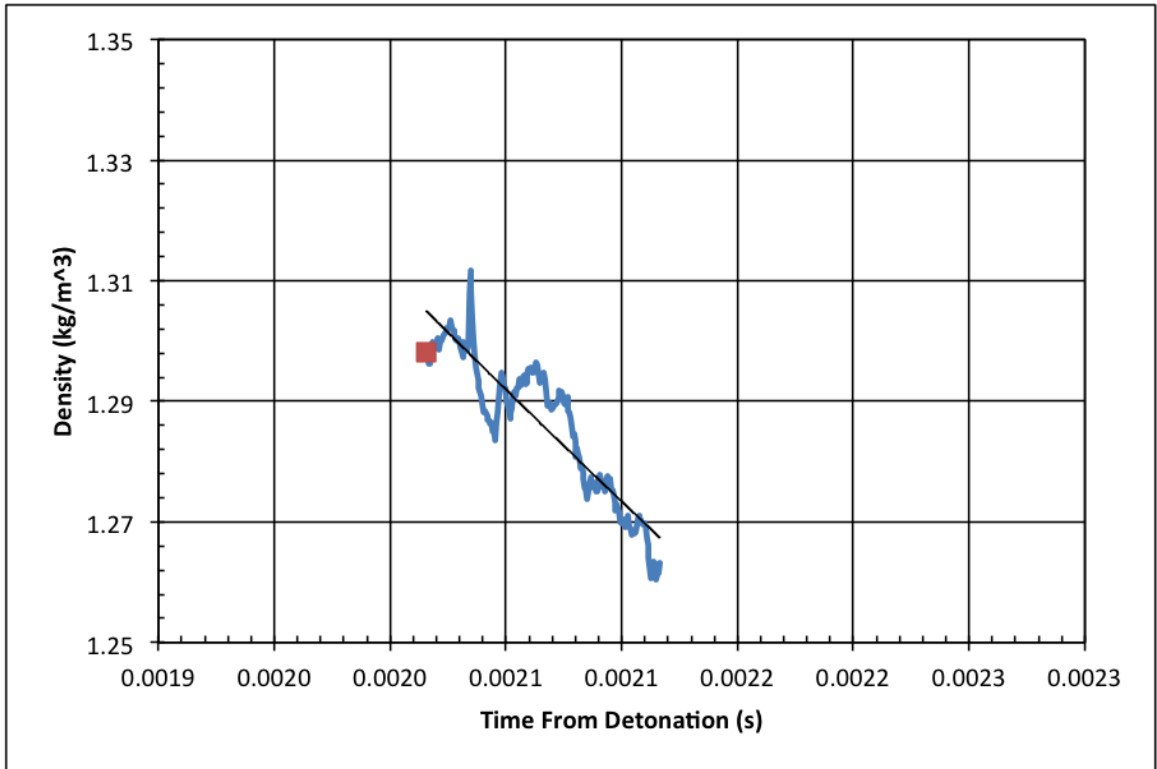


Figure 5.25: Optical density profile. Location of leading edge of shock highlighted. Linear fit of entire selection used to determine temperature.

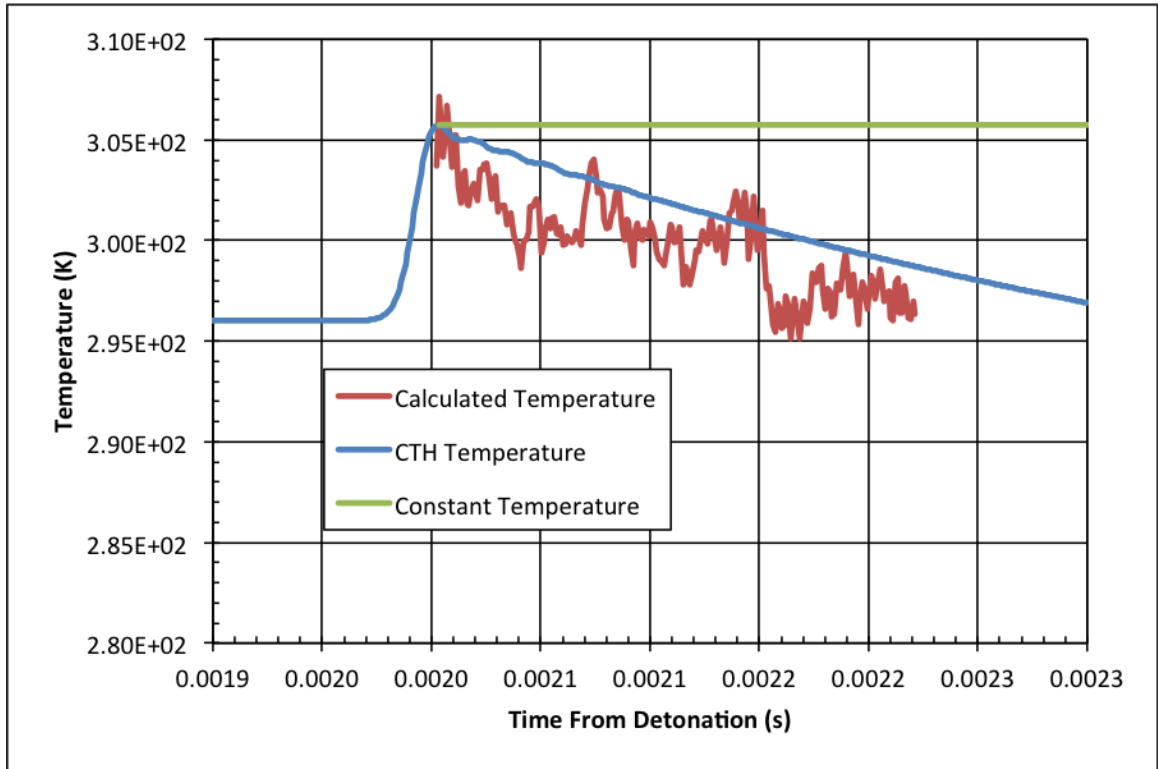


Figure 5.26: Compilation of temperature profiles from detonation of Detasheet.

For the calculated temperature, a linear fit is applied between the point at the front of the shock (highlighted in Figure 5.25) and the end of the temperature profile. Figure 5.25 shows the point at the leading edge of the shock. The linear fit and its comparison to the linear fit of the calculated temperature profile is shown in Figure 5.27. The two linear fits decay at nearly the same rate, though the linear calculated temperature fit does not reach the peak temperature at the leading edge of the shock. The effect on the pressure profiles using the CTH linear fit is shown in Section 5.2.3.

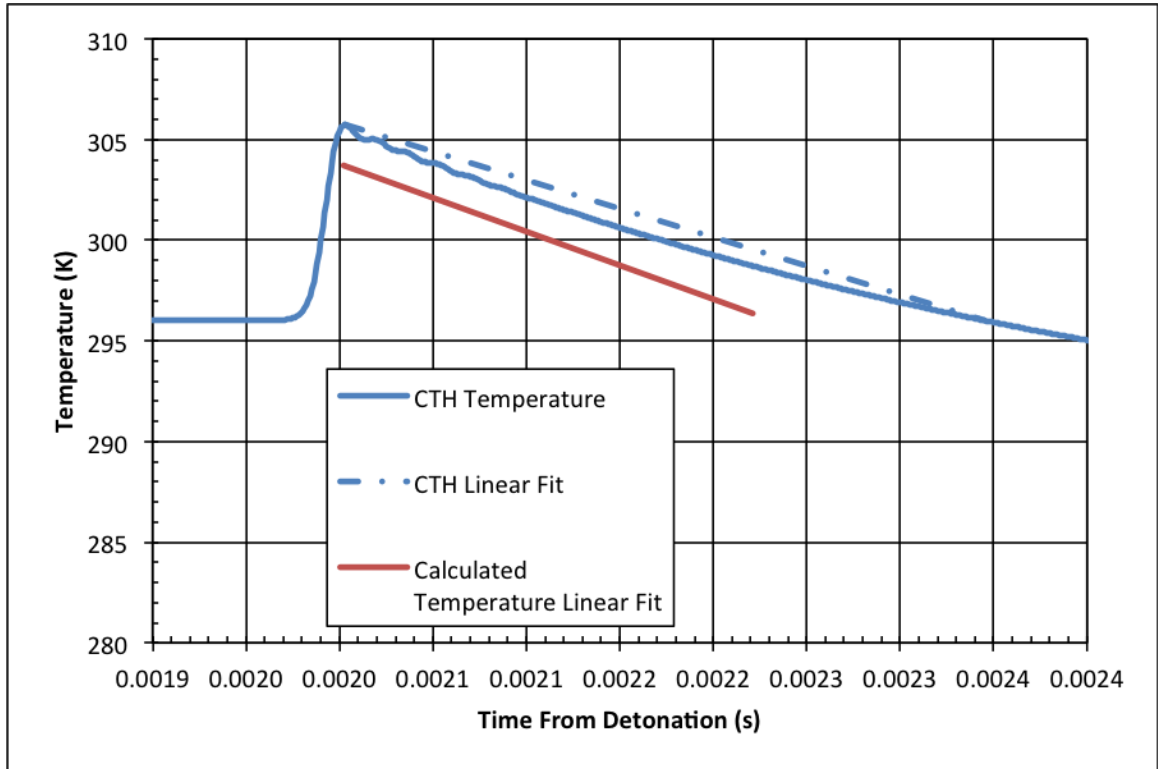
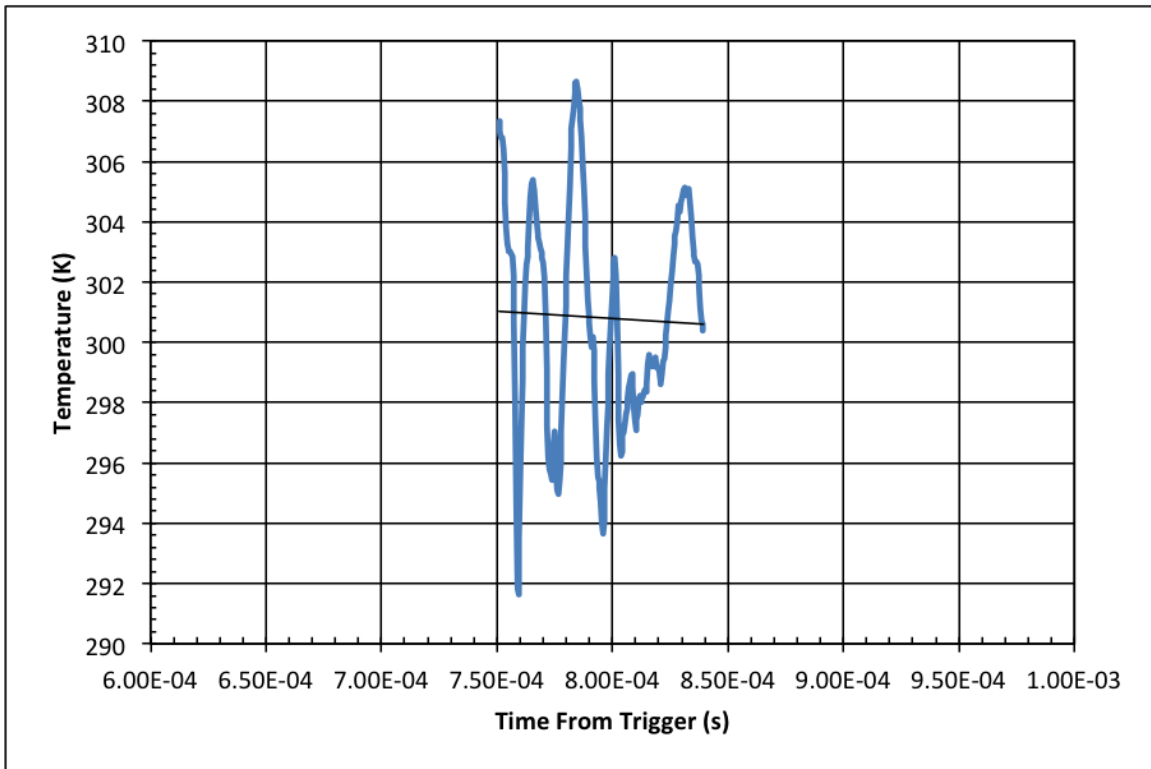


Figure 5.27: Linear fit to CTH profile and calculated temperature profile.

One additional data set was analyzed, with a distance of  $0.457m$  from the gage to the charge. In this test, the background shifted linearly, requiring a correction be applied to recreate a flat background. This correction was also applied to the shock intensity. Section 5.2.4 goes into the details of this process. After the correction, the method of determine the temperature profile is the same as described above. The only deviation from the above process is that the gage profile had a second-order polynomial fit applied to it, similar to the process in Section 5.1.1. This fit and the optical density data were used to generate the temperature profile and linear fit below (Figure 5.28). The oscillation in the temperature profile is due to oscillation in the density profile, which comes from the presence of fragments within the field-of-view.



(a) Shock Image



(b) Temperature Profile

Figure 5.28: Linear fit to temperature profile. Distance from gage to charge is  $0.456m$ .

## 5.2 Pressure Calculations from Optical Measurements

The analysis in Section 5.1.1 shows that while using a CTH temperature profile is reasonably comparable to an experimental temperature profile, though the rate of decay is faster with increasing distance from the leading edge of the shock. In order to determine the pressure field, all three of the temperature profiles will be analyzed for accuracy using the primer data as a benchmark.

### 5.2.1 Shot Shell Primers

Figure 5.29 shows the comparison of the different temperature profiles used to calculate the pressure field behind the shock. Constant temperature, the complete CTH profile, and the linear calculated temperature profile are compared

to the gage pressure. The CTH profile is included as a comparison to an idealized detonation, but clearly shows very poor agreement between the other profiles and the gage data. It neither resolves the experimental peak pressure, and it predicts a larger negative pulse than is backed up experimentally. Therefore, care should be taken if the CTH profile is to be used to generate temperature or pressure decay trends for experimental data.. The good agreement between the gage and linear profile throughout indicates that using an experimentally derived temperature decay field provides the best reproduction of the pressure field behind the shock. Additionally, using a constant temperature profile clearly shows very poor agreement with the gage pressure and the linear temperature pressure profile. Therefore, using a constant temperature profile is a poor choice and all other work will exclude analysis of the constant temperature profile.

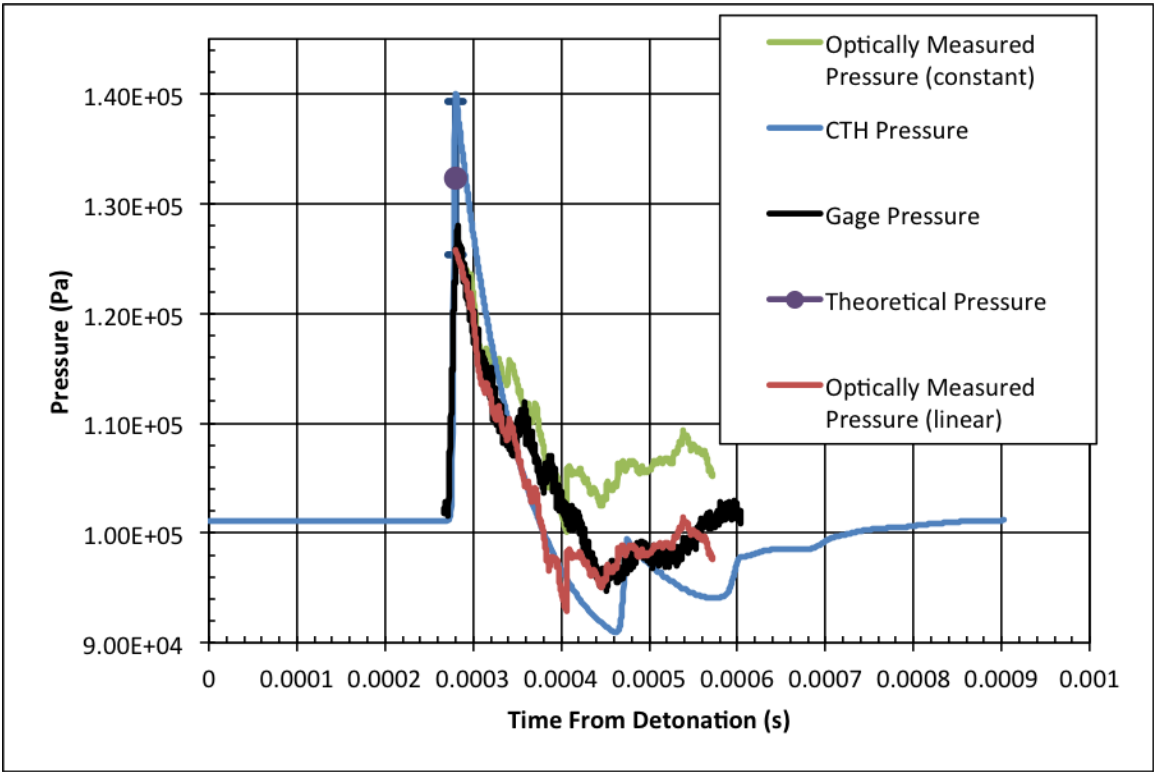


Figure 5.29: Compilation of pressure profiles used with shot shell primers. Mach 1.12, theoretical pressure  $185kPa \pm 7kPa$ .

An analysis of the relative uncertainty in the optical pressure signals can determine how well these various temperature and pressure profiles compare. However, one drawback to the high-speed imaging is high levels of uncertainty due to noise. An example of the oscillation in the background intensity is shown below (Figure 5.30).

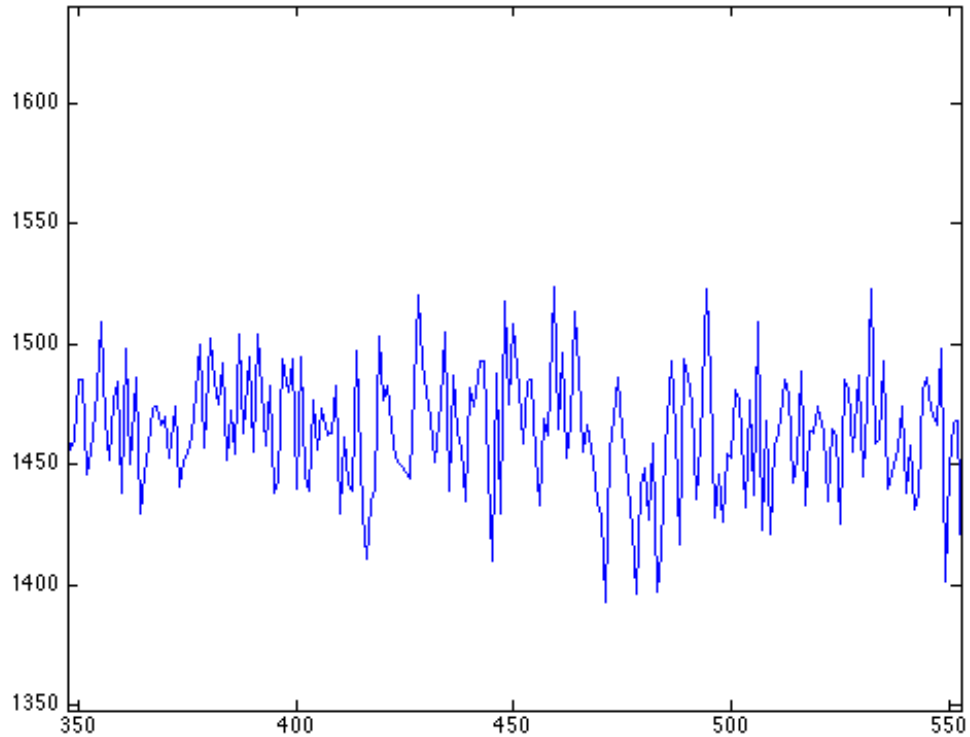


Figure 5.30: Zoomed in example of raw background intensity.

In this test, there was an average oscillation of  $\pm 114$  values in the raw pixel intensity data. This becomes a variation of  $\pm 57$  pixels in the background intensity from the average, which lead to an uncertainty of  $\pm 4000 Pa$ . This high level of uncertainty is attributed to noise from the camera sensor. A more appropriate estimate of the uncertainty is calculated by determining the atmospheric pressure across the field-of-view in one image using the Abel transform on a section of the field-of-view unaffected by the shock. Using this method, the average atmospheric pressure was  $101292 Pa$ , with a standard deviation of  $507 Pa$ . This is still a large degree of uncertainty, and an accurate uncertainty would more likely be  $\pm 200 Pa$ . The gage pressure is within the linear temperature pressure's uncertainty, while the constant temperature and CTH pressures are not. There is also some degree of uncertainty of the theoretical pressure based on the Mach number. The Mach number calculated by the shock tracking program is dependent on the uncertainty in pixel location, temperature, and the size of the calibration object. The program outputs an uncertainty based on these parameters. The Mach number in this primer test was  $1.14 \pm 0.022$ . With this uncertainty, the range in theoretical pressure becomes  $130$  to  $144 kPa$ . All but the CTH pressure profile are outside of the range of possible theoretical pressures. However, the wide range in the theoretical pressure indicates that the theoretical peak pressure should be

treated as a benchmark figure. Another possible reason for the optical or gage measurements to fail at resolving the theoretical pressure is the relative pixel size and gage response time, respectively. As the Mach number increases, the camera and gage may not be able to resolve the small area where the peak intensity of the shock exists.

### 5.2.2 NONEL Shock Tube

A compilation of the theoretical, gage, and optical peak pressures from three different distances of NONEL shock tube are shown below in Figure 5.31. The uncertainty of the theoretical pressure is  $\pm 4300Pa$ . The two data sets furthest from the shock tube were chosen for analysis, as more of the pressure field could be analyzed before the detonation gases interfered. The pressure field for the detonation of NONEL shock is calculated at  $0.127m$  in Figure 5.32 and  $0.102m$  in Figure 5.33 from the end of the shock tube. The uncertainty is calculated in the same manner as with the primers. Here, the average background pressure is  $101591Pa$ , with a standard deviation of  $\pm 407Pa$ .

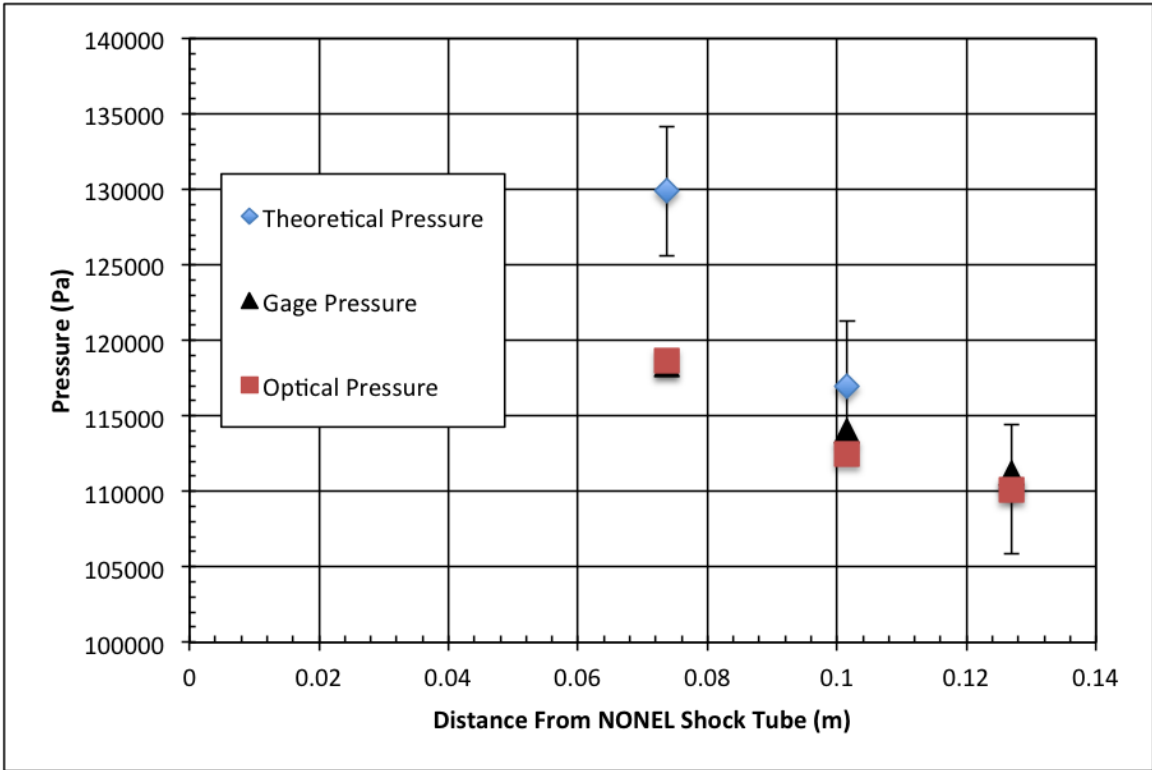


Figure 5.31: Comparison of theoretical, gage, and optical peak pressures at three distances using NONEL shock tube.

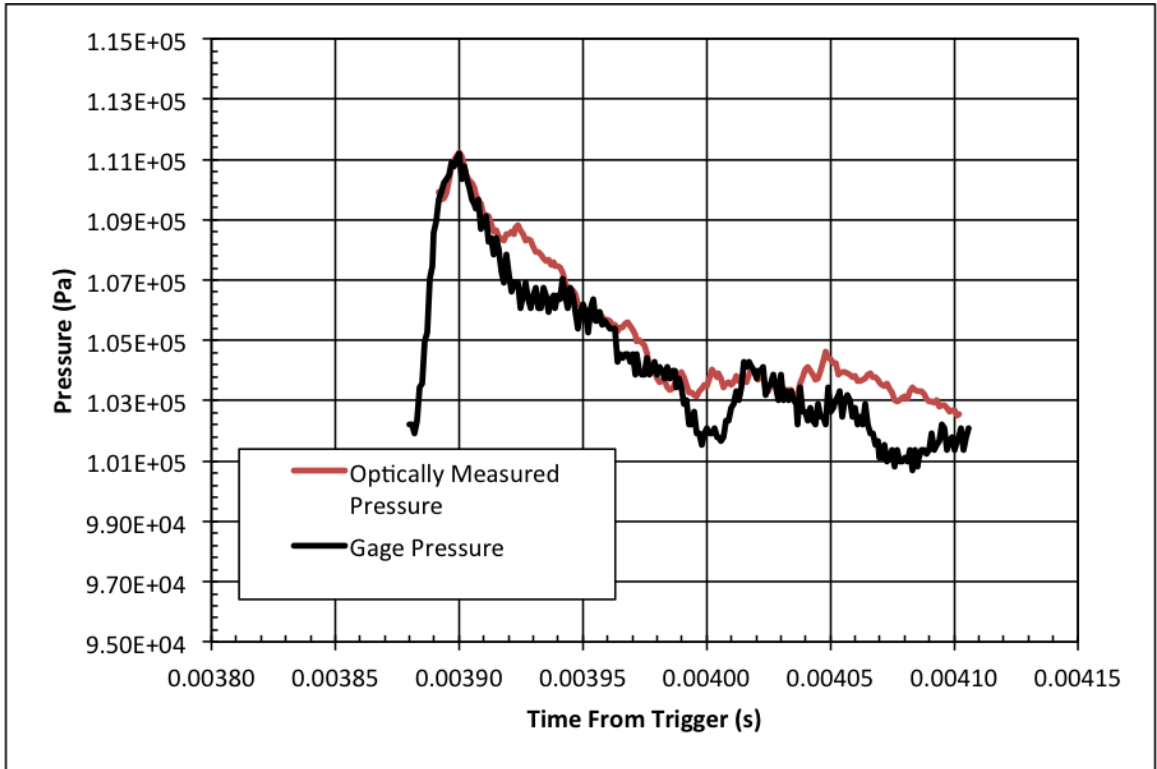


Figure 5.32: Pressure fields derived from linear temperature trends compared to gage pressure. Distance to gage 0.127m.

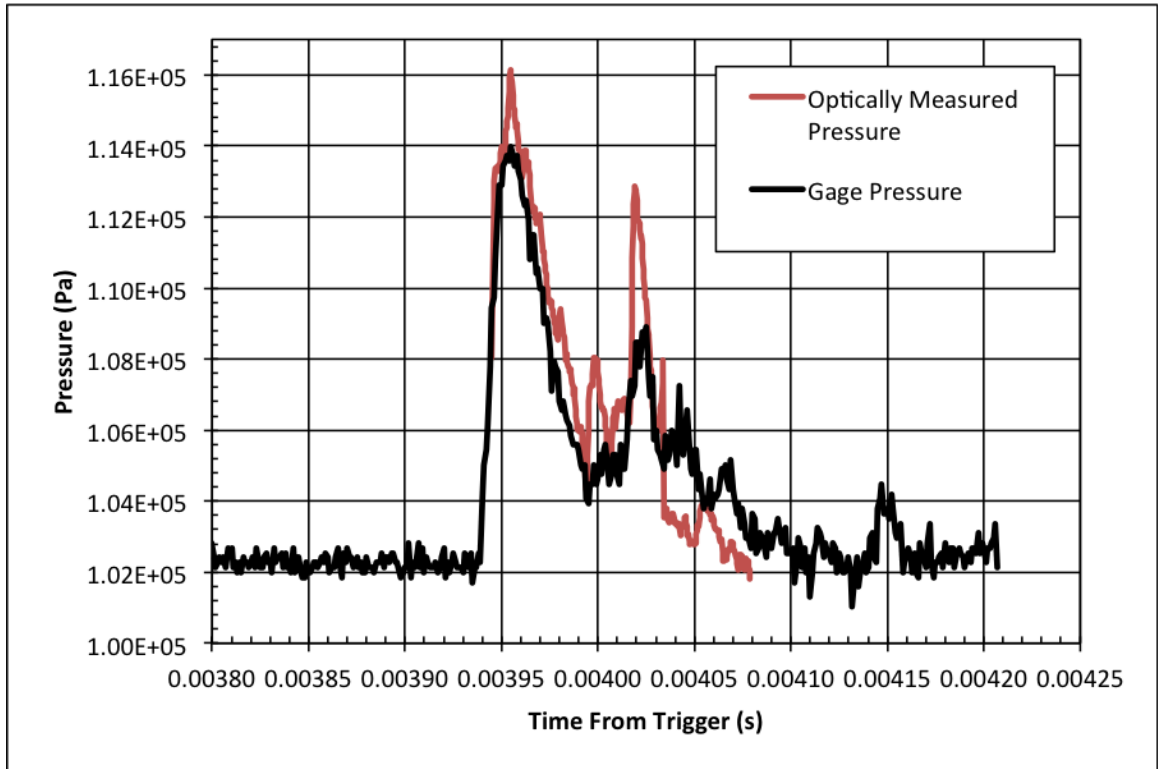


Figure 5.33: Pressure fields derived from linear temperature trends compared to gage pressure. Distance to gage 0.102m.

The plots of the optically measured pressure fields shows show several key things. The most important aspect is the inability to accurately resolve the pressure field around the secondary shock. Also, the optical pressure fields over predict the pressure behind the shock. This indicates that in a shock environment with secondary, or tertiary, shocks, multiple temperature profiles are needed to accurately recreate the pressure field. Using multiple trends would allow for the characteristics seen in the gage data and the density data (see Figures 5.15 and 5.16) to be clearly expressed when calculating pressure. Using a single linear decay profile alters the behavior of the pressure field in areas where the optical density profile indicates there should be greater variation. Ignoring the areas influenced by secondary shocks, the linear profile falls within the range of uncertainty, though it would be greatly improved by including decay trends that take secondary shocks into account. The other important aspect is that the method of creating an linear temperature decay profile clearly improves the pressure profile. This indicates that it is possible to generate temperature decay profiles from density or pressure data, as indicated by the decay trends analyzed using CTH. Therefore, its possible that pressure fields can be reproduced in tests where data collection with gages is difficult, provided the data collection is occurring at distances from the charge center where the relative decay trends are equal.

### 5.2.3 Detasheet

For these tests, the average background pressure was  $101640Pa$ , with a standard deviation of  $750Pa$ . A plot of the peak pressures from the gage, optical, and theoretical calculations is shown in Figure 5.34. Two tests at  $0.9m$  show good reproducibility of the gage and optical data, but fairly wide variability in theoretical pressures, indicating theoretical calculations serve better as a ballpark figure.

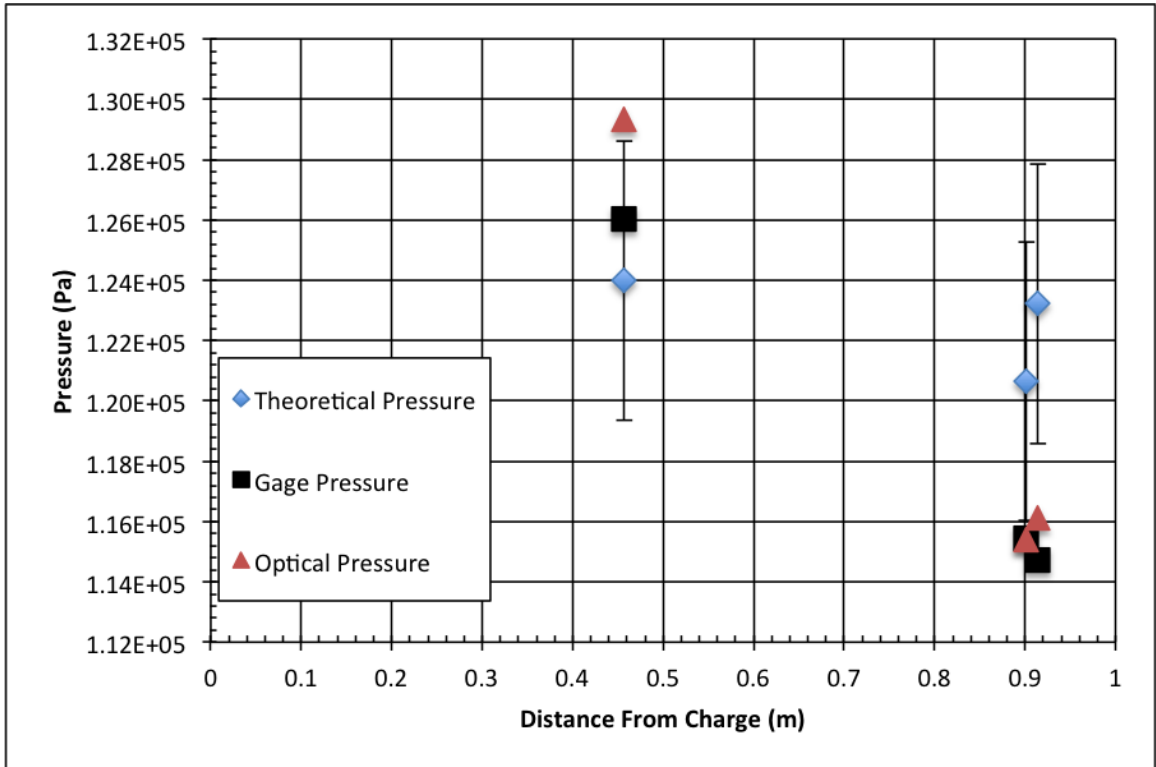


Figure 5.34: Comparison of theoretical, gage, and optical peak pressures at three distances using rolled 1g balls of Detasheet.

Plots of the pressure fields for tests at  $0.902m$  and  $0.457m$  are shown below in Figures 5.35 and 5.36. As the constant temperature profile clearly over predicts the pressure field, it is excluded. The reason for the oscillation in the gage pressure signal in Figure 5.36 cannot be quantified, as the gage was outside the field-of-view. It could be attributed to fragments crossing the gage face. The alignment of the experimental data with the gage and CTH pressure in this test is nearly perfect, indicating that using a temperature decay profile based on the experimental temperature profile is ideal for accurately resolving the pressure field. One discrepancy between the two plots is the alignment of the CTH profile with the gage and optical profiles. At a greater distance, the CTH aligns nearly perfectly with the gage and optical data. However, decreasing distance results in the

peak CTH pressures becoming greater than is observed experimentally. Again, the behavior of the CTH profile can be attributed to the highly idealized nature of the simulation.

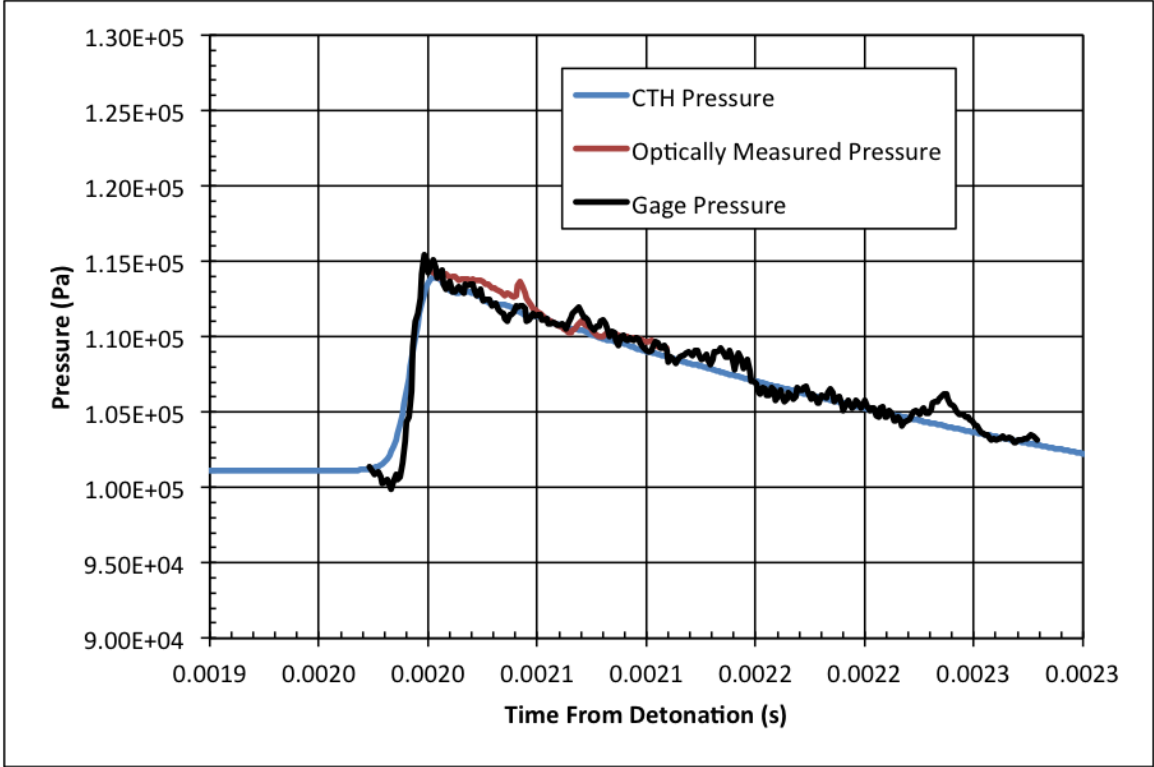


Figure 5.35: Comparison of calculated pressure field to gage and CTH pressure profiles. Distance charge to gage 0.9017m. Mach 1.08.

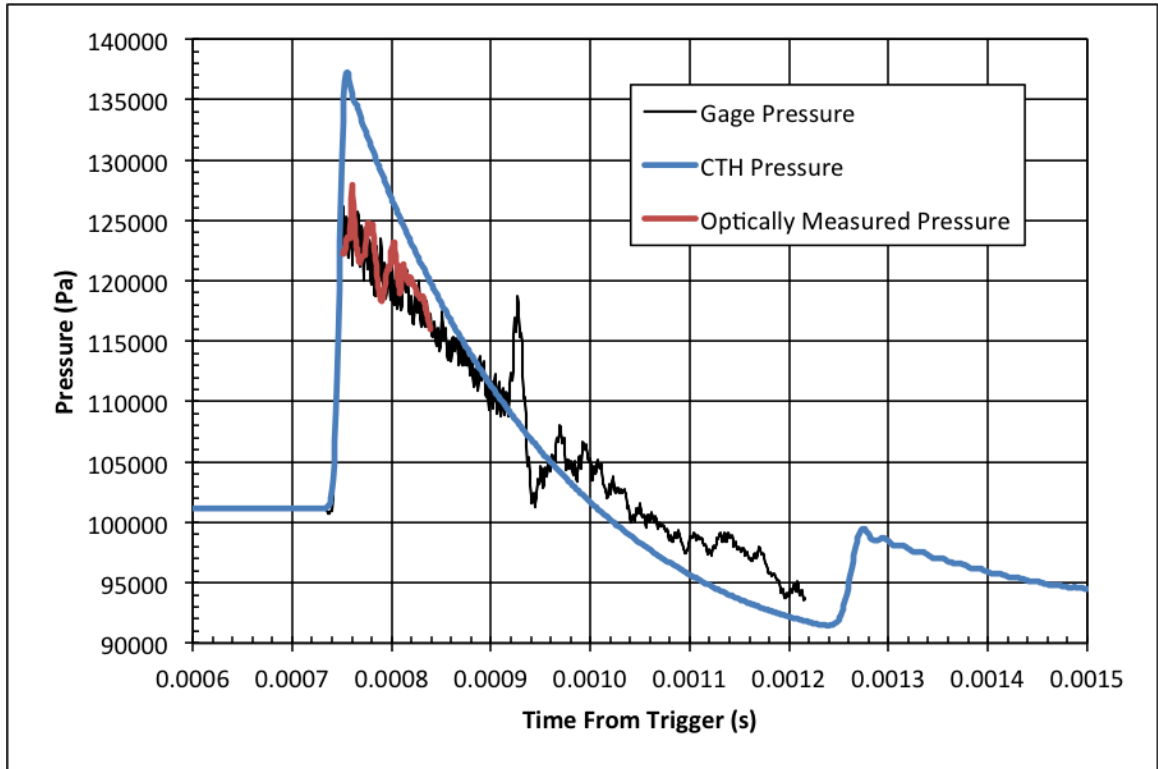
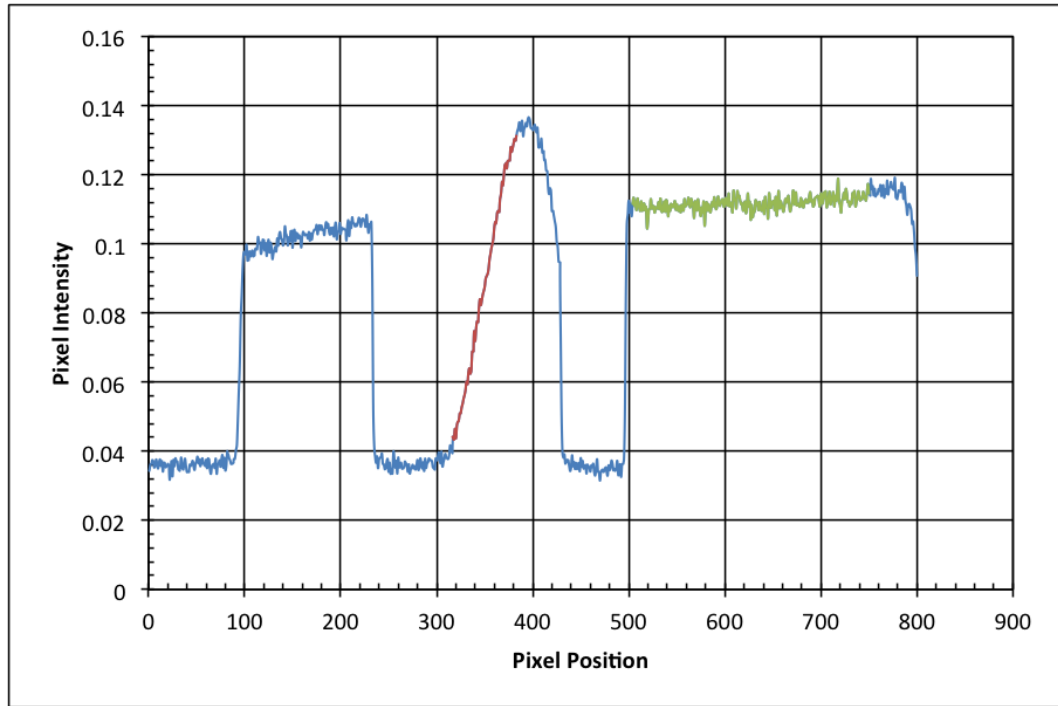


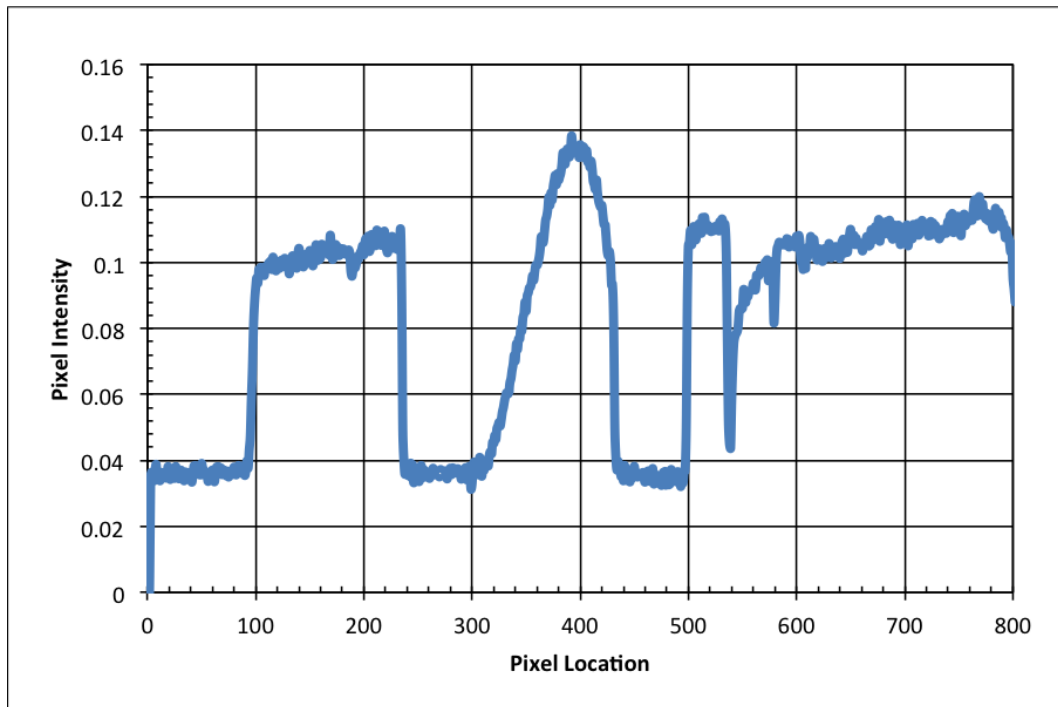
Figure 5.36: Comparison of calculated pressure field to gage and CTH pressure profiles. Distance charge to gage  $0.457m$ . Mach 1.09.

#### 5.2.4 Intensity Corrections

When the schlieren setup is correct, the intensity across the entire field-of-view should be uniform. However, should this intensity deviate linearly, it is possible to apply a correction to generate a flat background intensity. Adding or subtracting a constant value from the intensity creates this new background at each pixel location. The correction must be applied to all images being analyzed, including the intensities observed in the calibration images. For the analysis of the Detasheet, it was necessary to apply the correction to several of the later tests. An example of a typical flat background intensity and shock versus a deviated background intensity and shock is shown below in Figures 5.37 and 5.38.

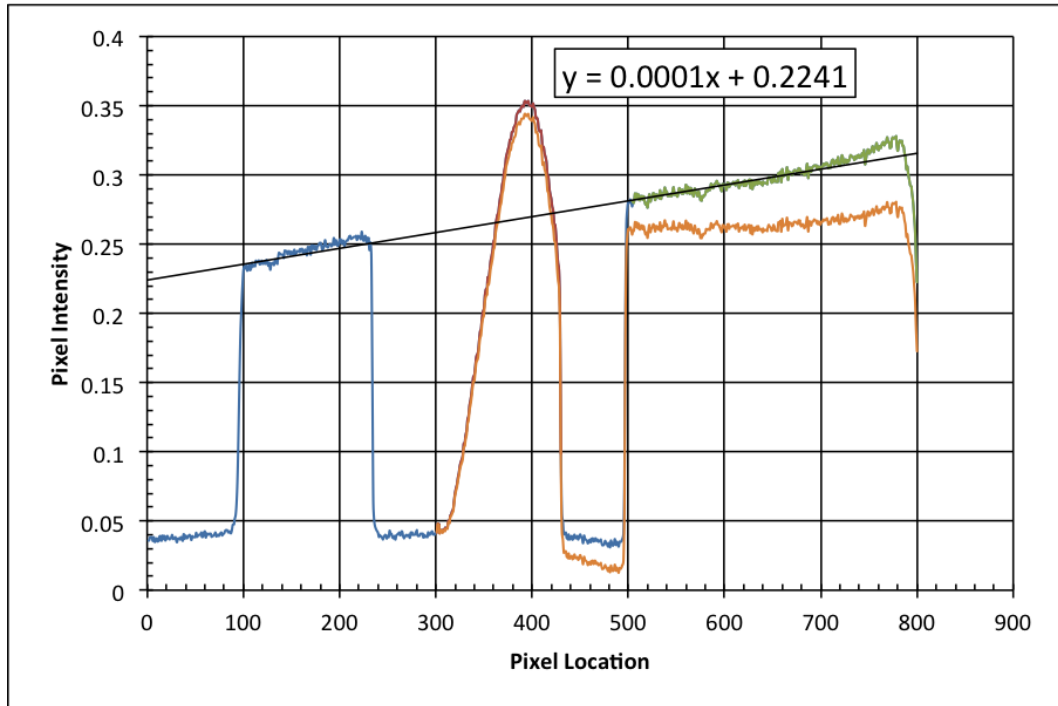


(a) Background

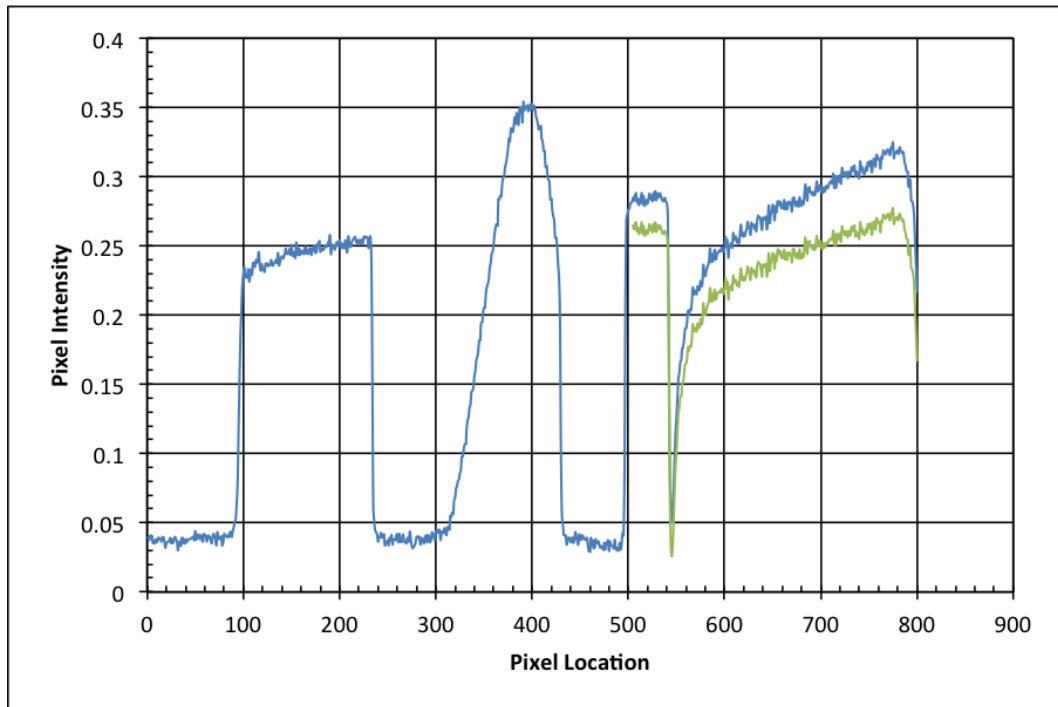


(b) Shock

Figure 5.37: Background and shock intensities for detonation of Detasheet.



(a) Background



(b) Shock

Figure 5.38: Deviated background and shock intensities for detonation of De-tasheet. Correction also shown.

This method of correction was used to create the pressure profiles in the previous section. As there is good agreement between the experimental gage and optical results, this technique is a valid tool for future use. Situations where a uniform background is difficult to achieve can be made to yield accurate results.

## CHAPTER 6

### CONCLUSIONS AND RECOMMENDATIONS FOR FUTURE RESEARCH

The schlieren technique has been shown to be capable of successfully capturing images of explosively-driven shocks, and for the shock overpressure and pressure duration to be reproduced. The images used must meet certain criteria to be successfully analyzed. The most important consideration is that the background intensity in the calibration and shock images is uniform, which allows for deviations from the background to be quantified with little error. In cases where the background deviates linearly, it is possible to apply a correction and accurately process images. Ideally, the shock should be clearly separated from the following detonation gases, as the observed changes in refractive index are quantifiable for one gas species. Additionally, the shock should be purely spherical, without fragments within the field-of-view. Oblique shocks form from the fragments, creating interference with shock processing. Finally, the schlieren setup must have sufficient light that applying a cutoff will not cause the shock intensity to zero out. The light entering the camera should take up most of the sensor's range.

The Abel two-point deconvolution technique is effective at reproducing the density, and subsequently the pressure, field. The method used has a high degree of accuracy with little computational noise. However, a disadvantage to the technique is the assumption on spherical geometry. When fragments are present, the deflection angles due to both the spherical shock and the fragments' oblique shocks are carried through the calculations. Some discrepancies between the gage and optical pressure fields is due to this.

For all three explosives, creating an optically-derived temperature field yielded better results than using the constant temperature assumption. The temperature field for the shot shell primers was created using second-order polynomial fits of the experimental density data and gage pressure. A linear decay profile was fit to the derived temperature field and used to determine the pressure field. The calculated pressure field showed the best agreement with the pressure gage data. The constant temperature profile resulted in a pressure field that was too high everywhere, so it is inappropriate to use this assumption. The CTH data over-predicted the peak pressures and under predicted the negative pulse following the shock. In the case of non ideal explosives such as shot shell primers, it is inappropriate to use the highly idealized temperature profiles determined by

CTH to calculate the experimental pressure.

The temperature profile of NONEL shock tube was created by directly applying the ideal gas law to corresponding optical density and gage pressure data points. A linear fit was applied to this profile and used to determine the optical pressure field. The use of NONEL was complicated by the presence of large secondary shocks. As the Mach number increased, the influence of secondary shocks on the pressure profile increased. Applying trends to the data was complicated by this secondary shock, as the current research focused on using a single fit for data set being analyzed. Despite this difficulty, the NONEL pressure signal was calculated with reasonable accuracy. The accuracy was best for data immediately behind the primary shock and preceding the secondary shock.

The tests using Detasheet were the closest experimental comparison to the CTH simulation. Only subsections corresponding to available optical data were analyzed to determine the temperature field. A linear fit was applied to this temperature field and used to determine the optical pressure field. These tests showed the best agreement between the gage, optically calculated pressure, and the CTH pressure data. The good alignment between the optically calculated pressure, the gage, and CTH pressures indicates that the method of deriving the temperature field is accurate, as well as the use of a linear temperature decay profile to calculate pressure.

## 6.1 Future Work

Future extensions to this work will be the application of the schlieren techniques and computational processes to the background-oriented schlieren (BOS) technique. The BOS technique visualizes the first-derivative of the refractive index and can be used to determine the same information. This technique is capable of visualizing large-scale events, using a simplified setup of the high-speed camera and a natural landscape. Other issues to be addressed include improving the accuracy of the technique and reducing the uncertainty. Different light sources and cameras should be tested in order to quantify the source of the noise in the background seen throughout the images analyzed. Additionally, the degree to which a background can vary and still produce accurate data should be quantified. Extreme setup accuracy is not always possible, particularly during field testing. Acceptable parameters for background deviation should be established. Finally, developing a method to measure across the detonation gases would be highly beneficial. Current methods cannot image through the gases, and their presence interferes with the collection of the complete pressure profile. Developing a method to image through these gases at the same time as air would allow the shock properties to be quantified very close to the explosive.

## BIBLIOGRAPHY

- [1] R. E. Duff and E. Houston. Measurement of the chapman jouguet pressure and reaction zone length in a detonating high explosive. *Journal of Chemical Physics*, 23:1268–1273, jul 1955.
- [2] Michael J Hargather and Gary S Settles. Optical measurement and scaling of blasts from gram-range explosive charges. *Shock waves*, 17(4):215–223, 2007.
- [3] A. M. Bagabir. Cylindrical blast wave propagation in an enclosure. *SHOCK WAVES*, 22(6):547–556, NOV 2012.
- [4] K. Spranghers, I. Vasilakos, D. Lecompte, H. Sol, and J. Vantomme. Numerical simulation and experimental validation of the dynamic response of aluminum plates under free air explosions. *INTERNATIONAL JOURNAL OF IMPACT ENGINEERING*, 54:83–95, APR 2013.
- [5] Geoffrey Mays and Peter D Smith. *Blast effects on buildings: design of buildings to optimize resistance to blast loading*. Thomas Telford, 1995.
- [6] Gilbert Ford Kinney and Kenneth Judson Graham. Explosive shocks in air. *Berlin and New York, Springer-Verlag, 1985, 282 p., 1, 1985*.
- [7] Zhang Qi, Qin Bin, and Lin Da-Chao. Estimation of pressure distribution for shock wave through the bend of bend laneway. *Safety Science*, 48(10):1263 – 1268, 2010.
- [8] Qi Zhang, Bin Qin, and Da-Chao Lin. Estimation of pressure distribution for shock wave through the junction of branch gallery. *Safety Science*, 57(0):214 – 222, 2013.
- [9] A Sayapin, A Grinenko, S Efimov, and YE Krasik. Comparison of different methods of measurement of pressure of underwater shock waves generated by electrical discharge. *SHOCK WAVES*, 15(2):73–80, JUN 2006.
- [10] WN MacPherson, MJ Gander, JS Barton, JDC Jones, CL Owen, AJ Watson, and RM Allen. Blast-pressure measurement with a high-bandwidth fibre optic pressure Sensor. *MEASUREMENT SCIENCE & TECHNOLOGY*, 11(2):95–102, FEB 2000.
- [11] AJ Hoffman and SM Mills Jr. Air blast measurements about explosive charges at side-on and normal incidence. Technical report, DTIC Document, 1956.

- [12] Bertram Hopkinson. A method of measuring the pressure produced in the detonation of high explosives or by the impact of bullets. *Proceedings of the Royal Society of London. Series A*, 89(612):411–413, 1914.
- [13] Per-Anders Persson, Roger Holmberg, and Jaimin Lee. *Rock blasting and explosives engineering*. CRC press, 1993.
- [14] G. S. Settles. *Schlieren and Shadowgraph Techniques*. Springer, 2001.
- [15] L Venkatakrisnan and GEA Meier. Density measurements using the Background Oriented Schlieren technique. *EXPERIMENTS IN FLUIDS*, 37(2):237–247, AUG 2004.
- [16] Michael J. Hargather and Gary S. Settles. A comparison of three quantitative schlieren techniques. *OPTICS AND LASERS IN ENGINEERING*, 50(1, SI):8–17, JAN 2012.
- [17] MM Biss, GS Settles, MJ Hargather, LJ Dodson, and JD Miller. High-speed digital shadowgraphy of shock waves from explosions and gunshots. In *Shock Waves*, pages 91–96. Springer, 2009.
- [18] Michael J. Hargather and Gary S. Settles. Retroreflective shadowgraph technique for large-scale flow visualization. *APPLIED OPTICS*, 48(22):4449–4457, AUG 1 2009.
- [19] O. K. Sommersel, D. Bjerketvedt, S. O. Christensen, O. Krest, and K. Vaagsaether. Application of background oriented schlieren for quantitative measurements of shock waves from explosions. *SHOCK WAVES*, 18(4):291–297, SEP 2008. 21st International Colloquium on the Dynamics of Explosions and Reactive Systems, Poitiers, FRANCE, JUL 23-28, 2007.
- [20] M. J. Hargather. Background-oriented schlieren diagnostics for large-scale explosive testing. *SHOCK WAVES*, 23(5):529–536, SEP 2013.
- [21] Matthew Biss. Laboratory-scale technique to optically measure explosive impulse for energetic-material air-blast characterization. Technical Report ARL-TR-6185, Army Research Laboratory, 2012.
- [22] Michael J Hargather. *Scaling, Characterization, and Application of Gram-range Explosive Charges to Blast Testing of Materials*. PhD thesis, Pennsylvania State University, 2008.
- [23] Wolfgang Merzkirch. *Flow visualization*. Elsevier, 1987.
- [24] Paul W Cooper. *Explosives engineering*. VCH New York, 1996.
- [25] Harold L Brode. Numerical solutions of spherical blast waves. *Journal of Applied physics*, 26(6):766–775, 2004.

- [26] Pankaj S Kolhe and Ajay K Agrawal. Abel inversion of deflectometric data: comparison of accuracy and noise propagation of existing techniques. *Applied optics*, 48(20):3894–3902, 2009.
- [27] Simon Ostrach. An analysis of laminar free-convection flow and heat transfer about a flat plate parallel to the direction of the generating body force. *NACA*, 1953.
- [28] J.M. McGlaun, S.L. Thompson, and M.G. Elrick. Cth: A three-dimensional shock wave physics code. *International Journal of Impact Engineering*, 10(1–4):351 – 360, 1990.
- [29] Geoffrey Taylor. The formation of a blast wave by a very intense explosion. i. theoretical discussion. *Proceedings of the Royal Society of London. Series A. Mathematical and Physical Sciences*, 201(1065):159–174, 1950.
- [30] Geoffrey Taylor. The formation of a blast wave by a very intense explosion. ii. the atomic explosion of 1945. *Proceedings of the Royal Society of London. Series A. Mathematical and Physical Sciences*, 201(1065):175–186, 1950.
- [31] H Kleine, JM Dewey, K Ohashi, T Mizukaki, and K Takayama. Studies of the tnt equivalence of silver azide charges. *Shock Waves*, 13(2):123–138, 2003.

QUANTITATIVE SCHLIEREN MEASUREMENT OF EXPLOSIVELY-DRIVEN  
SHOCK WAVE DENSITY, TEMPERATURE, AND PRESSURE PROFILES.

by

J. D. Tobin

Permission to make digital or hard copies of all or part of this work for personal or classroom use is granted without fee provided that copies are not made or distributed for profit or commercial advantage and that copies bear this notice and the full citation on the last page. To copy otherwise, to republish, to post on servers or to redistribute to lists, requires prior specific permission and may require a fee.